UNIVERSITY OF KWAZULU-NATAL

The Design, Construction and Deployment of PRI^{Z}M

by

Liju Philip

Submitted in fulfillment of the
academic requirements for the degree of
Doctor of Philosophy
in
Physics
UKZN, Durban

Supervised by Profs. Jonathan L. Sievers and Hsin C. Chiang

March 2019

To him who is able to do immeasurably more than all we ask or imagine, according to his power that is at work within us.

~Ephesians 3:20

Dedicated to my family...

Declaration of Non-Plagiarism

I, **Liju Philip**, hereby, declare that

1. The research reported in this thesis, except where otherwise indicated, is my original research.
2. This thesis has not been submitted for any degree or examination at any other university.
3. This thesis does not contain other persons' data, pictures, graphs or other information, unless specifically acknowledged as being sourced from other persons.
4. This thesis does not contain other persons' writing, unless specifically acknowledged as being sourced from other researchers.

.....

Date: .....

Publication List

Publications that form part and/or include research presented in this thesis:

1. Probing Radio Intensity at high-Z from Marion: 2017 Instrument (Philip et al., 2018).

Abstract

Observations of the redshifted 21 cm signal of neutral hydrogen can potentially help us probe the uncharted epochs in the history of the Universe. One such epoch is "cosmic dawn," when the first luminous objects lit up the Universe, a few hundred million years after the Big Bang. The radiation from first stars heated the intergalactic medium, imprinting a characteristic signature in the evolution of the globally averaged 21 cm signal when observed as a function of frequency. The 21 cm spectrum is expected to have a $\sim$200 mK absorption feature at a redshift of $\sim$20, corresponding to frequency of $\sim$70 MHz (Cohen et al., 2017). Recent results from the Experiment to Detect the Global EoR Signature (EDGES, Bowman et al., 2018) are in conflict with simple models, highlighting the need for independent global signal measurements.

In this dissertation, I introduce Probing Radio Intensity at high-Z from Marion (PRI^{Z}M, Philip et al., 2018), a new experiment designed to measure the globally averaged sky brightness, including the expected redshifted 21 cm neutral hydrogen absorption feature arising from the formation of the first stars. The PRI^{Z}M instrument consists of two dual-polarization antennas operating at central frequencies of 70 and 100 MHz, and observes in the 30–200 MHz frequency band. PRI^{Z}M is the first radio astronomy experiment to be deployed to Marion Island, in the Southern Indian ocean, over 2000 km from the nearest mainland. Marion Island is possibly the most RFI-free place known, with no visual contamination in the FM band.

This dissertation provides a detailed description of the instrument, with focus on key factors such as optimizing the hardware of remote deployability and low power consumption. I discuss the design and build of the PRI^{Z}M instrument, also provided an overview of the progress and current status of the experiment. The work in this dissertation is closely tied to our limited access to the instrument on Marion, which is about three weeks every year. The tight schedule gives rise to numerous logistical and experimental challenges that we overcame during our trips to Marion. The preliminary data analysis demonstrate that Marion Island offers an exceptionally clean observing environment, with essentially no visible contamination within the FM band. The installation of PRI^{Z}M has opened doors to an excellent site for future low-frequency endeavours.

Acknowledgments

So long, rainbow nation.

It's been almost five years since I first moved to South Africa, and now it's time to say goodbye. So many people have supported me over these years – it's an impossible task to summarize everything in a few acknowledgments. My heartfelt apologies to anyone left out.

Firstly, I express my sincerest gratitude to Jon and Cynthia for giving me an opportunity to work on PRI^{Z}M. I had a wonderful time building the instrument, and taking it to the sub-Antarctic. Every step was an adventure and a learning experience. I thank you for the support and guidance, and for teaching me an essential life skill – to be patient with *paperwork* (you know what I am talking about).

Being away from home – I have always missed my family. However, during all these years, my mom, dad and sister encouraged me in every step. You have always motivated me to push through tough times, and maintain my positive attitude towards life in general. I am grateful for all your prayers and support.

During my PhD days, I had the privilege to visit various radio astronomy research facilities around the world, and it helped me immensely in my work. I hereby express my gratitude to all the folks I met on my trips, and I thank you for all the useful conversations we had. My PhD

research would not have been possible without the support of South African National Antarctic Programme (SANAP) and the Department of Environmental Affairs (DEA), South Africa. Thank you for allowing us to explore the pristine island of Marion, and thereby opening a new door to an excellent observing location for low-frequency experiments. It was an honor to be a part of the 2016, 2017, and 2018 relief voyages to Marion Island, also to meet renowned researchers from various scientific disciplines.

With a special mention to all the students and staff at the Astronomy and Cosmology Research Unit. It was fantastic to have the opportunity to work with you. And finally, last but by no means least, also to everyone in H1-225, it was great sharing laboratory with all of you during my time at UKZN.

Thanks for all your encouragement!

Preface

The work described in this thesis was carried out in the School of Chemistry and Physics, University of KwaZulu-Natal from Feb 2016 to November 2018. This dissertation was completed under the supervision of Profs. Jonathan L. Sievers and Hsin C. Chiang.

This study represents original work by the author and has not been submitted in any form for any degree or diploma to any other tertiary institution. Where use was made of the work of others it has been duly acknowledged in the text.

List of Figures

1.1 The 21 cm HI line arises from the electron spin flip relative to the nucleus, where the electron-proton parallel-parallel spin configuration has slightly higher energy than its parallel-antiparallel configuration. In the rest frame, the transition between these two states results in emitting a photon with frequency $\nu \approx 1420$ MHz. 4

1.2 Figure from Zaroubi (2012) is presented with modified markers. The blue, green and red curves are the evolutionary models for CMB, gas and spin temperature respectively. The spin temperature couples to the gas temperature via the Wouthuysen-Field effect *(red dashed line)*, therefore creating an absorption trough at $z \sim 25$ in the above model. After the first stars heat up the IGM, the spin temperature couples to the gas temperature *(red solid line)* at $z > 10$. 8

1.3 Diagram describing the Wouthuysen-Field effect, with the hyperfine splitting of the fundamental S and the excited P levels. The HI atom after absorbing a Ly-α photon transitions to either of the P levels, followed by returning to the hyperfine S level with the emission of the photon. Solid lines indicate transitions that populate the hyperfine levels from the ground state (from Furlanetto et al., 2006). 10

1.4 Upper panel: two dimensional slice of the time evolution of the 21 cm brightness temperature, T_b (from Mellema et al., 2006). Lower panel: predicted time evolution of the global 21 cm brightness temperature with relevant epochs highlighted (from Pritchard & Loeb, 2010). 11

1.5 A figure from Cohen et al. (2017) suggests possible models of the 21 cm global signal modeled using different model physics. The colourbar indicates the ratio between Ly-α intensity and rate of X-ray heating. Early X-ray heating results in narrower troughs *(blue dips)*, as compared to intense Ly-α production by the first stars *(red dips)*. 12

1.6 A cartoon showing relativistic electrons spiraling in magnetic field and emitting synchrotron radiation. 15

1.7 A map for Galactic foreground by Haslam et al. (1982) at 408 MHz. We notice that the Galactic synchrotron emission varies significantly across the sky, where, outside the Galactic plane, shows a variety of features like spurs and cirrus, related to variations of the spectrum of relativistic electrons. 17

1.8 Results by Bowman et al. (2018) showing brightness temperature profiles from individual hardware configurations plotted against redshift z and timeline of the Universe in Myr after the Big Bang. The thick black curve represents the model with the highest signal to noise ratio. The observed absorption profile is centred at $z \approx 17$ and spans $\approx 20 > z > 15$. The flat shape of the absorption trough may suggest delayed heating of the IGM by early stars, and requires independent verification. 19

2.1 Block diagram for a single polarization PRI^{Z}M antenna. The upper and lower dashed boxes represent the first and second stages of the electronics chain. The two stages are separated by 50 m to reduce contamination from self-generated RFI. 24

2.2 CAD image from antenna redesigning. *(a)* PRI^{Z}M has a modified four-square antenna design that consists of two crossed dipoles, which are aligned north–south and east–west (refer Table 2.1 for dimensions). *(b)* Side view of a single antenna petal. The innermost triangular section has flaps on both sides that are bent downward with an opening angle of 106°. *(c)* Isometric view of simulated PRI^{Z}M antenna petals. 26

2.3 The ventral *(left)* and dorsal *(right)* sides of PRI^{Z}M dipoles. The non-folding rib on the ventral side provides the necessary rigidity to the aluminum structure and preserves the angles of the trapezoidal sections at all times. 27

2.4 *(a)* $1/10$ scale model of the 100 MHz PRI^{Z}M antenna support structure made from paper and plastic straws; *(b)* CAD modeling; and *(c)* a completed 100 MHz antenna placed on a 2m$\times$2m fibreglass grating at the Rho-Tech workshop in Durban. 28

2.5 FEKO simulated PRI^{Z}M beam responses for a single polarization of the 70 MHz *(left)* and 100 MHz *(right)* antennas. The top row shows the logarithmic beam amplitude relative to the peak, calculated at the central frequency, and the bottom row illustrates how the -3 dB *(solid lines)* and -10 dB *(dashed lines)* contours vary with frequency. 30

2.6 Cuts through the E *(dashed)* and H *(solid)* planes of the FEKO simulated beam showing the respective gains. 31

2.7 Frequency dependence of the gain at zenith angle $\theta = 0°$ *(solid)* and the 3 dB points at 70 MHz (for the 70 MHz antenna) and at 100 MHz (for the 100 MHz antenna) in E *(dashed)* and H *(dotted)* planes. 31

2.8 A 4^{th} order polynomial is subtracted from the solid line in Figure 2.7 and plotted as fractional changes in gain to show small ripples in frequency. The ripples are due to numerical artifacts in the FEKO simulation, and efforts are ongoing to improve it. 32

2.9 Magnitude *(black)* and phase *(blue dashed)* of reflection coefficient for the 70 MHz antenna. These data were taken in April 2018. The unsmooth profile of the plot is because of measurement errors due to on-site challenges during the takeover voyage. Improved measurements will be made in April 2019. 32
2.10 Magnitude *(black)* and phase *(blue dashed)* of reflection coefficient for the 100 MHz antenna. These data were taken in April 2017. The positive spikes at $<$20 MHz are unknown leakage, and the step like features are measurement artifacts. The PRI^{Z}M team will make better measurements in April 2019. 33
2.11 The evolution of the first stage electronics box, 2017 *(red inset)* and 2018 *(green inset)*. The box sits inside a cavity in the central column under the antenna. . . . 34
2.12 A simplified schematic of the first stage electronics. One wire digital temperature sensors are attached to components (marked with $\star$) to record the temperature variation across them. 35
2.13 A CCR-39S860 SP6T electromechanical switch *(left)* enables switching between on-sky and reference loads observations. There are seven SMA-F ports *(centre)*: the centre port is the output while six peripheral ones (J1–J6) are the input ports to which the antenna and the reference load are connected. The input ports J1–J6 are controlled via ports 1–6 which have J-shaped soldering hooks for electrical interfacing *(right)* and accept TTL signals. 36
2.14 *Left*: Two WEA101 LNAs connected in series (inside green ellipse) at the output of each calibrator switch in the FSE box. *Right*: S21 measurement of the two first stage LNAs with 3 dB of attenuation shows a combined gain of $\sim$40 dB. Within the frequency range shown above, the LNA's have a uniform gain response with a variation of $\sim$0.03 dB. 37
2.15 A wide angle view of a PRI^{Z}M antenna and shipping containers containing the second stage electronics, batteries, generator, fuel and spares. A 50 m long separation between the first and second stages help in minimizing self generated RFI. 38

2.16 The SSE box with its top panel removed reveals the multi-tiered interior. The design of this box is such that most of the internal components can be accessed in this configuration, however, to access the DC-DC converters (hidden in this image), we have to open one more panel (preferably the bottom one). 39
2.17 The SSE box is sealed and tested in the reverberation chamber at SKA-SA. For testing purposes, the input power is supplied using two car batteries. In order to ensure RFI tightness, the Ethernet ports on the front panel of the box are covered with a brass lid during observations. 41
2.18 A simplified schematic of the back end electronics illustrating the second stage filtering and amplification circuit connected to the spectrometer. 41
2.19 *Left*: Four identical second stage RF chain. *Right*: S21 measurements of the : Minicircuits ZX60-33LN-S+ amplifier gain *(green)*, the band limiting by Minicircuits SLP-200+ low pass and SHP-25+ high pass filters *(red)*, and the second stage filter + amplifier output with 6 dB attenuation in *blue*. The 30–200 MHz pass band is highlighted in red. 42
2.20 A Valon5009 dual frequency synthesizer. The two output ports (Source 1 and Source 2) can be locked either to an internal or to an external frequency reference. 43
2.21 *Left:* An off-the-shelf GPS patch receiver from Adafruit. *Right:* Difference between the GPS and RPi clocks over a period of 12 hours. 44
2.22 SNAP board (left) with external AT84AD001B ADC *(upper right)*. Initialization and data acquisition is done using a Raspberry PI *(lower right)* that connects to the SNAP board via a 40-pin general purpose input output (GPIO) ribbon cable. . 45
2.23 The PRI^{Z}M firmware designed using the MATLAB-Simulink package is represented in a graphical environment. The yellow blocks are used for communicating to the outside world. 46
2.24 The polyphase filter bank comprising of FIR filter and FFT blocks represented using blocks in MATLAB-Simulink block design environment. 47
2.25 Core temperatures of RPi and SNAP FPGA over a 24 hour period. The 0 hour corresponds to midnight on Marion Island. 48

2.26 The switch control circuit installed in April 2018 to drive the latching calibrator switches in both antennas. The components were assembled on a perfboard and operated using a RPi (not shown in this image) that is connected to the GPIO ribbon cable on the left. Addition of latching switches was one of the major upgrades in 2018. 50
2.27 2018 : A circuit to operate four CCR-39S860 electromechanical switches. We use five L298 high-current full-bridge drivers to provide the reset (using the top two L298s) and actuation (using the bottom three L298s) signals. A power mosfet is used to turn ON/OFF a noise source in the FSE box. The TTL signals are provided by a RPi. The circuit also has nine DS18B20 1-wire sensors for temperature feedback. 51
2.28 2017 : Four ULN2003AN chips connected in parallel to operate four CCR-38S360 switches. Each of the seven NPN Darlington transistors on a single ULN2003AN is capable of 500 mA, 50 V output. The TTL signals are provided by a RPi, and a DS18B20 1-wire sensor is used to record the temperature inside the PRI^{Z}M receiver. 52
2.29 Zooming in onto a section of the FSE box shows a subset of 1-wire DS18B20 temperature sensors *(circled)* glued to the calibrator switch and the LNAs in one of the polarizations. There are nine DS18B20 temperature sensors in each FSE box. 53
2.30 Temperature profile of LNAs *(red)*, noise sources *(black)*, calibrator switches *(green)* and ambient *(blue)* inside the 70 MHz East-West polarization FSE box recorded on 11–13 May, 2018. The diurnal temperature variation is visible in the plot. The brief dropout on the right is due to a glitch in the data from a sensor on one of the LNAs. 54

2.31 Power distribution chain of PRI^{Z}M consists of eight lead crystal batteries *(grey blocks)* of 200-Ah each. The batteries operate in pairs that are cascaded together via the green switches. During charging, the battery pairs are disconnected and a single battery charger *(blue blocks)* can charge two batteries. The yellow switches are used to operate the battery chargers. During observation, all yellow switches are powered OFF and all green switches are powered ON. 55

3.1 The Prince Edward Islands are two small islands : Marion island and Prince Edward Island, in the sub-antarctic Indian ocean. 57

3.2 The new base (*right,* yellow buildings) and the jettisoned old base (*left,* white buildings) on Marion Island. The emergency base is partially visible in green behind the new base, it serves as a helipad and a hangar for helicopter operations. 58

3.3 Satellite image of Marion Island with field huts (1–9, refer Table 3.1 for hut details) shown using yellow markers , and main base using a cyan marker. 59

3.4 The SCI-HI experiment installed on Marion during the relief voyage of April 2016. The PVC support structures failed to stabilize the antenna, and therefore it had to be tied down using nylon ropes. The orange shipping container housed backend electronics, batteries, generator, fuel and spares. 61

3.5 A Workman T-600 antenna hooked up to a Rhode & Schwartz spectrum analyzer (not visible in the photo) set up at one of the RFI survey locations on Marion. . . 61

3.6 The markers on Marion map *(top)* indicate some of the RFI survey locations during the 2016 voyage. The bottom panel shows the spectra recorded at each location. The spike at $\sim$162 MHz is from the ship's transponder. The colours in the plot correspond to the marker colours in the map. The *yellow* and *blue* sites have an increased power level possibly due to incorrect settings on the spectrum analyzer.. 63

3.7 The markers on Marion map *(top)* indicate the RFI survey locations during the 2017 voyage. We were searching for a potential observing site within the region highlighted in white that is at a reasonable hiking distance (<5 km) from the base (red marker). The bottom panel shows the spectra recorded (<300 MHz) at each location. The colours in the plot correspond to the marker colours in the map. . . 65

3.8 The PRI^{Z}M team *(foreground)* and the SANSA team *(background)* RFI surveying a candidate site near 46°52′11.70”S, 37°50′29.80”E (blue marker in Figure 3.7) during the April 2017 takeover. 67

3.9 RFI spectrum comparison between the main base and one of the candidate sites called the hydro shack. In spite of the hydro shack being easily accessible from the main base, the RFI sheilding was poor especially at lower frequencies. We can clearly see the DORIS beacon (401 MHz) at the main base from the hydro shack. Due to all these factors, the hydro shack was not selected as our deployment site. 68

3.10 Marion Island is located in the sub-Antarctic, roughly halfway between South Africa and Antarctica. The main research base is situated on the northeast side of the island, and the PRI^{Z}M observing site is about 4 km inland, between Junior’s and Fister’s kop. 69

3.11 RFI spectrum comparison between the main Marion base and the PRI^{Z}M observing location. These spectra are max hold measurements and were taken while a helicopter was operating near the base and transmitting at 123.45 MHz. A comparison of the received power at both locations provides a rough benchmark of ∼60 dB signal suppression, arising from a combination of attenuation from Junior’s kop and the distance between the PRI^{Z}M site and the base. The peak at 156 MHz is transmission from a hand held radio. 70

3.12 *Clockwise from top-left:* On-site cargo drop by the helicopter team; assembling the mechanical support structure; and installing the first stage module. 71

3.13 The PRI^{Z}M experiment installed on Marion Island. The 70 MHz and 100 MHz antennas are visible in the foreground and background, respectively, and the three orange shipping containers house the control electronics, generator and batteries, fuel cache, and spares. The main base lies 4 km behind Junior's kop. 72
3.14 *Left:* Me inspecting the electrical connections of the 70 MHz antenna petals during a snow storm at PRI^{Z}M site. *Right:* Small amount of ice accumulation near the electrical connections at the central hub of the antenna. All electrical contacts and cable feedthrough points are completely sealed from wind, water, ice and mice. 72
3.15 Schematic of a broadband noise source added to the input of all calibrator switches in April 2018. The noise source outputs a noise temperature of ∼3300 K (30–200 MHz) at 12 V. 74
3.16 The output spectrum of the noise source shown in Figure 3.15. The spectral structure is independent of system contribution. 74
3.17 The newly upgraded PRI^{Z}M system undergoing an end-to-end test at Marion base in April 2018. The SSE box is connected to two FSE boxes, and test data is being displayed on the laptop. The system is powered using 4 lead cyrstal batteries of 200 mAh each placed under the table. 75
3.18 There are three shipping containers at the PRI^{Z}M site. The command module contains newly rebuilt readout electronics for both the PRI^{Z}M and ALBATROS (described in Section 4.4) experiments, with battery banks, and chargers etc. The generator and fuel containers are the two other containers at site. 76
3.19 Mice eating away our cable insulation *(left)* and self amalgamating tape *(right)*. . 77
3.20 The PRI^{Z}M cables are protected by wrapping them with finely woven steel mesh *(left)*. A combination of steel mesh and scourer pads are used to prevent mice from entering the cable feeding pointing at the base of the antenna *(right)*. 78
3.21 The daily mean of the plasma frequency at different locations in the Southern hemisphere during the last solar minimum as predicted by the International Reference Ionosphere model (IRI-2007). 79

4.1 Spectra of raw data from a single dataset (∼4 second integration) from the PRI^{Z}M 100 MHz East-West polarization. The different spectra denote antenna and calibrator observations. 83
4.2 A representative truncated short spectrum showing ∼2.5 MHz ripple across the band. This ripple, present in antenna and calibrator spectra, is caused by standing waves in the 50 m LMR400 coaxial cable. The spike at 125 MHz is believed to be due to leakage from the FPGA clock, and its harmonic at 93.75 MHz. 84
4.3 24 hour waterfall plot of raw data from East-West polarization of the 70 MHz system recorded in April 2018. The fine horizontal streaks are due to switching between on-sky and calibrator observations. The switching cadence is one hour on the sky and one minute on each of the calibrator sources. During the April 2018 takeover voyage, the North-South polarization signal chain had a malfunction, and therefore not shown in this plot. 85
4.4 24 hour waterfall plot of raw data from East-West polarization *(top)* and North-South polarization *(bottom)* of the 100 MHz system recorded in April 2018. The fine horizontal streaks are due to switching between on-sky and calibrator observations. The switching cadence is one hour on the sky and one minute on each of the calibrator sources. 86
4.5 24 hours of waterfall plots from the 70 MHz antenna recorded in April 2017, and the 100 MHz antenna recorded in April 2018, on Marion Island. This plot shows the raw data without any calibration or RFI mitigation. 87
4.6 Representative spectra from the 70 MHz system showing day and night variation in the reflection of long wavelength transmission (<30 MHz, eg. AM radio). During daytime, when the solar activity is high, the ionosphere reflects radio waves (spikes <30 MHz in the left panel). However, during night, the reflection is significantly reduced because ions recombine and are not replenished due to photoionization. 88

4.7 PRI^{Z}M signal chain for a single polarization with antenna as the input. T_a and T_r are antenna and receiver temperatures respectively. The gains of the antenna and receiver are denoted by G_a and G_r respectively. V_{in} and V_{out} are the input and output voltages of the spectrometer. 89
4.8 A representative plot showing ∼20 min dataset from the East-West polarization of 100 MHz system that is partially calibrated using Eqn. 4.10. 92
4.9 The residuals after removing the ripples and diving by a background smooth polynomial. The plot suggests a ∼0.5% residual, thus placing PRI^{Z}M within a factor of ∼10 from the EDGES detection. The plot is generated using a semi-calibrated 20 minute dataset, hence, with more data and improved calibration, we should be able to provide better results. 93
4.10 A global sky model by de Oliveira-Costa et al. (2008) at 100 MHz plotted in the celestial coordinate system. 93
4.11 As the Earth rotates, the PRI^{Z}M 100 MHz East-West beam *(top panels)* map different patches of the sky *(bottom panels)*. Here we see the antenna observing a hotter patch when the Galactic centre is up *(right panels)*, and a comparatively colder patch when the Galactic centre is below the horizon *(left panels)*. Similarly, the North-South beam maps the orthogonal polarization. 94
4.12 Expected sky spectrum T_{sky} generated by convolving the GSM with the FEKO beam of PRI^{Z}M. 95
4.13 Daily variance of a frequency point at 100 MHz. The simulated data is in Kelvin, however, the observed data is not calibrated. Therefore, the values are feature scaled (using min-max normalization) for comparison. 96

4.14 Comparison of radio spectrum on Marion *(thick red)* and in the Karoo desert *(thin black)* in the cosmic dawn frequency range band from the 100 MHz antennas. Both data have been identically filtered by applying a light high pass and notch filters to remove ripples. This plot shows the fractional amplitude above a background fit to the raw and uncalibrated data without RFI excision. Apart from Orbcomm satellite transmission at 137–138 MHz, there is no visible RFI in the Marion data. The feature at 125 MHz is an artifact of the FPGA clock and not due to RFI. 97

4.15 ALBATROS-EGG with a baseline of ∼120 m *(yellow dashed line)* installed at the PRI^{Z}M site in April 2018. The PRI^{Z}M antennas and shipping containers are visible to the right of the ALBATROS-EGG baseline. 98

4.16 A synthesized beam of the ALBATROS experiment, with antennas at all the field huts on Marion, and a longest baseline of ∼20 km. The beam has a resolution of 8 arcminutes FWHM at 5 MHz. 99

4.17 Current version of the ALBATROS-EGG receiver with inputs from two antennas, and encloses a single SNAP board. The future revisions will cater to only a single antenna and accommodate additional hardware such as a calibrator switch circuit. An important aspect of the receiver box design is the ease of transportation for remote deployments. 100

4.18 A representative plot of auto *(top)* and cross *(bottom)* correlation of ∼3 days of East-West polarization data from the recently installed ALBATROS-EGG experiment. The auto-spectra colourbar shows log values of the raw signal amplitude recorded by the SNAP board. The fringes < 20 MHz in the cross-spectra is a visual confirmation of the antenna performance at lower frequencies, and we expect to observe at lower frequencies during the solar minimum. 101

List of Tables

2.1 Antenna dimensions (in mm), refer Figure 2.2 for segment description. 27
2.2 Switch characteristics 37

3.1 Huts on Marion (clockwise from the main base, as marked in Figure 3.3) 60

Contents

Declaration of Non Plagiarism i

Declaration of Publications ii

Abstract iii

Acknowlegments v

Preface vii

1 Introduction 1

1.1 Cosmic history 2

1.2 21 cm cosmology 3

1.2.1 The Hyperfine 21 cm Hydrogen line 3

1.2.2 Fundamental physics of the 21 cm line 4

1.2.3 Coupling between spin temperature T_S and gas temperature T_K 7

1.2.4 Evolution of the sky-averaged 21 cm signal with cosmic time 10

1.3 Challenges in observing the 21 cm signal 13

1.3.1 21 cm HI line and the bright foreground . . . 14
1.3.2 Galactic synchrotron emission . . . 15
1.3.3 Extragalactic foregrounds . . . 16
1.3.4 Foreground separation in global 21 cm observations . . . 17
1.4 Current global 21 cm signal experiments . . . 18
1.4.1 Experiment to Detect the Global EoR Signature . . . 18
1.4.2 Shaped Antenna measurement of background RAdio Spectrum 2 . . . 20
1.4.3 Large aperture Experiment to Detect the Dark Ages . . . 20
1.4.4 Broadband Instrument for Global HydrOgen ReioNisation Signal . . . 21
1.5 Outline of this dissertation . . . 22

2 PRI^{Z}M instrument development **23**
2.1 Overview . . . 23
2.2 Antenna . . . 25
2.2.1 Antenna support structure . . . 28
2.2.2 Antenna radiation pattern . . . 29
2.3 First stage electronics . . . 33
2.3.1 Calibrator switch . . . 35
2.3.2 Low-noise amplifier . . . 37
2.4 Second stage and readout electronics . . . 38
2.4.1 Filtering and secondary amplification . . . 40
2.4.2 Sampling clock . . . 42
2.4.3 System clock and GPS . . . 43
2.5 Spectrometer . . . 44
2.6 Data acquisition . . . 48
2.7 Auxiliary hardware . . . 50
2.7.1 Calibrator switch control circuit . . . 50
2.7.2 Temperature monitoring circuit . . . 53
2.7.3 Power distribution circuit . . . 54

3 Observing site and RFI characterization **56**
3.1 Overview . . . 56
3.2 Marion Island . . . 57
3.3 My voyages to Marion Island . . . 59
3.3.1 2016 relief voyage . . . 60
3.3.1.1 Site selection and installation challenges . . . 62
3.3.1.2 RFI characterization . . . 62
3.3.2 2017 relief voyage . . . 64
3.3.2.1 Site selection . . . 66
3.3.2.2 Instrument installation . . . 68
3.3.3 2018 relief voyage . . . 73
3.4 Operations and onsite infrastructure . . . 75
3.5 Mice extermination program . . . 77
3.6 Advantages of observing from Marion Island . . . 78
3.6.1 Ionosphere . . . 79
3.6.2 Meteor scatter . . . 81

4 Preliminary data and future outlook **82**
4.1 PRI^{Z}M raw spectrum . . . 82
4.2 Preliminary bandpass calibration . . . 89
4.3 Foreground modeling . . . 93
4.4 Exploring lower frequencies . . . 96
4.4.1 ALBATROS-EGG instrument . . . 98
4.4.2 ALBATROS-EGG data : first look . . . 99
4.5 Conclusions and future outlook . . . 102

Appendix **104**

A Programming Valon5009 **104**

CHAPTER 1

Introduction

Over the past few decades, our understanding of cosmology has been transformed by the success of the "standard" six parameter ΛCDM model – a model that describes the time evolution of all the components in the Universe that follows the Big Bang cosmology. The six parameters of the standard ΛCDM model are : the Hubble constant, the cold dark matter and baryon energy densities, the primordial amplitude and spectral index of scalar perturbations, and the reionization optical depth. The ΛCDM cosmological model is in general agreement with observations, and is supported by a number of independent techniques, such as the distribution of light elements in the early Universe (Beringer et al., 2012), structure of the cosmic microwave background (CMB, Planck Collaboration, 2015; Planck Collaboration et al., 2016a,b), the growth and distribution of large scale structures such as galaxies and galaxy clusters (Tegmark et al., 2006; Anderson et al., 2014; Planelles et al., 2015) and the baryonic acoustic oscillations (Seo & Eisenstein, 2005; Xu et al., 2010).

The time evolution of the Universe is classified into several epochs, and in this chapter I aim to provide an overview of low frequency fundamentals to study a wide range of cosmic epochs. The work in this dissertation, however, focuses mainly on an epoch called "cosmic

dawn," an era when the first luminous sources formed in the Universe. In the next section, I will present a brief summary on the history of the Universe.

1.1 Cosmic history

Let us begin by understanding the cosmic evolution in a chronological order from the Big Bang to its present state. In the very early Universe at $t \lesssim 10^{-43}$ seconds, it is believed that the four fundamental forces – gravitation, electromagnetism, weak nuclear interaction, and strong nuclear interaction possibly existed as one combined force. During this time, the temperature and energy density in the Universe was high ($\sim 10^{32}$ K), and it is likely that quantum gravity played an important role, thus making it harder to understand the physics in this epoch. When the Universe cooled down, it is estimated that the strong nuclear force and the electroweak interactions might have separated from each other, and possibly triggering cosmic inflation (Guth, 1981; Linde, 1982). As the Universe expanded, the quark-gluon plasma underwent a phase transition to hadronic matter (Kajantie & Kurki-Suonio, 1986; Fuller et al., 1988). Matter-antimatter asymmetry was locked in by $t \sim 10^{-6}$ seconds (Dine & Kusenko, 2003), followed by nucleosynthesis when the Universe was a few minutes old (Steigman, 2007).

The photons and baryons were coupled together in a hot plasma until the Universe was $\sim$380000 years old, and $\sim$3000 K, when matter and radiation decoupled as neutral hydrogen (HI) atoms were formed (Peebles, 1968). This epoch in the timeline of the Universe at $z \sim 1100$ is called the epoch of recombination, and the free streaming photons are observed as CMB radiation. This present day relic of the remnant radiation from the Big Bang was first detected by Penzias & Wilson (1965), followed by observations at progressively increasing resolutions by space missions such as the Cosmic Background Explorer (COBE, Bennett et al., 1993), Wilkinson Microwave Anisotropy Probe (WMAP, Bennett et al., 2003), and Planck (Planck Collaboration, 2015).

The formation of the CMB at z$\sim$1100 is followed by a period known as the cosmic dark ages, during which no luminous sources existed. The first luminous sources are expected to be formed, a few hundred millions of years after the Big Bang, in dark matter halos due to

gravitational collapse in overdense regions (Yoshida et al., 2012; Bromm, 2013; Jeon, 2015), and this epoch is called the cosmic dawn. The ultraviolet radiation from the first generation stars and black holes with accretion disks ionized the HI in the surrounding intergalactic medium (IGM). As a result, the IGM went from being once neutral to ionized state (HII), and this phase transition is called the Epoch of Reionization (EoR, Zaroubi, 2013). The fraction of HI declined as the sources continued ionizing the IGM. The EoR is believed to have lasted until $z \sim 7$, and eventually the IGM was completely ionized.

There are several observational pieces of evidence for an epoch of reionization. These include – 1. the Gunn-Peterson trough (Gunn & Peterson, 1965) which results from clouds of HI absorbing all light to the blue side of Ly-α centre (before reionization), and leaving an observable trough in the spectra of distant quasars (Fan et al., 2006; Becker et al., 2015; Mortlock, 2015); 2. CMB polarization anisotropies (Planck Collaboration et al., 2016a,b); and 3. Ly-α dropout in high redshift galaxies due to HI being opaque to Ly-α emission that escaped from galaxies, thus causing a drop in the observed Ly-α flux (Stark et al., 2011; Dijkstra, 2014; Pentericci et al., 2014). The large scale structures continued to grow after the EoR, and the Universe evolved into its present state.

Epochs such as the cosmic dawn and EoR are poorly understood since we have limited direct observations of them, and over the past few decades several experiments are making effort to map the uncharted territories. Probing these uncharted epochs require clever methods that make use of promising tracers, and in the next section I will discuss one such approach.

1.2 21 cm cosmology

The 21 cm line from neutral hydrogen is one of the most promising probes to study the Universe's history as it directly probes the evolution of the IGM (Barkana & Loeb, 2001; Furlanetto et al., 2006; Madau et al., 1997). In the subsequent sections, I will give an overview of the theoretical framework of the 21 cm line in a cosmological context.

1.2.1 The Hyperfine 21 cm Hydrogen line

Hydrogen, the most common atomic species present in the Universe, is one of the best probes to study the local properties of the intergalactic medium (IGM). The interaction of the magnetic moments of the proton and electron in a neutral hydrogen (HI) atom results in aligned and anti-aligned states of proton-electron spins.

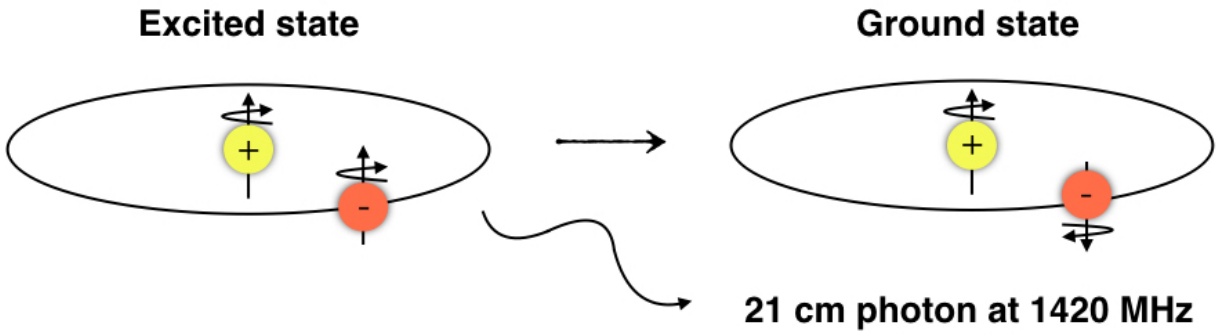

Figure 1.1: The 21 cm HI line arises from the electron spin flip relative to the nucleus, where the electron-proton parallel-parallel spin configuration has slightly higher energy than its parallel-antiparallel configuration. In the rest frame, the transition between these two states results in emitting a photon with frequency $\nu \approx 1420$ MHz.

The difference in spin states results in hyperfine splitting of the $1S$ ground state leading to two distinct energy levels separated by $\Delta E = 5.9 \times 10^{-6}$ eV, that corresponds to a rest frequency ν_0 = 1420 MHz and a wavelength of 21 cm (van de Hulst, 1945; Ewen & Purcell, 1951). The energy difference between the two hyperfine states arises due to the difference in the orientations of the magnetic moments of proton and electron. The magnetic moments are oriented anti-parallel in the excited state and parallel in the ground state (the spin states are illustrated in Figure 1.1). The 21 cm HI line is one of the best studied astrophysical probes, and its rest frequency has been accurately measured by studying hydrogen masers (Goldenberg et al., 1960). The abundance of hydrogen in the Universe makes the 21 cm observation a promising tool to study the early Universe despite a $\sim$11 million year lifetime of the excited state.

1.2.2 Fundamental physics of the 21 cm line

In the cosmological context, we are interested in using the 21 cm line to probe the clouds of neutral hydrogen along the line of sight to the background radiation source. The radiation from the background source when passing through a HI cloud results in absorption and emission, and causes variation in the specific intensity radiation. Therefore, it is important to understand the radiative transfer (Rybicki & Lightman, 1986) through the cloud along the line of sight. In the absence of any scattering medium, the radiative transfer for specific intensity radiation I as a function of frequency ν along a path s can be fundamentally represented as,

$$\frac{dI_\nu}{ds} = -\alpha_\nu I_\nu + j_\nu, \tag{1.1}$$

and the coefficients α_ν and j_ν denote the absorption and emission by gas along its path. This intensity is measured in ergs $s^{-1}cm^{-2}sr^{-1}Hz^{-1}$, and quantifies the energy of the radiation traveling along a given path, per unit area, frequency, solid angle, and time. If τ_ν is the optical depth of absorption through the cloud at a given frequency, then the radiative transfer equation becomes,

$$\frac{dI_\nu}{d\tau_\nu} = -I_\nu + B_\nu(T) \tag{1.2}$$

where $B_\nu(T)$ denotes the Planck function expressed as,

$$B_\nu(T) = \frac{2h\nu^3}{c^2}\frac{1}{e^{\frac{h\nu}{k_BT}} - 1} \tag{1.3}$$

with h and k_B being the Planck and Boltzmann constants respectively, and c is the speed of light. Using the approximation $e^x = 1 + x$ for $x \ll 1$, the denominator of Eqn. 1.3 can be simplified as follows,

$$e^{\frac{h\nu}{k_BT}} - 1 = 1 + \frac{h\nu}{k_BT} - 1 = \frac{h\nu}{k_BT}$$

Hence,

$$B_\nu(T) \approx \frac{2h\nu^3}{c^2}\frac{1}{h\nu/k_BT} = \frac{2h\nu^3}{c^2}\frac{k_BT}{h\nu} = \frac{2\nu^2 k_BT}{c^2} \tag{1.4}$$

Eqn. 1.4 is called the Rayleigh-Jeans limit, which is an excellent approximation to the Planck curve at frequencies low enough that $h_\nu \ll k_B T$. As a result, at low-frequencies of our interest we can express a relationship between I_ν and an equivalent brightness temperature T_b as follows,

$$T_b(\nu) \approx \frac{I_\nu c^2}{2 k_B \nu^2} \tag{1.5}$$

For the work presented in this dissertation, we are interested in the 21 cm brightness temperature, and therefore rewriting Eqn. 1.2 in terms of the brightness temperature,

$$\frac{dT_b}{d\tau_\nu} = -T_b + T_S \tag{1.6}$$

where T_S is the spin temperature.

Taking into account the cosmological redshift z and the comoving frame, the emergent brightness temperature $T_b^{'}(\nu)$ at the cloud can be measured on Earth as an apparent brightness $T_b(\nu) = T_b^{'}(\nu)/(1+z)$ at an observing frequency $\nu = \nu_0/(1+z)$. Therefore, the 21 cm signal radiated by a cloud at high redshift, the wavelength will be stretched by a factor of $(1+z)$ and will be observed in the meter wavelength regime (Furlanetto et al., 2006; Pritchard & Loeb, 2012; Fialkov & Loeb, 2013).

Therefore, in the Rayleigh-Jeans limit, the radiative transfer from the CMB background T_{CMB} along the line of sight through a HI cloud of optical depth τ_ν and uniform spin temperature T_S (excitation temperature) will give us an observed brightness temperature T_b at a frequency ν as,

$$T_b(\nu) = T_S\,(1 - e^{-\tau_\nu}) + T_{CMB}(\nu)\, e^{-\tau_\nu} \tag{1.7}$$

where the optical depth $\tau_\nu \equiv \int ds\, \alpha_\nu$ is the integral of the absorption coefficient α_ν along the ray through the cloud (Furlanetto et al., 2006).

The spin temperature T_S (in Eqns. 1.6 and 1.7) is defined by the relative population of the two spin states n_0 and n_1 through the relation,

$$\frac{n_0}{n_1} = \frac{g_1}{g_0}\, e^{(-E_{10}/k_B T_S)} = 3\, e^{(-T_*/T_S)} \tag{1.8}$$

where $\left(\frac{g_1}{g_0}\right)$ = 3 is the ratio of the spin degeneracy of the triplet and singlet levels, and the energy difference between the levels is $E_{10} \equiv E_1 - E_0 \approx 5.9 \times 10^{-6}$ eV (Pritchard & Loeb, 2012), and can be represented by an equivalent temperature, $T_* \equiv E_{10}/k_B = 0.0682\ K \ll T_S$. The optical depth of a HI cloud is then,

$$\begin{aligned} \tau_\nu &= \int ds \sigma_0 (1 - e^{-E_{10}/k_B T_S}) \phi(\nu) n_0 \\ &\approx \sigma_0 (h\nu/k_B T_S)(N_{\rm HI}/4)\phi(\nu) \end{aligned} \tag{1.9}$$

and $\sigma_0 \equiv 3c^2 A_{10}/8\pi\nu^2$ where $A_{10} = 2.85 \times 10^{-15} s^{-1}$ is the spontaneous emission coefficient of the spin-flip transition. ϕ_0 is the line shape function which is normalized so that $\int d\nu \phi(\nu) = 1$. $n_0 = N_{\rm HI}/4$ where $N_{\rm HI}$ is the column density of HI and the fraction on HI atoms in the hyperfine singlet state is denoted by the factor $1/4$. The line shape $\phi(\nu)$ predominantly includes natural, thermal, turbulent and velocity broadening, as well as bulk motion (which increases the effective Doppler spread). The velocity broadening has an important effect on the uniformly expanding IGM such that a region of linear dimension l will undergo velocity broadening as $\Delta V \sim lH(z)$, and as a result $\phi(\nu) \sim c/(lH(z)\nu)$. The column density along such a segment depends upon the neutral fraction $x_{\rm HI}$ of hydrogen, so $N_{\rm HI} = l x_{\rm HI} n_H(z)$ (Furlanetto et al., 2006; Zaroubi, 2012). Therefore we obtain the 21 cm optical depth of the diffuse IGM from Eqn. 1.9 as,

$$\begin{aligned} \tau_{\nu_0} &= \frac{3}{32\pi} \frac{hc^3 A_{10}}{k_B T_s \nu_0^2} \frac{x_{\rm HI} n_H}{(1+z)(d\nu_r/dr)} \\ &\approx 0.0092 (1+\delta)(1+z)^{3/2} \left(\frac{x_{\rm HI}}{T_s}\right) \left(\frac{H(z)(1+z)}{d\nu_r/dr}\right) \end{aligned} \tag{1.10}$$

where δ denotes the density contrast, $d\nu_r/dr$ is the comoving gradient of the line of sight velocity component and $H(z)$ is the Hubble parameter.

The 21 cm signal brightness temperature observed as an offset from the CMB temperature T_{CMB}, along a line of sight at a frequency ν can be expressed as (Mesinger et al., 2015),

$$\delta T_b(\nu) \approx 27 x_{\rm HI} \left(1 - \frac{T_{CMB}}{T_s}\right)(1+\delta) \left(\frac{H(z)(1+z)}{d\nu_r/dr}\right) \left(\frac{1+z}{10} \frac{0.15}{\Omega_m h^2}\right)^{\frac{1}{2}} \left(\frac{\Omega_b h^2}{0.023}\right) \left(\frac{1-Y_p}{0.75}\right) \text{mK} \tag{1.11}$$

where Ω_m and Ω_b are the matter and baryon densities respectively and Y_p is the Helium mass fraction. δT_b is sourced by variation in the spin temperature and neutral fraction in addition to the density field, and is only observed when $T_s \neq T_{CMB}$. In particular, if $T_s > T_{CMB}$ the 21 cm signal can be seen in emission, and in absorption if $T_S < T_{CMB}$.

1.2.3 Coupling between spin temperature T_S and gas temperature T_K

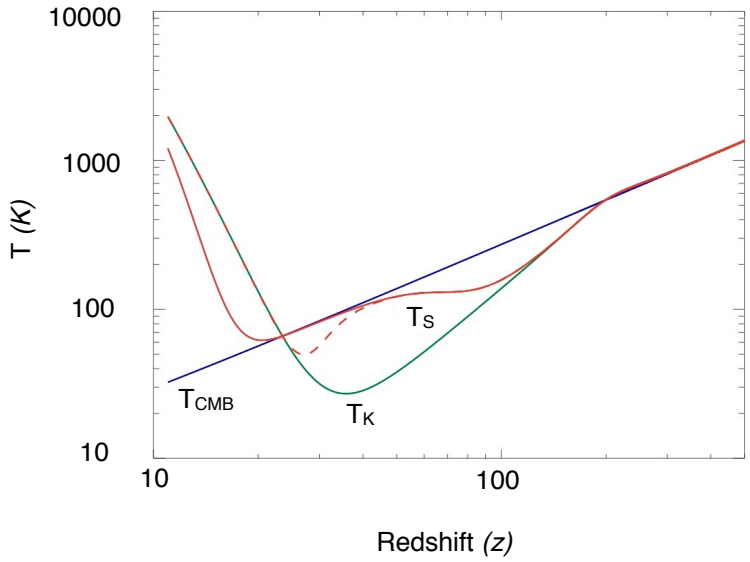

Figure 1.2: Figure from Zaroubi (2012) is presented with modified markers. The blue, green and red curves are the evolutionary models for CMB, gas and spin temperature respectively. The spin temperature couples to the gas temperature via the Wouthuysen-Field effect *(red dashed line)*, therefore creating an absorption trough at $z \sim 25$ in the above model. After the first stars heat up the IGM, the spin temperature couples to the gas temperature *(red solid line)* at $z > 10$.

The spin temperature inevitably tends to T_{CMB} unless there is a mechanism that couples it to T_K (see Figure 1.2). The processes that determine the spin temperature are:

- interaction with the background CMB photons
- HI-HI and HI-electron collisions
- resonant scattering of Ly-α photons

In equilibrium, the spin temperature can be given as the weighted sum of above three processes (Pritchard & Loeb, 2012),

$$T_S^{-1} = \frac{T_{CMB}^{-1} + x_\alpha T_\alpha^{-1} + x_c T_K^{-1}}{1 + x_\alpha + x_c} \tag{1.12}$$

where x_α and x_c are coupling coefficients for UV scattering and collisions respectively, T_α is the colour temperature of the Ly-α radiation (Fialkov & Loeb, 2013). T_α provides a measure of the shape of the spectrum near the Ly-α resonance (Meiksin, 2006).

The 21 cm signal is obtained only if T_S couples to T_K, and one of the two processes that make it happen is collisional coupling. At high redshift, $z \gtrsim 50$, T_S coupled to T_K due to collisions between HI-HI atoms (Zygelman, 2005) and HI-electron/proton (Furlanetto & Furlanetto, 2007a,b). The collisions effectively induce a spin flip in the HI atoms and dominates the coupling in the early Universe where the gas density was high (Mesinger et al., 2015). Eventually, collisional coupling becomes ineffective in coupling T_s to T_k and T_s relaxes to T_{CMB}.

However, the ultraviolet radiation from the first luminous sources interacts with the IGM, and Raman-scatter through the Ly-α resonances, thereby causing spin-flip in HI atoms between the two hyperfine levels $F = 0$ and $F = 1$. Within the Ly=α resonance region, the photons exchange energy with HI atoms via the Doppler shift, and hence are expected to be in equilibrium with the gas kinetic temperature. Therefore, the Raman scattering brings T_S into equilibrium with T_k. This process is known as the Wouthuysen-Field (W-F, Wouthuysen, 1952; Field, 1959) effect. In Figure 1.3, we illustrate the hyperfine sublevels of the 1S and 2P states of HI. A HI atom that is initially in the hyperfine singlet state will be excited to either of the central 2P excited state on absorption of a Ly-α photon. The dipole selection rules allow change in the total angular momentum of the atom $\Delta F = 0, 1$; however, $F = 0 \rightarrow 0$ transitions are prohibited, thereby making the other two hyperfine levels inaccessible. The first stage of de-excitation allows the electron to decay to the hyperfine level with the emission of a shorter wavelength photon and, with a consequent decay to the fundamental state, to emit a 21 cm photon.

The Ly-α photons scatter off HI atoms causing a slight recoil of the nucleus that absorbs energy from the photons. Previously it was believed that heating due to Ly-α scattering would

provide a strong source of heating sufficient to prevent the possibility of seeing the 21 cm signal in absorption. However, scattering changes the distribution of Ly-α photon energies, due to which photons come into equilibrium with the gas and significantly reduces the heating rate (Madau et al., 1997; Chen & Miralda-Escudé, 2004; Chuzhoy & Shapiro, 2007; Furlanetto & Pritchard, 2006). The X-ray sources inject energy into the IGM via photons that have a long mean free path, and are able to heat the gas far from the sources. The minimum of the W-F absorption trough corresponds to the point when X-ray heating switches on heating the gas above the CMB temperature leading to an emission signal.

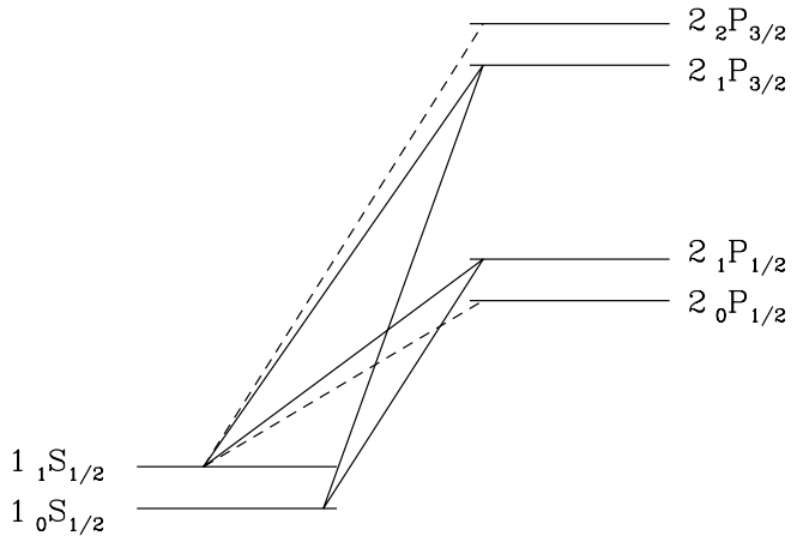

Figure 1.3: Diagram describing the Wouthuysen-Field effect, with the hyperfine splitting of the fundamental S and the excited P levels. The HI atom after absorbing a Ly-α photon transitions to either of the P levels, followed by returning to the hyperfine S level with the emission of the photon. Solid lines indicate transitions that populate the hyperfine levels from the ground state (from Furlanetto et al., 2006).

The 21 cm brightness temperature T_b can be described by a spatially averaged (or sky–averaged or global) signal that encodes the thermal history of the IGM. Experiments such as Experiment to Detect the Global EoR Signature (EDGES), Shaped Antenna measurement of background RAdio Spectrum (SARAS), Large aperture Experiment to Detect the Dark Ages (LEDA),

Broadband Instrument for Global HydrOgen ReioNisation Signal (BIGHORNS) etc. (see Section 1.4 for more details on these experiments) follow this approach, and attempt to observe the characteristic signature that is imprinted in the observable 21 cm signal, in order to constrain the high redshift Universe. An alternative approach is to map the state of the IGM via tomographic observations of 3D fluctuations in T_b (Barkana & Loeb, 2008; Morales & Wyithe, 2010) using radio interferometric arrays in experiments such as Murchison Widefield Array (MWA, Tingay et al., 2013), Precision Array to Probe the Epoch of Reionization (PAPER, Parsons et al., 2010), LOw Frequency ARay (LOFAR, Rottgering et al., 2006), Hydrogen Epoch of Reionization Array (HERA, DeBoer et al., 2017), etc.

1.2.4 Evolution of the sky-averaged 21 cm signal with cosmic time

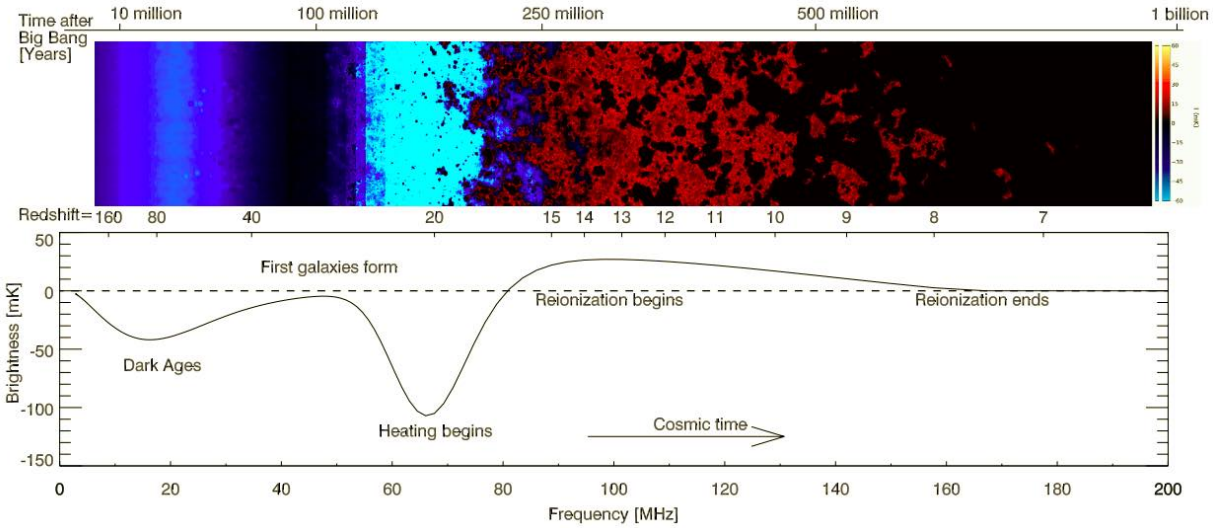

Figure 1.4: Upper panel: two dimensional slice of the time evolution of the 21 cm brightness temperature, T_b (from Mellema et al., 2006). Lower panel: predicted time evolution of the global 21 cm brightness temperature with relevant epochs highlighted (from Pritchard & Loeb, 2010).

The top panel of Figure 1.4 is a simulation of the evolution of T_b, whereas the bottom panel illustrates the fiducial model of the global 21 cm signal. The evolution of T_b is marked with several turning points that highlights its dependence on the redshift evolution. In this section,

I will provide a brief summary of the physical processes that are responsible for the frequency structures we see in the evolution of the sky-averaged 21 cm brightness temperature.

- $1100 \gtrsim z \gtrsim 200$: T_K stays coupled to T_{CMB} due to Compton scattering, and T_S couples to T_{CMB}. Therefore, no 21 cm emission is expected from this epoch as $T_b = T_{CMB}$.

- at $z \sim$200: During this time, the gas cools adiabatically faster than the CMB, as the residual fraction of free electrons is insufficient to couple T_K to T_{CMB}. Meanwhile, the collisional coupling drives $T_S < T_{CMB}$, and therefore we expect to see the 21 cm signal in absorption against the CMB. By $z \sim$80, collisional coupling loses its efficiency in coupling T_S to T_K, as a result T_S relaxes to T_{CMB} by $z \sim$30. This epoch is called the dark ages, and its standard cosmological principles and atomic physics are theoretically well studied (Hirata & Sigurdson, 2007; Valdes et al., 2010). Observations of the 21 cm fluctuations from the dark ages have indeed been suggested to be one of the most powerful probes of the dark matter power spectrum (Loeb & Zaldarriaga, 2004).

- $z \sim$30: This epoch is often referred to as the cosmic dawn, an era when the first luminous sources are expected to form in the Universe. These sources that are expected to form in the first dark matter halos, are likely to be massive, almost metal-free Population III stars which generate a Ly-α background that in turn generates the 21 cm signal via the WF effect (Field, 1959). This results in a strong absorption trough as shown by the model in Figure 1.4. However, the nature of this absorption feature is model dependent (see Figure 1.5) as the amplitude and redshift of the peak depends upon the predominant Population III or X-Ray sources. For instance, massive X-ray binaries (Pritchard & Furlanetto, 2007) or mini-quasars (Zaroubi et al., 2007) can heat the IGM by generating significant amount of X-ray radiation or massive metal-free Population III stars generating Ly-α photons can drive T_S up, and rapidly drive the 21 cm signal into emission against the CMB (Furlanetto et al., 2006), thereby reducing the peak of the absorption trough. On the other hand, delayed heating of the gas due to low X-ray emission can lead to a deeper peak and wider absorption trough (Pritchard & Loeb, 2010).

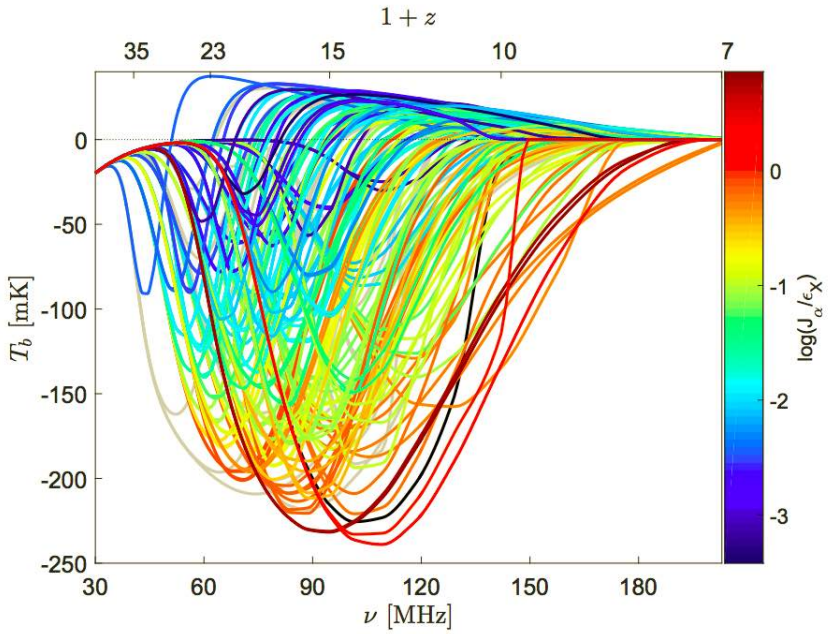

Figure 1.5: A figure from Cohen et al. (2017) suggests possible models of the 21 cm global signal modeled using different model physics. The colourbar indicates the ratio between Ly-α intensity and rate of X-ray heating. Early X-ray heating results in narrower troughs *(blue dips)*, as compared to intense Ly-α production by the first stars *(red dips)*.

- $z \sim$15: By now the IGM is heated above T_{CMB} by the X-ray radiation from stellar black-holes created as the end product of stellar evolution, and therefore the 21 cm signal is seen in emission (Morandi & Barkana, 2012) in most models. Reionization is believed to begin at $z \sim$15 with ionizing photons escaping from the host galaxies due to continued star formation, and ionizing the IGM (Barkana & Loeb, 2004; Mellema et al., 2006). Based on theoretical efforts towards understanding the details of how reionization progresses, most studies suggest that the denser HI regions are expected to be ionized first, with bubbles of HII regions merging as reionization progresses (Ciardi et al., 2003). A study by Fialkov et al. (2014), however, suggests the possibility of a "cold reionization", with the 21 cm emission appearing in absorption against the CMB up to $z \sim$10.

- $z \sim$7: As reionization progresses, the HI fraction decreases until it becomes zero around $z \sim$6 (Fan et al., 2006), and the 21 cm signal disappears.

Studying the evolution of the global 21 cm signal is therefore a promising tool to understand the physical processes occurring in the high-z Universe.

1.3 Challenges in observing the 21 cm signal

As we understand, the spectral measurements of the 21 cm monopole background has great scientific impact; and in the last decade, considerable efforts have been made towards its detection. However, the experiments that aim to detect the 21 cm HI line face multiple challenges. The primary challenge is the extreme brightness of foreground emission, contributed by both Galactic and extragalactic sources. The Earth's ionosphere also introduces significant fluctuations in the measured signal. Besides astrophysical challenges, man-made RFI swamps the frequency bands, therefore increasing the need for isolated remote deployment sites. In addition to the above, the instrument systematics too need to be precisely calibrated in order to remove instrumental effects from the data. In the next section, I will discuss the bright astrophysical foregrounds, and describe a prominent emission mechanism.

1.3.1 21 cm HI line and the bright foreground

The 21 cm global signal experiments do not need high angular resolution as the global HI signal is constant over different large patches of the sky. The characteristic scale of the 21 cm global HI signal is $\sim$10–100 mK. The measurement can be carried out using a few dipoles, and the required integration time can be determined using the radiometer equation as follows (Campbell, 2002),

$$T_{rms} = \frac{T_{sky}}{\sqrt{\Delta\nu t}} \tag{1.13}$$

where T_{rms} is the system temperature, T_{sky} is the sky temperature, $\Delta\nu$ is the bandwidth and t is the integration time in seconds. For example, observing at a bandwidth of 1 MHz and T_{sky} $\sim$1000 K; the observing time required to reach the 100 mK sensitivity is,

$$t = \left(\frac{T_{sky}}{T_{rms}}\right)^2 (1/\Delta\nu) \approx 10000 \text{ seconds} \approx 3 \text{ hours}$$

Although it takes only a few hours to attain the required signal to noise ratio for global signal experiments, the attempted measurement is complicated. Lets say, in order to make a 5σ detection using a system with pure thermal noise T_R, the required integration time as per Eqn. 1.13 becomes $t = T_R^2/(5^2\Delta\nu)$. The measurement is affected by system uncertainty, which should ideally be small after subtracting the instrument contribution from the measurement.

In addition to systematics, the astrophysical foreground dominates the cosmological signal by up to five orders of magnitude. The bright astrophysical foreground is a combination of both Galactic and extragalactic emission. Accurate modeling of the foreground and adoption of effective foreground removal techniques play major roles in the success of 21 cm experiments. One of the key goals in foreground modeling is to follow an approach based on the mechanism responsible for the emission. There are several mechanisms that drive emission in the Galactic and extragalactic domains, out of which one is discussed below.

1.3.2 Galactic synchrotron emission

The dominant emission process is a non-thermal radiation called synchrotron emission that originates from relativistic electrons accelerated in a magnetic field, and results in the brightest foreground at lower frequencies (Lawson et al., 1987; de Oliveira-Costa et al., 2008).

An accelerated electron spirals in the magnetic field B and generates radiation (see Figure 1.6). In case of non-relativistic electrons, this radiation is called cyclotron radiation and the frequency of radiation is simply the frequency of gyration of the electron in the magnetic field. However, for relativistic electrons, the frequency spectrum is complex and extends to many times the gyration frequency. The beaming is therefore concentrated in a narrow set of directions about the velocity of the electron, and is visible to a distant observer only if it is aligned with the observer's line-of-sight. The resulting synchrotron radiation is confined to a time period much shorter than the gyration time.

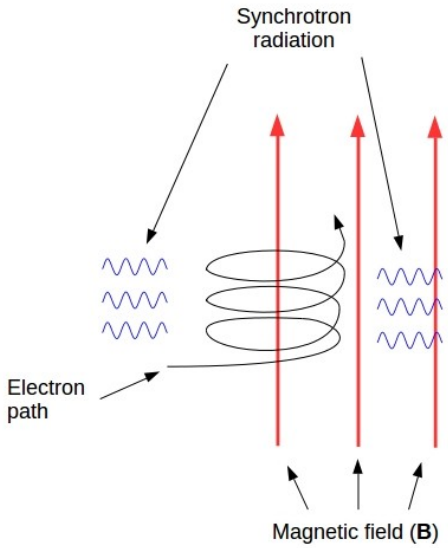

Figure 1.6: A cartoon showing relativistic electrons spiraling in magnetic field and emitting synchrotron radiation.

A relativistic electron with energy $E = \gamma m_e c^2$, emits radiation over a range of frequencies, with the peak frequency called *critical frequency* ν_c given by (Rybicki & Lightman, 1986),

$$\nu_c \sim \frac{3\gamma^2 qB}{2m_e c} sin\alpha \tag{1.14}$$

where γ is the Lorentz factor, m_e and q are the mass and charge of the electron respectively, c is the speed of light, and α is the electron direction pitch angle to the magnetic field B.

For an electron, the synchrotron radiation is negligible at frequencies larger than ν_c. Therefore, the synchrotron spectrum emerging from a population of electrons emitting at a wide range of critical frequencies is, therefore, expected to span a wide range of frequencies and can be approximated by a power law (as the underlying electrons' energy spectrum is a power law),

$$P_\nu \propto \nu^\beta \tag{1.15}$$

where β is the spectral index, and can be related to the distribution of particle energies with index p over a wide energy range as $\beta = (p-1)/2$ (Rybicki & Lightman, 1986).

When the intensity of synchrotron radiation or the electron density within a source is sufficiently high, then the radiation can be (partially) absorbed by relativistic electrons themselves,

leading to a characteristic peak in the synchrotron spectrum, below which $\beta \sim -0.5$. This phenomenon is termed *self absorption* and can be particularly prominent at low radio frequencies (*e.g.* $<$100 MHz for quasar 3C48, Kellermann & Owen, 1988) where the optical depth of the plasma is higher.

The Galactic synchrotron emission varies across the sky as shown in Figure 1.7. Observing at 408 MHz, Haslam et al. (1982) described a thick disc around the Galactic plane and features like spurs and cirrus outside the Galactic plane. These features are related to variations of the spectrum of relativistic electrons (Beuermann et al., 1985; Sironi, 1976).

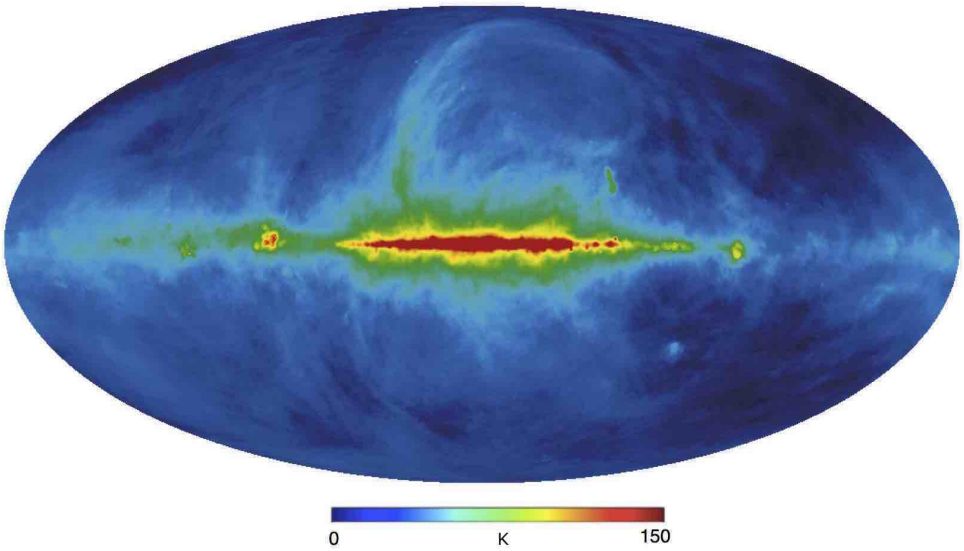

Figure 1.7: A map for Galactic foreground by Haslam et al. (1982) at 408 MHz. We notice that the Galactic synchrotron emission varies significantly across the sky, where, outside the Galactic plane, shows a variety of features like spurs and cirrus, related to variations of the spectrum of relativistic electrons.

Mozdzen et al. (2017) reports $2.60 > \beta > 2.62 \pm 0.02$ between 0 and 12 h LST, which flattens out to $\beta = 2.50 \pm 0.02$ when the Galactic plane is up. Spatial variations up to $\Delta\beta \sim$0.3 are common on degree scales (Lawson et al., 1987; Platania et al., 1998) for sky-averaged synchrotron spectrum.

1.3.3 Extragalactic foregrounds

The extragalactic foregrounds are considered to come from discrete sources outside our galaxy. Generally, global signal experiments have broad primary beams, hence it averages together a great number of extragalactic sources in its field of view. Therefore, extragalactic foregrounds cannot be distinguished from Galactic foreground in our case, and they both combine to form the total foreground. While Galactic emission dominates the foregrounds in global signal experiments, the extragalactic discrete sources also emit synchrotron radiation, and their integrated emission is estimated to constitute $\sim$27% of the total foreground at 150 MHz (Shaver et al., 1999). The variation in intensity of extragalactic emission depends upon the sources that emit radiation; for example, the bright extragalactic emissions originate from active galactic nuclei (AGN) from central supermassive black holes in galaxies Gleser et al. (2008), that is believed to power the emission "jets" and "lobes", while Sadler et al. (2003) suggests that the fainter emission is due to processes related to star formation.

1.3.4 Foreground separation in global 21 cm observations

The conventional foreground separation approach relies on the difference in the spectral behavior of the foreground and the cosmological signal. The foregrounds generally exhibit smooth, power-law-like spectra that must be subtracted from observations to reveal the cosmological signal. The most common foreground removal technique involves fitting a power law and subtracting polynomials in log frequency to remove the spectrally smooth components (Bowman et al., 2009; Gleser et al., 2008; Jelić et al., 2008; Liu et al., 2009; Wang et al., 2006), although recent literature reports approaches that focus considerably on minimizing the signal loss during signal separation (Zuo et al., 2018).

In global 21 cm observations, any spectral structure introduced by the instrument will corrupt the spectral-smoothness of foregrounds and contaminate the cosmological signal (Nhan et al., 2017). Therefore, instrument calibration is crucial in order to avoid spectral leakage into the data.

1.4 Current global 21 cm signal experiments

Despite challenges in 21 cm cosmology, several experiments are making considerable efforts to detect the cosmological signal. Some of the ongoing global 21 cm experiments are discussed in the following subsections.

1.4.1 Experiment to Detect the Global EoR Signature

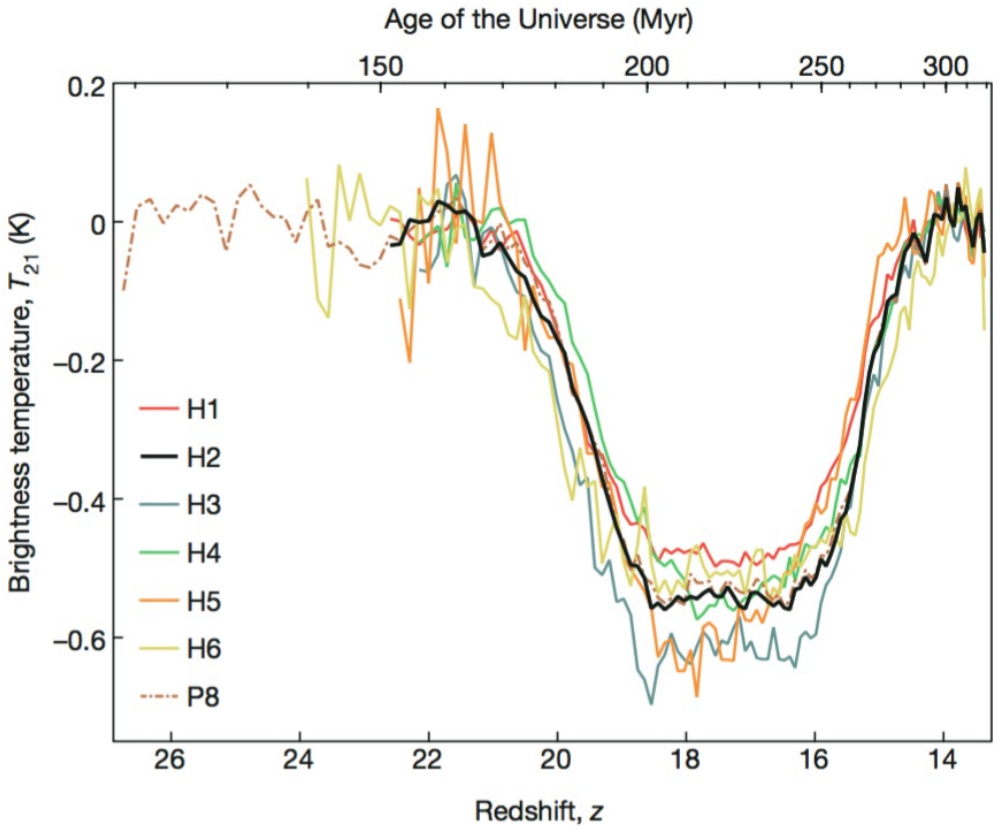

Figure 1.8: Results by Bowman et al. (2018) showing brightness temperature profiles from individual hardware configurations plotted against redshift z and timeline of the Universe in Myr after the Big Bang. The thick black curve represents the model with the highest signal to noise ratio. The observed absorption profile is centred at $z \approx 17$ and spans $\approx 20 > z > 15$. The flat shape of the absorption trough may suggest delayed heating of the IGM by early stars, and requires independent verification.

EDGES, located at the Murchison Radio-astronomy Observatory (MRO) in Western Australia, is a wide field-of-view, broadband experiment that aims to measure the 21 cm brightness temperature of the primordial HI gas. EDGES consists of three instruments of 6.1 kHz resolution each : a high- band instrument operating over the $90 - 200$ MHz ($14 > z > 6$) range, a mid-band instrument operating over 60–160 MHz, and a low- band instrument that is sensitive to the $50 - 100$ MHz ($27 > z > 13$) range. Observing from the Southern hemisphere using EDGES, Mozdzen et al. (2017) probed the diffuse radio background and provided an improved measurement of the spectral index as $2.60 > \beta > 2.62 \pm 0.02$ for $0 - 12$h LST . Monsalve et al. (2017) placed limits on the duration of reionization to be $\Delta z = 1.3$, for a reionization redshift of $z_r = 8.5$. Results from Monsalve et al. (2017) also suggest a cold reionization with no heating of the IGM by early stars at $z_r = 6$.

Bowman et al. (2018) recently reported the first detection of the 21 cm global signal as a flattened absorption profile centred at a frequency of 78.1 MHz. As illustrated in Figure 1.8, the reported absorption feature is 18.7 MHz wide with an amplitude of 0.53 K, and is more than a factor of two brighter than the most optimistic model where no heating happens until $z \sim 17$, therefore suggesting a hotter background or the primordial gas being colder than expected. The detection has called for an interpretation of newer physics in terms of collisional dark matter (Barkana, 2018; Barkana et al., 2018) and independent verification by similar experiments.

1.4.2 Shaped Antenna measurement of background RAdio Spectrum 2

SARAS 2 is a broadband precision radiometer operating within the $40 - 200$ MHz ($z \sim 6 - 34$) frequency band to detect the global 21 cm signal from the cosmic dawn and the epoch of reionization. The instrument consists of a custom designed spherical-disc monopole antenna with the electronics housed beneath the metallic disc (Singh et al., 2018a). The SARAS 2 antenna is optimized to be frequency independent with the resonant frequency kept outside the observing band. The antenna beam is omnidirectional with a maximum response at 30° elevation with nulls towards the horizon and zenith, and a half power beam width of 45°. The backend electronics are contained in an RFI-shielded environment about 100 m away from the antenna, and the signal

transmission is carried out using RF over fiber. The continuous time signals are sampled at 500 MHz using a 10-bit analogue-to-digital converter ADC. Signal channelization is performed using an FFT algorithm implemented on a Virtex- 6 FPGA that yields 2048 complex data points from which auto- and cross-spectra are computed. SARAS 2 was deployed at the Timbaktu Collective (Southern India, 14°14′32″N, 77°36′45″E). Analysis of the first light data reports rejection of 27 out of 264 global 21 cm templates predicted by Cohen et al. (2017). Moreover, 25 models were rejected with a confidence $> 5\sigma$, therefore ruling out early x-ray heating and rapid reionization in the early Universe (Singh et al., 2018b).

1.4.3 Large aperture Experiment to Detect the Dark Ages

The LEDA experiment (Price et al., 2017) operates as part of the Long Wavelength Array (LWA, Taylor et al., 2012; Ellingson et al., 2013) at the Owens Valley Radio Observatory (LWA-OVRO). The LWA-OVRO array consists of 251 dual-polarized dipole antennas in a 100 m radius circle, and 5 outrigger antennas were fitted with LEDA instrumentation. LEDA operates in the frequency range 10–88 MHz (Taylor et al., 2012; Bernardi et al., 2016). The instrumentation of LEDA facilitates in situ characterization of the foreground, monitoring of ionosphere, and measure antenna gain patterns during observations. The backend of LEDA has a FX-correlator, with F-engines running on ROACH-2 field-programmable gate array (FPGA) boards from the CASPER collaboration. The data is sampled at $\sim$196 MHz with a channel resolution of 24 kHz (4096 channels).

Bernardi et al. (2016) set the upper limits on the 21 cm signal from the cosmic dawn to date using a Bayesian foreground subtraction method. They report constrains on the amplitude and width of the 21 cm signal to be 890 mK and 6.5 MHz respectively at the 95% confidence level in the (100$> \nu >$50 MHz) ($z \sim$13.2–27.4) range.

1.4.4 Broadband Instrument for Global HydrOgen ReioNisation Signal

BIGHORNS is a portable, low power consuming total-power radiometer deployed in remote, radio quiet locations in Western Australia. The experiment uses off-the-shelf biconical

antenna, oriented East-West and placed at a height of 52 cm on a 3 m $\times$ 3 m ground screen (Sokolowski et al., 2015). For calibration purposes, the system observes the sky and a known reference load (50 Ω terminator) with a switching cadence of 7 or 15.5 seconds on the antenna, and 5 seconds on the reference in both cases. The total gain of the front-end is set to $\sim$68–75 dB in order to ensure maximum utilization of the 8 bit dynamic range of the digital system. The backend electronics are separated by a distance of 100 m from the front end. At the backend, the signal is amplified, filtered and sampled at 960 MHz using an 8 bit ADC with bandwith of 20 MHz. A four tap polyphase filterbank in the spectrometer channelizes the data into 4096 channels with a spectral resolution of $\sim$117 kHz.

Over the 2012–2014 season, BIGHORNS collected data from three locations in Western Australia – 1. Muresk; 2. Eyre Bird Observatory (EBO); and 3. Wondinong Station Based on test data collected using the prototype system, BIGHORNS made several improvements in the instrument namely, addition of a hot/cold load calibration scheme, replacing solid state switches with mechanical switches in the front end in order to eliminate unwanted attenuation, removal of the 3 dB attenuator between the antenna and the LNA, and replacing the biconical antenna with a conical log spiral antenna which is better matched over a wide frequency band. Most of these improvements are believed to significantly improve calibration accuracy.

1.5 Outline of this dissertation

The outline of this dissertation is as follows: In Chapter 2, I will provide a detailed description of the PRI^{Z}M instrument that I have designed, and present a detailed walk through of various stages in the system. In Chapter 3, I will introduce Marion Island, the observing location of PRI^{Z}M, and present modest RFI characterization of the island. I will also provide a brief summary of all my voyages to Marion. We are currently analyzing the data from our previous observing season, therefore I will be presenting only preliminary results in Chapter 4, and conclude in the same chapter.

CHAPTER 2

PRI^{Z}M instrument development

2.1 Overview

Probing Radio Intensity at high-Z from Marion (PRI^{Z}M, Philip et al., 2018) is an experiment that is designed to measure the global redshifted 21 cm signal from neutral hydrogen, with the aim of constraining the expected absorption feature in the brightness temperature that arises from the formation of the first stars. The PRI^{Z}M experiment comprises two dual-polarization radiometers operating at centre frequencies of 70 and 100 MHz. The combined frequency range of both antennas spans 30–200 MHz, which brackets the predicted absorption feature from cosmic dawn.

The PRI^{Z}M system was developed in the radio astronomy lab at University of KwaZulu-Natal (UKZN). PRI^{Z}M is a collaboration between UKZN, Carnegie Mellon University (CMU), University of California Berkeley (UCB), South African National Space Agency (SANSA) and Square Kilometer Array, South Africa (SKA-SA).

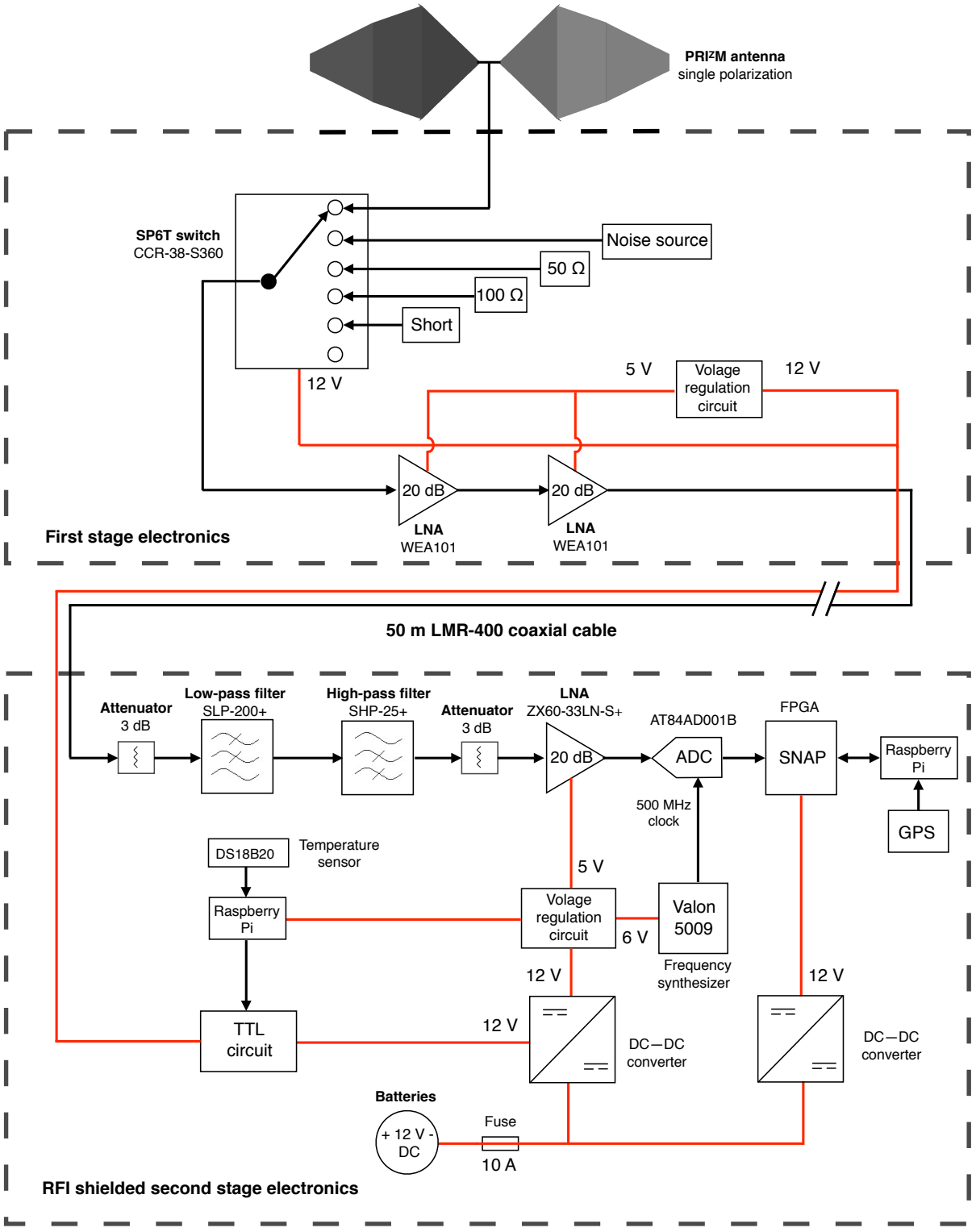

Figure 2.1: Block diagram for a single polarization PRI^{Z}M antenna. The upper and lower dashed boxes represent the first and second stages of the electronics chain. The two stages are separated by 50 m to reduce contamination from self-generated RFI.

The PRI^{Z}M hardware follows a standard radio instrumentation design consisting of general functional blocks, namely – 1. antenna; 2. first stage electronics; and 3. second stage electronics. Figure 2.1 shows a block diagram of the PRI^{Z}M signal chain for a single polarization. In the upcoming sections, I will discuss different stages of the instrument in the order of its purpose in the system.

2.2 Antenna

The PRI^{Z}M radiometers have a modified four-square antenna design that was originally developed by Jáuregui–García et al. (2017) for the Sonda Cosmológica de las Islas para la Detección de Hidrógeno Neutro (SCI-HI, Voytek et al., 2014) experiment. The detailed antenna geometry was tuned with FEKO[1], a 3D electromagnetic (EM) simulator, in order to minimize the beam chromaticity. The FEKO simulations indicate that the transmission efficiency is $\geq 90\%$ in a frequency range of 40–85 MHz for the 70 MHz antenna and 65–130 MHz for the 100 MHz antenna, thereby providing a frequency overlap of 20 MHz (65–85 MHz). During the initial days of SCI-HI antenna design by Jáuregui–García et al. (2017) and Voytek et al. (2014), a scaled model antenna tuned to 400–500 MHz was tested in an anechoic chamber at Carnegie Mellon University to obtain the frequency response for different scaled models. Parameters such as the inter-petal separation, height of the antenna with respect to the ground plane, and angles of the trapezoidal facets, which impacts the impedance, beam symmetry, and beam width, respectively, were finely tuned based on the tests in the chamber.

As shown in Figure 2.2, each antenna consists of four petals that form a pair of crossed dipoles. Each petal has three trapezoidal facets angled at various angles with respect to the ground in order to reduce the radiation pattern variations with frequency. The width of the antenna radiation pattern has direct dependence on the angles of the trapezoidal facets, and the height of the antenna above the ground changes the beam symmetry. The impedance of the antenna is linked to the inter-petal separation (Jáuregui–García et al., 2017).

The original SCI-HI antennas were fabricated using double sided FR4-4 fiberglass sand-

[1] https://altairhyperworks.com/product/FEKO

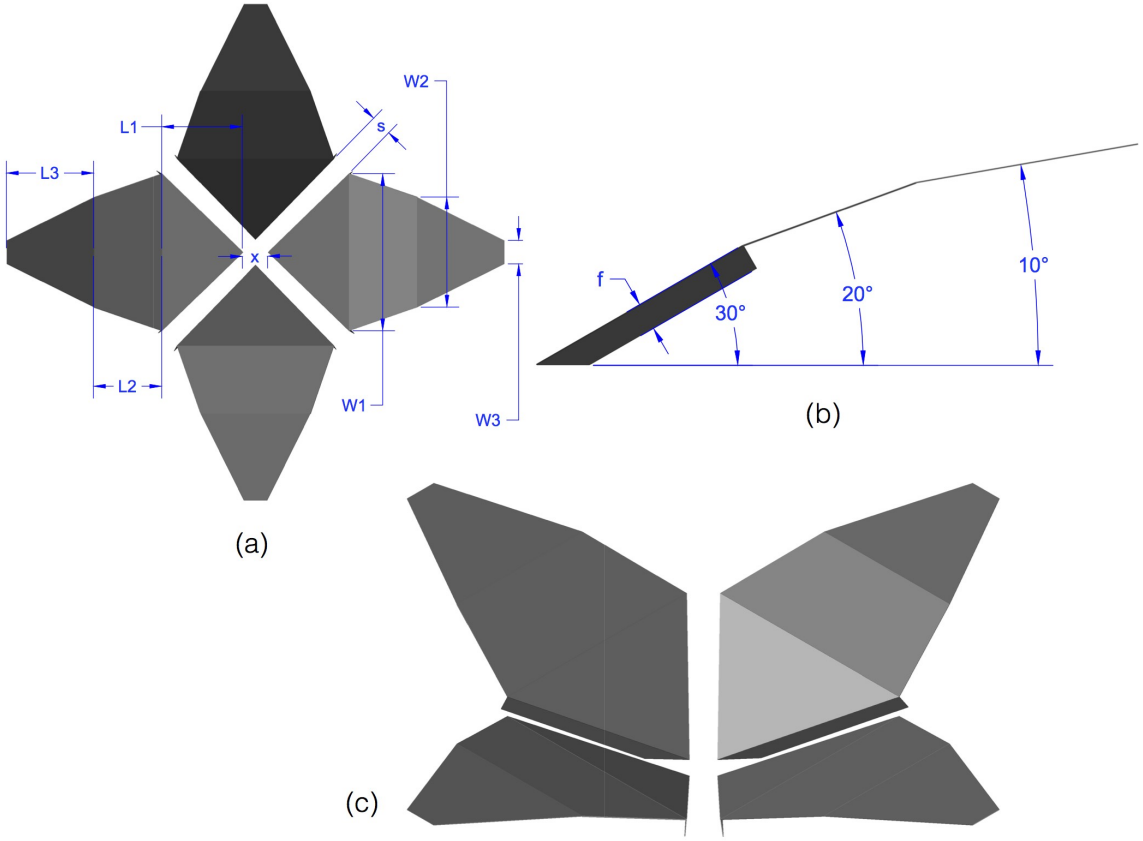

Figure 2.2: CAD image from antenna redesigning. *(a)* PRI^{Z}M has a modified four-square antenna design that consists of two crossed dipoles, which are aligned north–south and east–west (refer Table 2.1 for dimensions). *(b)* Side view of a single antenna petal. The innermost triangular section has flaps on both sides that are bent downward with an opening angle of 106°. *(c)* Isometric view of simulated PRI^{Z}M antenna petals.

wiched between two thin sheets of copper. The antenna petals were constructed in sections, and the individual sections were hinged together to form a foldable structure. For PRI^{Z}M, I redesigned the original SCI-HI antennas to include a non-folding rib on the ventral side of the petals (see Figure 2.3). Inclusion of a non-folding rib preserved the angles between the various sections in a petal at all times.

More importantly, the non-folding feature of the antennas suited our travel and deployment needs. Besides, the redesign should not have changed the electromagnetic properties of

Table 2.1: Antenna dimensions (in mm), refer Figure 2.2 for segment description.

Segment	70 MHz	100 MHz
L1	583	371
L2	451	287
L3	550	350
W1	980	624
W2	686	436
W3	147	93.4
x	41.8	26.5
s	50.7	31.7
f	66	42

Figure 2.3: The ventral *(left)* and dorsal *(right)* sides of PRI^{Z}M dipoles. The non-folding rib on the ventral side provides the necessary rigidity to the aluminum structure and preserves the angles of the trapezoidal sections at all times.

the antennas as all original dimensions were preserved. The antenna petals are made of 2 mm thick aluminum with black powder coating to mitigate snow and ice accumulation. The detailed dimensions of the 70 MHz and 100 MHz antenna petals are given in Table 2.1.

2.2.1 Antenna support structure

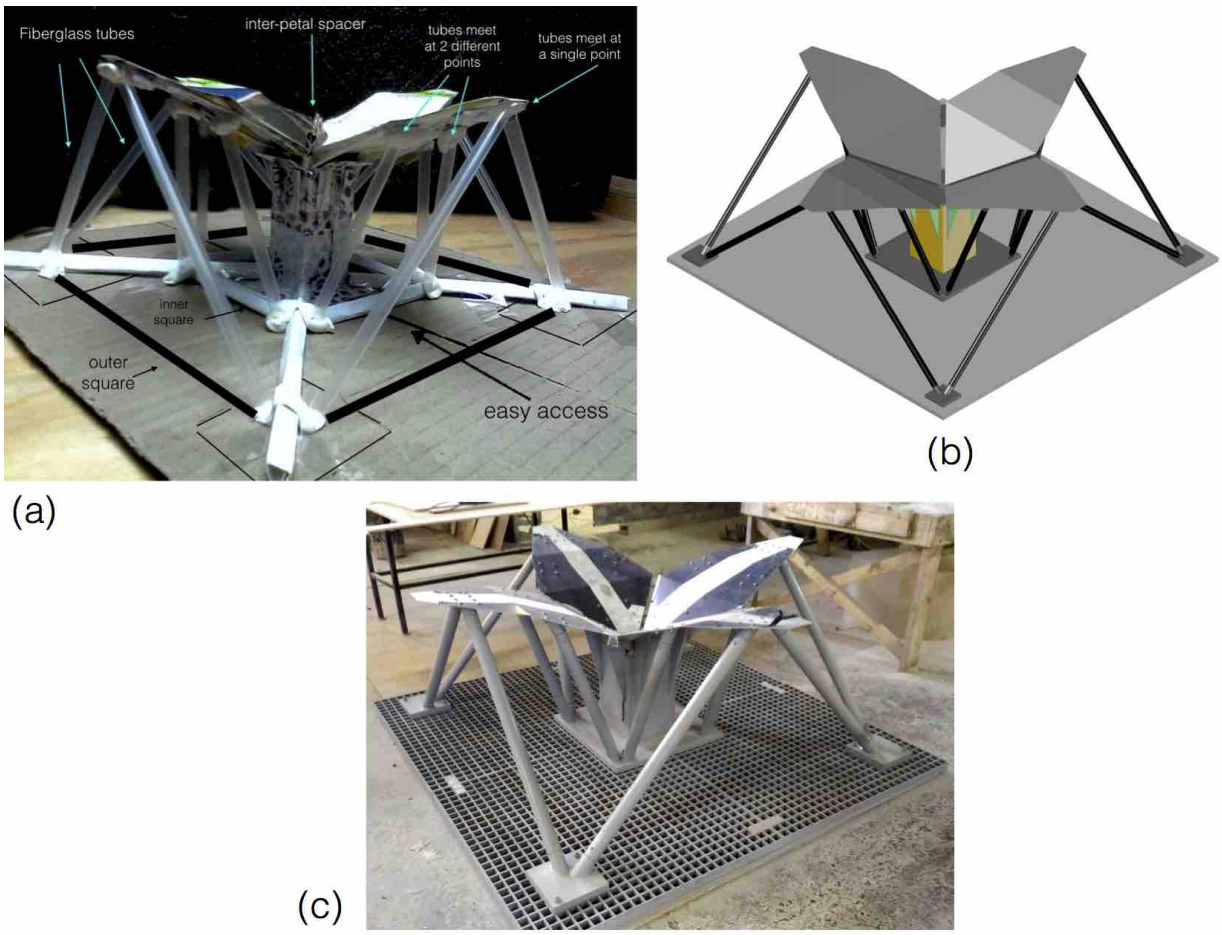

Figure 2.4: *(a)* $1/10$ scale model of the 100 MHz PRI^{Z}M antenna support structure made from paper and plastic straws; *(b)* CAD modeling; and *(c)* a completed 100 MHz antenna placed on a 2m$\times$2m fibreglass grating at the Rho-Tech workshop in Durban.

Following our first deployment to Marion Island (see Section 3.3.1), the antenna support structures needed a major redesign to withstand the strong persistent winds known as the “roaring

forties" on Marion. I, therefore designed a new support structure and tested its relative robustness on a $1/10$ scale model of the 100 MHz antenna constructed using cardboard and plastic straws. I then translated the model into a computer-aided design using AutoCAD[2] software (2016 version) for Macbook. A local thermoplastic company called Rho-Tech[3] fabricated the fiberglass structure from my CAD model. The panels *a, b* and *c* of Figure 2.4 show the different stages of the support structure build.

The antennas are stationary and point at zenith, and the polarization axes are aligned with the cardinal directions. The antenna petals are supported by a fiberglass structure that consists of a central column, angled trusses, and a rigid base plate. The central column houses the first stage electronics, the trusses provide the necessary rigidity for sustaining high winds, and the base plate provides both anchoring weight and a flat mechanical reference surface. The entire antenna and fiberglass structure sits on top of a ground screen that is roughly 10 m on a side and is made of welded wire mesh. The 70 MHz and 100 MHz antenna assemblies are scaled versions of each other and are roughly 3 m and 2 m on a side, respectively. Under normal working conditions, it takes about half a day to completely assemble both antennas.

2.2.2 Antenna radiation pattern

Our collaborators in CMU used FEKO to simulate the radiation pattern of the PRI^{Z}M antennas. Machining and assembly tolerances were modeled and adjusted to guarantee the antenna characteristics match the simulations. Both antennas have a 10 m $\times$ 10 m welded mesh ground screen, extended by sixteen 10 m radial spokes. The central ground screen and radial extension balance the electromagnetic performance and ease of installation. Simulations of the antenna's ground plane show that for the damp soil at the deployment site, a 10 m $\times$ 10 m ground screen is not enough to allow the currents to drain and the resonances create ripples in the response. However, the 10 m $\times$ 10 m ground screen was the largest practical size possible at the deployment site, therefore we found it easier to install the radial spokes which provided a smoothing effect

[2] https://www.autodesk.com/education/free-software/autocad-for-mac

[3] http://www.rho-tech.co.za/

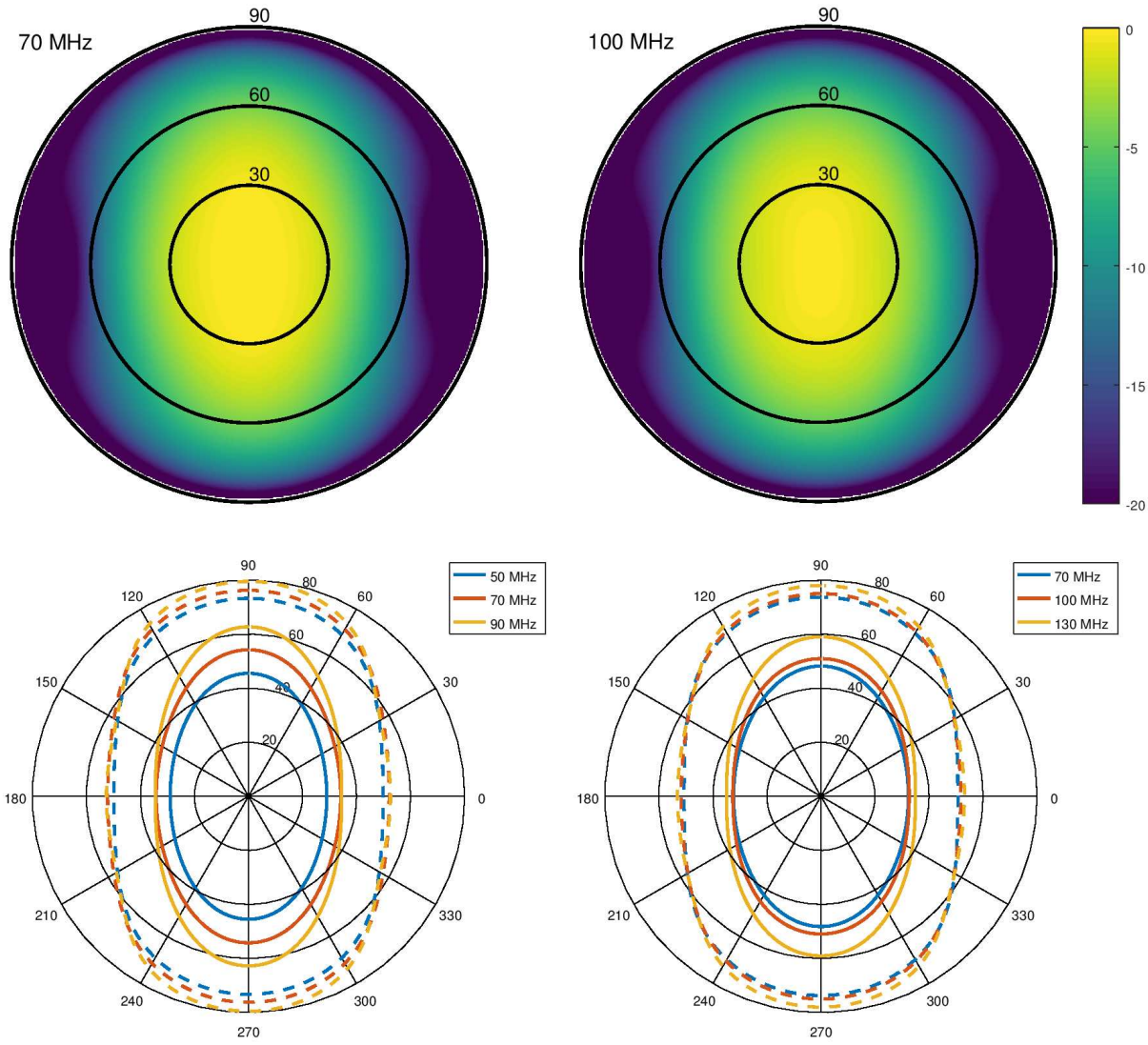

Figure 2.5: FEKO simulated PRI^{Z}M beam responses for a single polarization of the 70 MHz *(left)* and 100 MHz *(right)* antennas. The top row shows the logarithmic beam amplitude relative to the peak, calculated at the central frequency, and the bottom row illustrates how the -3 dB *(solid lines)* and -10 dB *(dashed lines)* contours vary with frequency.

on the response similar to that by a larger ground screen ($\sim$20 m).

Figure 2.5 shows the predicted beam patterns of the antennas, as simulated by FEKO. The 3 and 10 dB contours reveal the slight variation in the beam response as a function of frequency. Figure 2.6 shows the beam cross-sections through the electrical (E) and magnetic (H) field planes

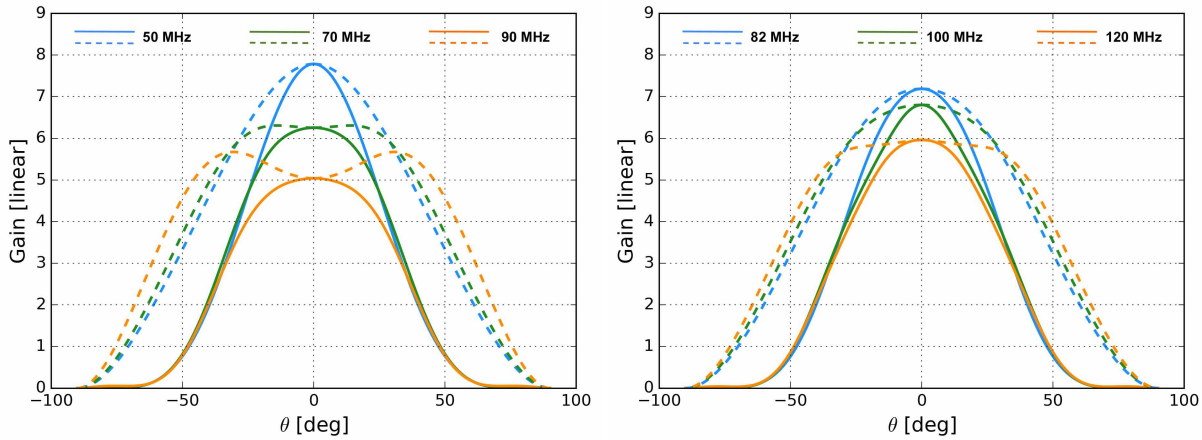

(a) 70 MHz (b) 100 MHz

Figure 2.6: Cuts through the E *(dashed)* and H *(solid)* planes of the FEKO simulated beam showing the respective gains.

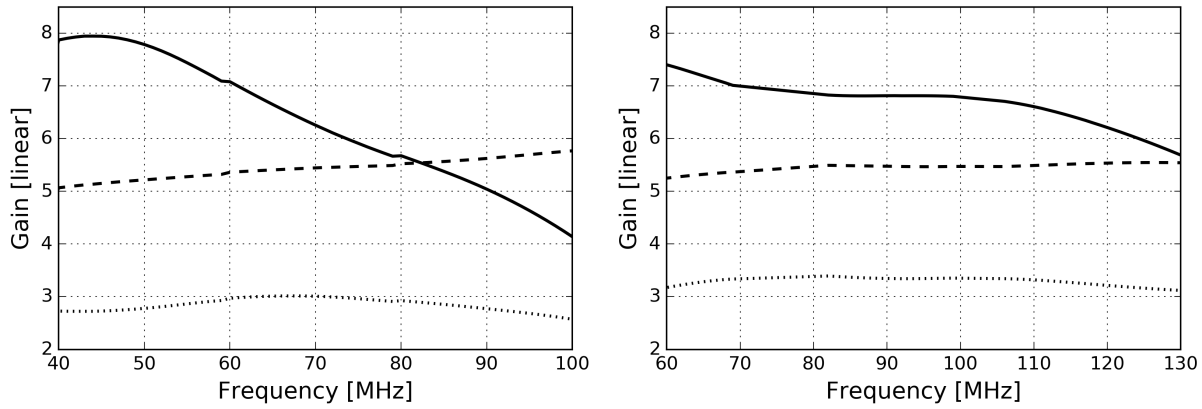

(a) 70 MHz (b) 100 MHz

Figure 2.7: Frequency dependence of the gain at zenith angle $\theta = 0°$ *(solid)* and the 3 dB points at 70 MHz (for the 70 MHz antenna) and at 100 MHz (for the 100 MHz antenna) in E *(dashed)* and H *(dotted)* planes.

of 70 and 100 MHz antennas respectively. In both, E and H planes, the gain of the radiation patterns for both antennas have a slight dependence on frequency. This frequency dependence, shown in Figure 2.7, is fitted with a 4^{th} order polynomial and subtracted from the model, and plotted as fractional changes in the gain (Figure 2.8) showing small ripples across the spectrum.

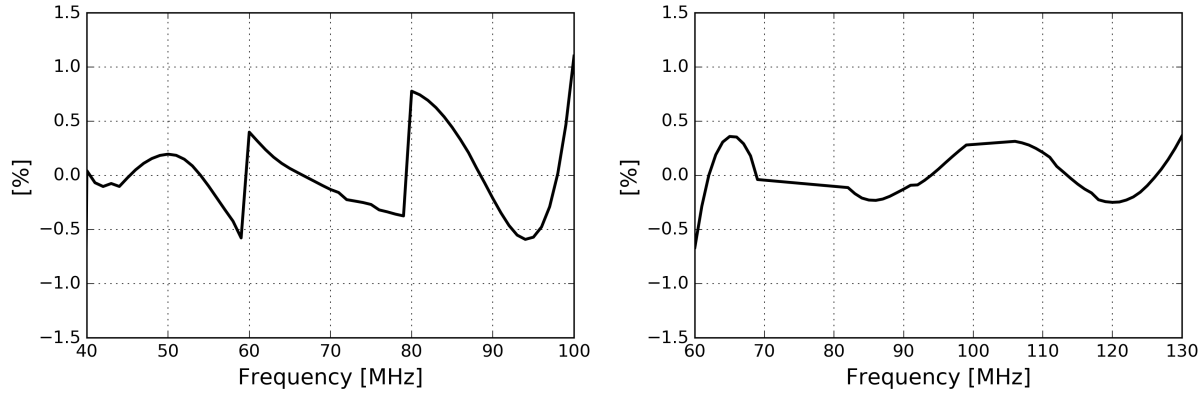

(a) 70 MHz (b) 100 MHz

Figure 2.8: A 4^{th} order polynomial is subtracted from the solid line in Figure 2.7 and plotted as fractional changes in gain to show small ripples in frequency. The ripples are due to numerical artifacts in the FEKO simulation, and efforts are ongoing to improve it.

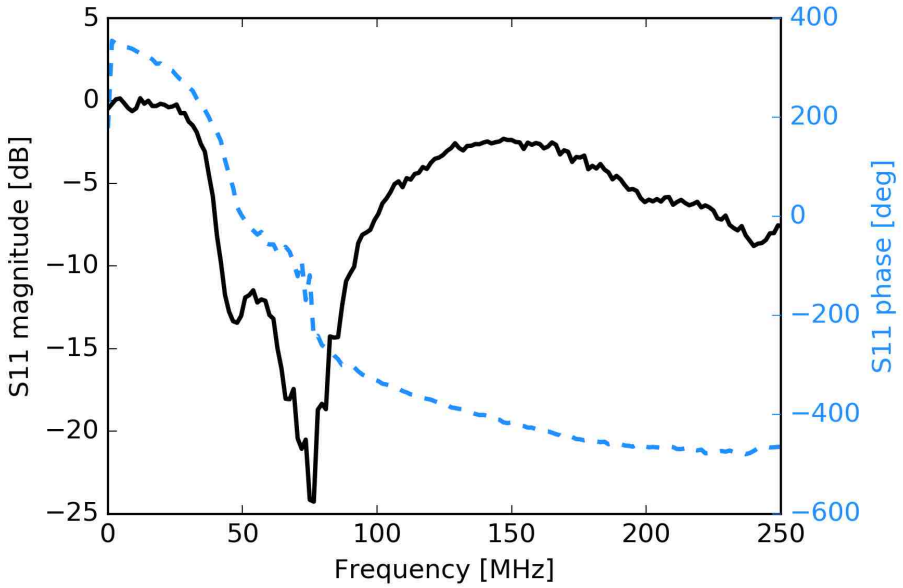

Figure 2.9: Magnitude *(black)* and phase *(blue dashed)* of reflection coefficient for the 70 MHz antenna. These data were taken in April 2018. The unsmooth profile of the plot is because of measurement errors due to on-site challenges during the takeover voyage. Improved measurements will be made in April 2019.

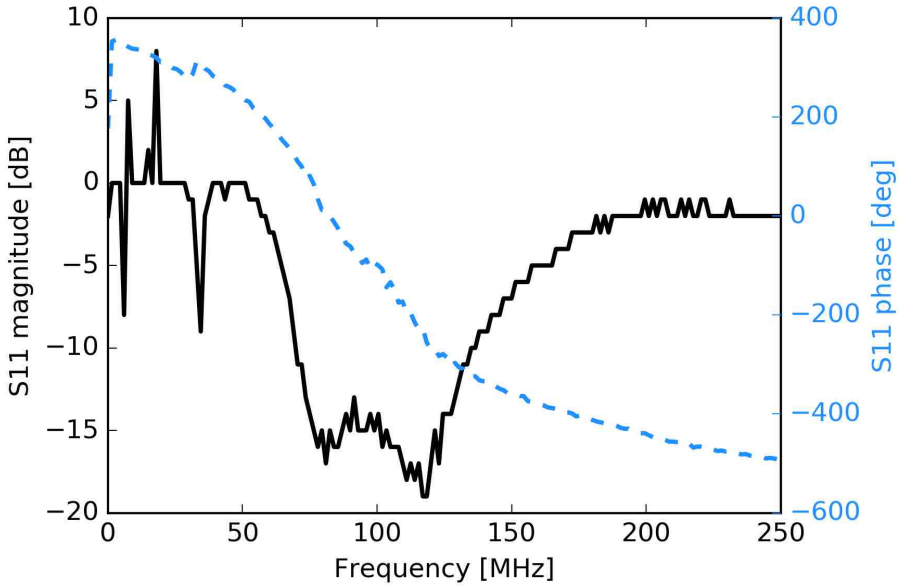

Figure 2.10: Magnitude *(black)* and phase *(blue dashed)* of reflection coefficient for the 100 MHz antenna. These data were taken in April 2017. The positive spikes at $<$20 MHz are unknown leakage, and the step like features are measurement artifacts. The PRI^{Z}M team will make better measurements in April 2019.

Although we trust the qualitative FEKO results, there are nevertheless low-level artifacts in the simulations that we still need to investigate (and this is work in progress).

The antenna simulations predict the return loss to be -10 dB or lower in the designed frequency range (see Figures 2.9 and 2.10). We have performed preliminary S11 measurements to verify the simulation results, but this is still work in progress. Unfortunately, due to onsite challenges and time limitation during the previous takeover voyage, we could not perform repeated measurements. We would be making more precise measurements on both antennas during our upcoming voyage in April 2019.

2.3 First stage electronics

The central column beneath the antenna (left panel of Figure 2.11) houses the first stage electronics (FSE hereafter) box. The fibreglass walls of the column provides necessary shielding

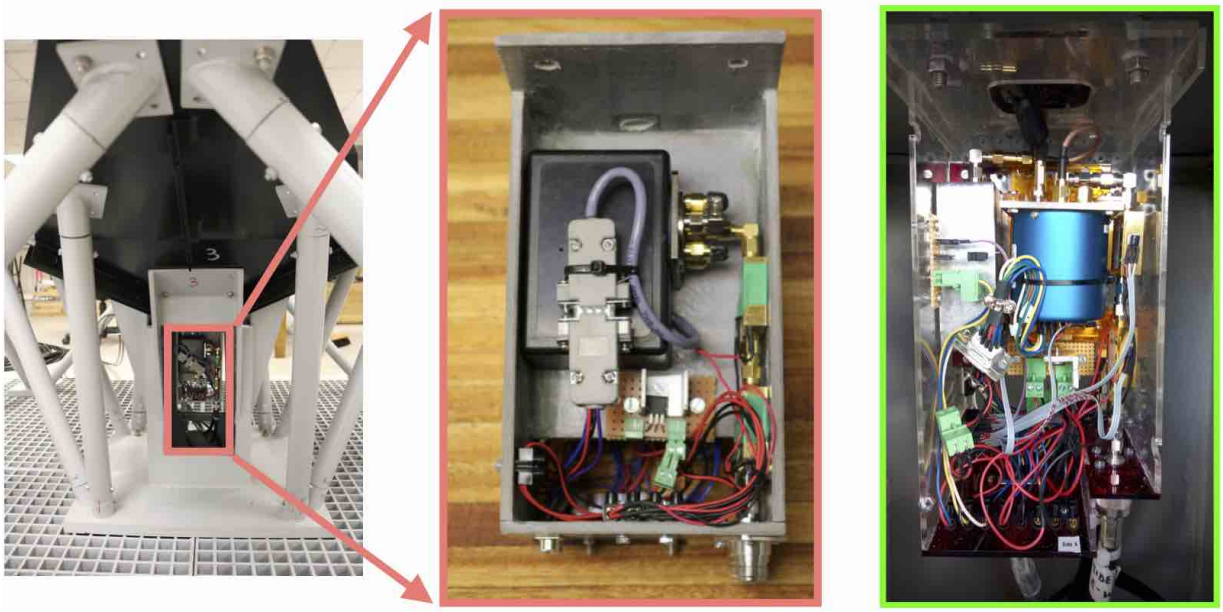

Figure 2.11: The evolution of the first stage electronics box, 2017 *(red inset)* and 2018 *(green inset)*. The box sits inside a cavity in the central column under the antenna.

for the box against various weather elements. The FSE box has a volume of $\sim 200 \times 140 \times 120$ mm^3, and a vertical wall divides it into two halves that cater for orthogonal polarizations. During the installation of PRI^{Z}M in 2017, the FSE box was fabricated using 5 mm thick fibreglass sheet (centre panel of Figure 2.11). However, in 2018 the design was revised and fabricated using 3 mm thick laser-cut acrylic sheets (right panel of Figure 2.11) . There are doors on the opposite walls of the central columns that makes it easier to access the electronics serving individual polarizations of the instrument. The FSE box has a lid to provide thermal isolation from the ambient, and we have installed temperature monitoring system for individual components inside the box (see Section 2.7.2 for details). Moreover, the central column doors are also sealed to provide further shielding from the weather.

Figure 2.12 shows a schematic representation of the FSE. The input from one polarization of the antenna is connected to an electromechanical switch (calibrator switch hereafter, see Section 2.3.1 for details) by a $\sim$200 mm coaxial cable. A ferrite core is clamped on to the coaxial cable in order to dissipate the current on the outer conductor of the cable. Antenna and calibrator

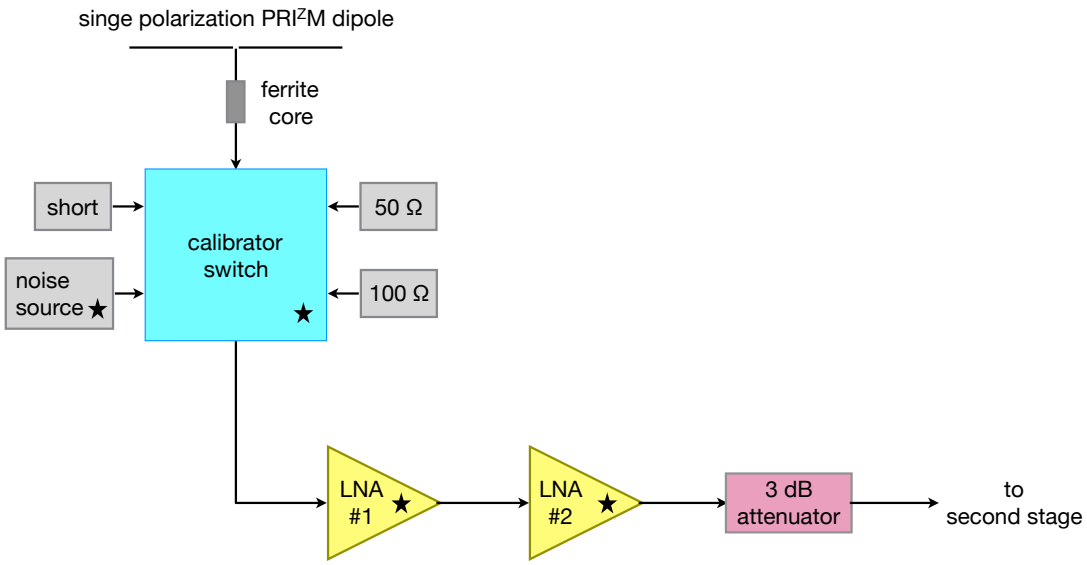

Figure 2.12: A simplified schematic of the first stage electronics. One wire digital temperature sensors are attached to components (marked with ⋆) to record the temperature variation across them.

sources are connected at the input ports of the calibrator switch, and its output is amplified using low-noise amplifiers (LNA, see Section 2.3.2). The FSE box also has additional electronics such as voltage regulation circuits to power the amplifiers and the temperature sensors.

2.3.1 Calibrator switch

The calibration scheme of PRI^{Z}M relies on observing known reference loads (or calibrators) in between sky observations. A calibrator switch is used to toggle between observations of the sky and the calibrator sources that include 50 Ω, 100 Ω, short terminators and a broadband noise source. The antenna and the calibrators are connected to separate inputs of a single pole six throw (SP6T) electromechanical switch (input ports J1–J6 in Figure 2.13).

During the deployment of PRI^{Z}M in 2017, we used Teledyne CCR-38S360 switches with non-latching actuators, and as the name suggests it requires a constant supply of power to latch onto an input. However, in 2018 we upgraded to Teledyne CCR-39S860 latching switches with latching actuators that require short separate pulses (for a maximum duration of 20 ms) in order

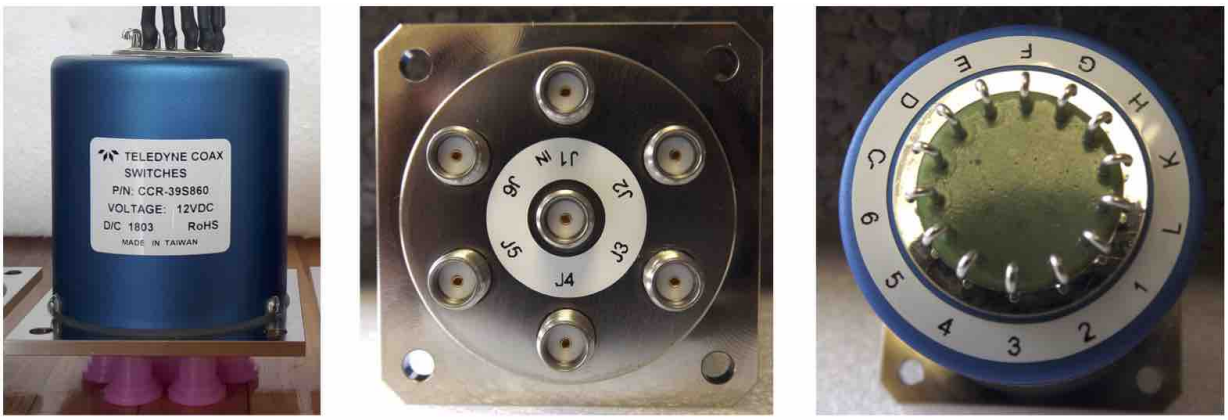

Figure 2.13: A CCR-39S860 SP6T electromechanical switch *(left)* enables switching between on-sky and reference loads observations. There are seven SMA-F ports *(centre)*: the centre port is the output while six peripheral ones (J1–J6) are the input ports to which the antenna and the reference load are connected. The input ports J1–J6 are controlled via ports 1–6 which have J-shaped soldering hooks for electrical interfacing *(right)* and accept TTL signals.

to reset and latch onto a position. The characteristic impedance for both type of switches is 50 Ω, refer Table 2.2 for a comparison between the two switch types.

The CCR-38S360 and CCR-39S860 switches more or less have similar form factor, with the latter being slightly bigger, and therefore the FSE box had to be redesigned for the 2018 upgrade. Figure 2.13 shows the electrical and RF interfaces of the calibrator switch. The maximum soldering temperature at the J-shaped hooks is 250° C for no more than 5 seconds in order to avoid damage to the solenoids. The circuits required to operate both these type of switches are discussed in Section 2.7.1.

PRI^{Z}M uses one electromechanical (EM) switch per polarization, and therefore four in total for two antennas. EM switches have lower insertion loss and higher isolation as compared to solid state (SS) switches. This was one of the main reason we opted for EM switches even though they have larger assemblies as compared to SS switches because they incorporate a series of coils and mechanical contacts. In addition to this, EM switches are not susceptible to electrostatic discharge (ESD).

Table 2.2: Switch characteristics

Parameter	CCR-38S360	CCR-39S860
Actuation voltage	12 V DC	12 V DC
Actuation current	400 mA	255 mA
Reset current	–	1530 mA
Isolation (30–200 MHz)	-90 dB	-90 dB
Insertion loss (30–200 MHz)	≈0 dB	≈0 dB
Power handling (30–200 MHz)	275–375 W	275–375 W
Operating temperature	-40°C to 65°C	-40°C to 65°C
Standard actuator life	5×10^6 cycles	5×10^6 cycles

2.3.2 Low-noise amplifier

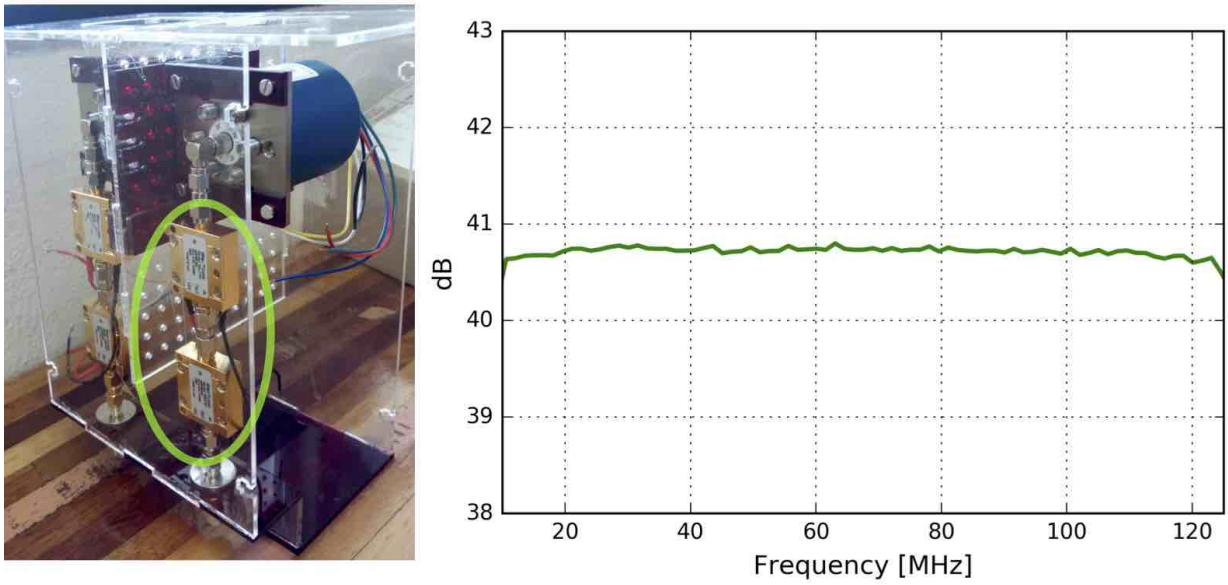

Figure 2.14: *Left*: Two WEA101 LNAs connected in series (inside green ellipse) at the output of each calibrator switch in the FSE box. *Right*: S21 measurement of the two first stage LNAs with 3 dB of attenuation shows a combined gain of ∼40 dB. Within the frequency range shown above, the LNA's have a uniform gain response with a variation of ∼0.03 dB.

In the RF chain, immediately after the calibrator switch, we perform the first stage amplification using two WEA101[4] LNAs in cascade. Each LNA has a low noise figure of 1 dB and a gain of a little over 20 dB in the 0–250 MHz frequency band. One of the main reasons for using WEA101 is because it has a better impedance match with the antenna as compared to Minicircuits ZX60-33LN-S+ amplifier which we use for second stage amplification. Impedance matching between the first stage amplifier and antenna is essential in order to avoid incoming RF signals from being reflected back to the antenna. We also added a 3 dB attenuator after the LNAs to avoid charge buildup on the central conductor of the coax that could potentially damage the LNAs. Figure 2.14 shows the S21 measurement of the first stage amplification chain with a 3 dB attenuation.

2.4 Second stage and readout electronics

The output from the first stage is routed over a 50 m long LMR400 coxial cable to the second stage and readout electronics that are enclosed in a Faraday cage. Moreover, for RFI-proofing and to protect sensitive electronics from the weather, the Faraday cage is placed inside a shipping container as shown in Figure 2.15. The separation between the first and the second stages reduces the risk of contamination from self generated RFI.

Figure 2.15: A wide angle view of a PRI^{Z}M antenna and shipping containers containing the second stage electronics, batteries, generator, fuel and spares. A 50 m long separation between the first and second stages help in minimizing self generated RFI.

[4]http://www.wantcominc.com/DataSheets/WEA/WEA101.pdf

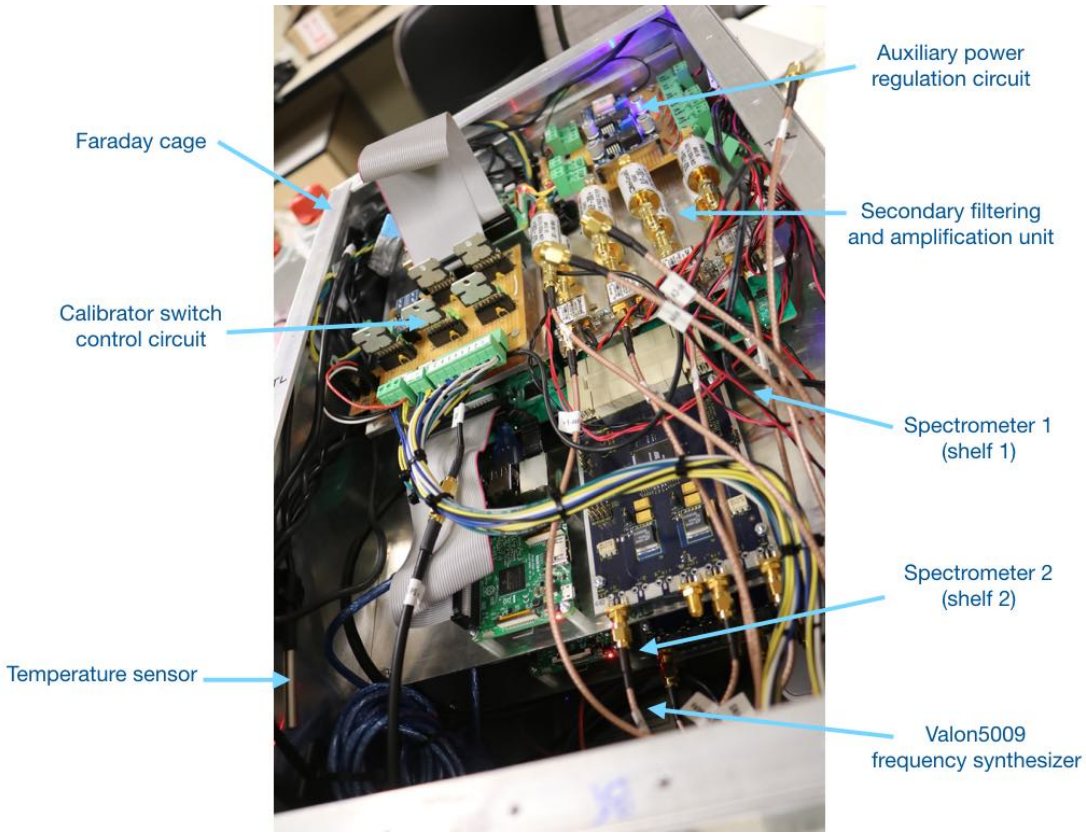

Figure 2.16: The SSE box with its top panel removed reveals the multi-tiered interior. The design of this box is such that most of the internal components can be accessed in this configuration, however, to access the DC-DC converters (hidden in this image), we have to open one more panel (preferably the bottom one).

The second stage electronics (SSE hereafter) box is a custom designed box with a volume of $\sim$300$\times$470$\times$240 mm^3 as shown in Figure 2.16. The box is fabricated using $\sim$2 mm thick aluminum sheet, and with a skeletal framework of right angle brackets. The different layers of the box separates components on the basis of their function and accessibility. A BNC connector is the main power connector on the box, the output of which is filtered using M4C104A DC feedthrough filters, which are 0.1 μF capacitive filters ("C-filters") that provide an attenuation of $\sim$30–40 dB (30–200 MHz) . The C-filters are the most common EMI filters used to remove unwanted ripples, and thereby provide a clean input to the DC-DC converters. There are two DC-DC converters on the bottom layer of the SSE box. Two readout boards (SNAP boards, to

be described in Section 2.5) are powered from a dedicated DC-DC converter, while the other one caters to the remaining electronics inside the box. The bottom layer also has a Valon5009 used as a sampling clock (see Section 2.4.2), and the second stage filtering and amplification unit (see Section 2.4.1).

The two SNAP boards are installed on the two central shelves in the SSE box. The shelves also accommodate the Raspberry Pi (RPi) single-board computers that run the SNAP boards. The position of the shelves stresses on accessibility of the readout electronics, which is a crucial factor for remote onsite debugging activities. The auxiliary electronics and power regulation circuit are mounted on two small shelves above the SNAP boards. Most of the hardware inside the SSE box can be accessed by removing just the front panel. However, in order to access components such as the DC-DC converters, or voltage regulators etc, we have to remove more that one panel. The front panel has all the connectors, mainly for signal, power and communicating to the RPis. There is a GPS receiver inside the box, to which an external antenna is connected for better signal reception (see Section 2.4.3). The SSE box was tested for its RFI-proofness in the reverberation chamber at SKA, SA (see Figure 2.17). The results showed no noticeable RFI signal leak from the SSE box.

The second stage electronics can be classified into two major sections – RF chain and auxiliary hardware (Section 2.7). The RF chain filters and amplifies the incoming signal (see Section 2.4.1) before routing it to the spectrometer (Section 2.5). The schematic in Figure 2.18 shows the signal path.

2.4.1 Filtering and secondary amplification

The second stage filtering chain consists of Minicircuits SLP-200+ low pass and SHP-25+ high pass filters that band limits the RF signal to 30–200 MHz before secondary amplification with a Minicircuits ZX60-33LN-S+ amplifier. Four identical RF chains are used to amplify signals from two dual-polarization antennas (see the left panel of Figure 2.19). The right panel of Figure 2.19 shows the band limit applied by the filters, and the amplifier gain for one of the chains. The ZX60-33LN-S+ amplifiers operates on 5V and has a power draw of $\sim$0.35 W, all

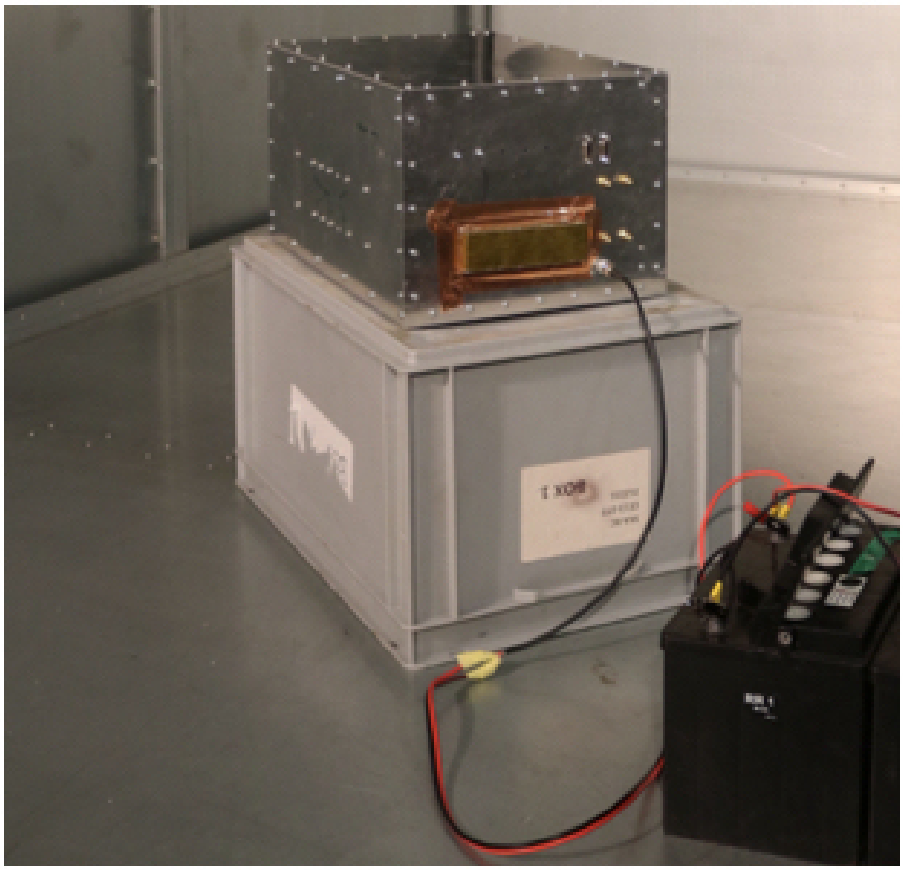

Figure 2.17: The SSE box is sealed and tested in the reverberation chamber at SKA-SA. For testing purposes, the input power is supplied using two car batteries. In order to ensure RFI tightness, the Ethernet ports on the front panel of the box are covered with a brass lid during observations.

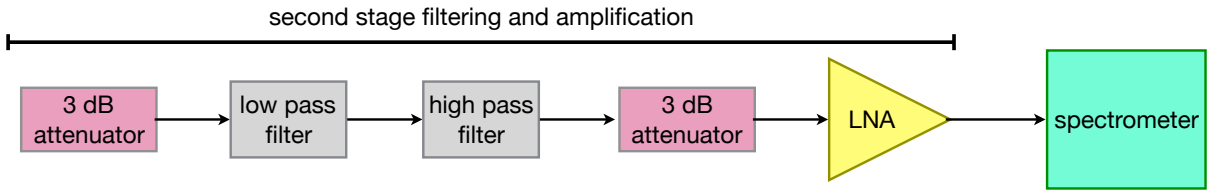

Figure 2.18: A simplified schematic of the back end electronics illustrating the second stage filtering and amplification circuit connected to the spectrometer.

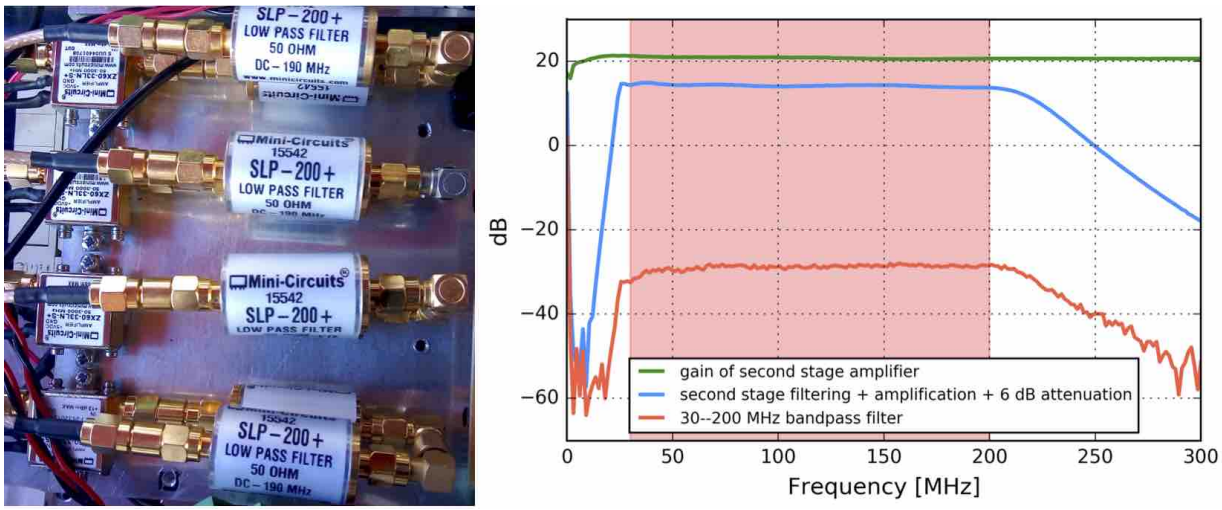

Figure 2.19: *Left*: Four identical second stage RF chain. *Right*: S21 measurements of the : Minicircuits ZX60-33LN-S+ amplifier gain *(green)*, the band limiting by Minicircuits SLP-200+ low pass and SHP-25+ high pass filters *(red)*, and the second stage filter + amplifier output with 6 dB attenuation in *blue*. The 30–200 MHz pass band is highlighted in red.

four amplifiers therefore has a combined power draw of $<$1.5 W, and are powered by the auxiliary power regulation circuit.

Also present in this chain are two 3 dB attenuators that are placed before and after the filtering stage. After filtering and amplification, the output signal is passed to the readout electronics (more in Section 2.5).

2.4.2 Sampling clock

PRI^{Z}M uses a Valon 5009[5] dual frequency synthesizer module (shown in Figure 2.20) as a sampling clock to sample the input analogue signals. The Valon 5009 is programmed to generate a periodic waveform, and this signal supplied to two 8-bit AT84AD001B ADCs via a RF splitter. The loss in the RF splitter is negligible compared to the typical 15 dBm output of the Valon 5009. Moreover, the Valon's non-volatile flash memory needs to be programmed in order to retain the state of its outputs even after a power cycle. The Valon5009 has two ouput ports (or synthesizers,

[5]https://www.valonrf.com/frequency-synthesizer-6ghz.html

Figure 2.20: A Valon5009 dual frequency synthesizer. The two output ports (Source 1 and Source 2) can be locked either to an internal or to an external frequency reference.

Source 1 and Source 2); and both synthesizers are locked to a 40 MHz internal high-stability, low phase noise, precision analogue compensated Voltage Controlled Temperature Compensated Crystal Oscillator (VCTCXO). Typical frequency error is less than 1 ppm while the stability over the -30 °C to 70 °C is less than 0.5 ppm. We program Source 1 to output 500 MHz. The programming is done in Python scripting language, and the steps are described in Appendix A. The Source 2 port serves as a backup, and be programmed on the fly to generate on-field test signals of interest whenever needed.

2.4.3 System clock and GPS

The RPi model used by PRI^{Z}M does not have a real time clock (RTC). Therefore the RPi clocks are synced to an Adafruit[6] global positioning system (GPS) receiver (left panel of Figure 2.21) prior to the start of every observation cycle. The GPS receiver used by PRI^{Z}M can operate either on 3.3 or 5 V DC, and is connected to the RPi via a USB to serial converter module. On power-on, the GPS receiver initiates a sequence to connect to the host of GPS

[6]https://www.adafruit.com/product/746

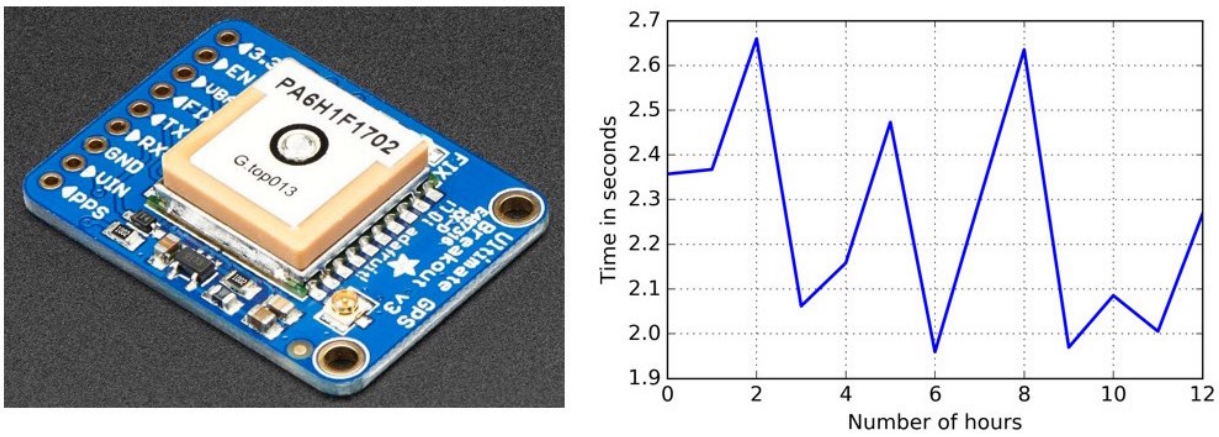

Figure 2.21: *Left:* An off-the-shelf GPS patch receiver from Adafruit. *Right:* Difference between the GPS and RPi clocks over a period of 12 hours.

satellites orbiting overhead. The RTC of the GPS receiver is synced with the atomic clocks on board the GPS satellites. The power from a coin battery in the receiver preserves the RTC sync in the event of a power cycle. After the GPS module is synced to the satellites, we use the GPS NMEA[7] data to set the RPi system clock. The RPi system clock drifts with time, and presently we do not correct the drift in situ with the observation. In the future revisions, precision RTC modules will be integrated with all the RPis in the PRI^{Z}M system.

2.5 Spectrometer

PRI^{Z}M employs two Smart Network ADC Processor (SNAP[8], Hickish et al., 2016) boards to read out and process the analogue RF signals. Each SNAP board accepts two RF inputs corresponding to the two polarizations from a single antenna. The input signals are sampled at 500 Msamp/s using a dual, monolithic, eight-bit, AT84AD001B analogue-to-digital converter (ADC). As shown in Figure 2.22, the ADC is an external unit that attaches to the SNAP board via a Z-Dok connector. The clock signal for the ADC is provided by a Valon 5009 frequency syn-

[7] https://www.gpsinformation.org/dale/nmea.htm
[8] https://casper.berkeley.edu/wiki/SNAP

thesizer (Section 2.4.2). The SNAP board is equipped with a Kintex 7[9] field-programmable gate array (FPGA) that is programmed with spectrometer firmware that performs Fourier transform routines to generate auto- and cross-spectra for the two digitized input signals. The firmware is generated using a block diagram environment called Simulink. It is combined with MATLAB to create a simulation environment that supports both textual and graphical programming.

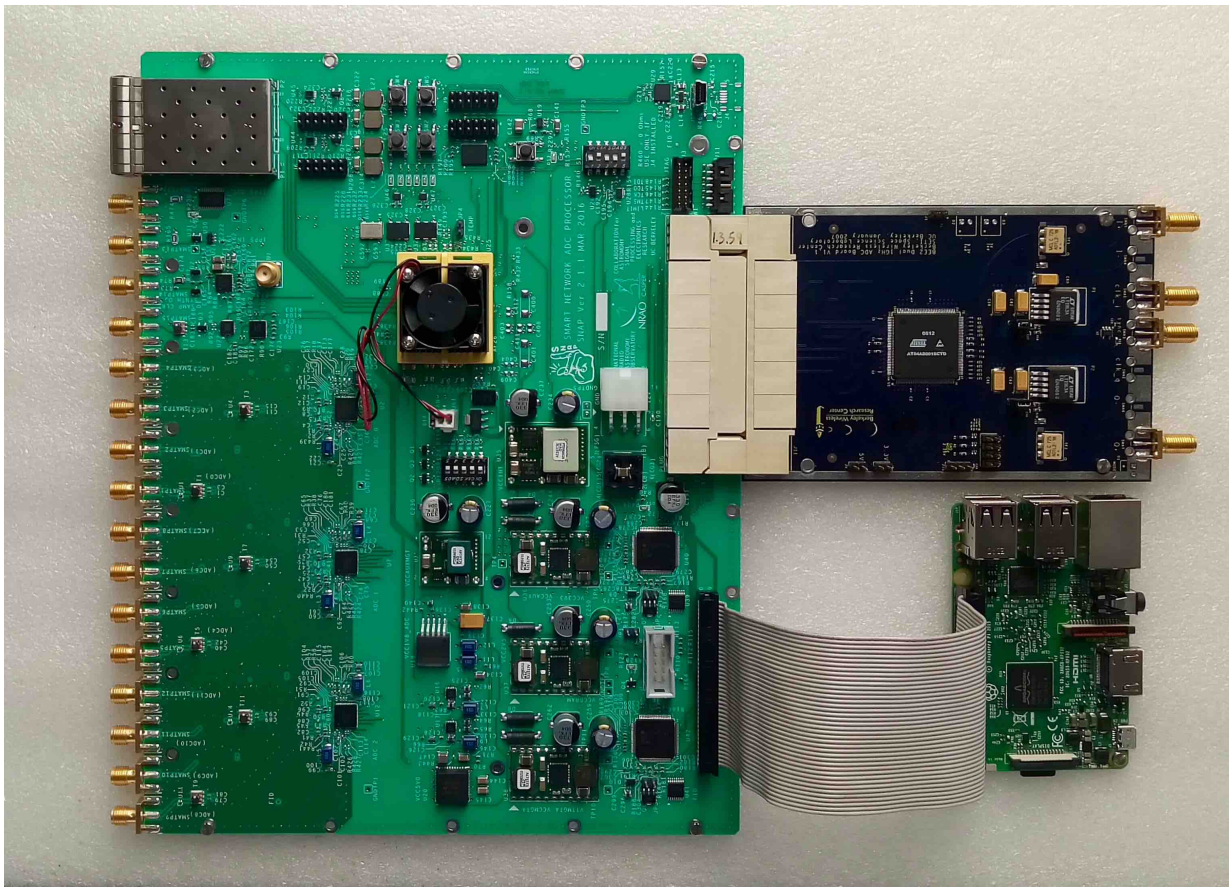

Figure 2.22: SNAP board (left) with external AT84AD001B ADC *(upper right)*. Initialization and data acquisition is done using a Raspberry PI *(lower right)* that connects to the SNAP board via a 40-pin general purpose input output (GPIO) ribbon cable.

Figure 2.23 is a graphical representation of the latest firmware version for PRI^{Z}M. We notice that the design is a combination of yellow, green and white blocks. The yellow blocks

[9]http://www.xilinx.com/products/silicon-devices/fpga/kintex-7.html

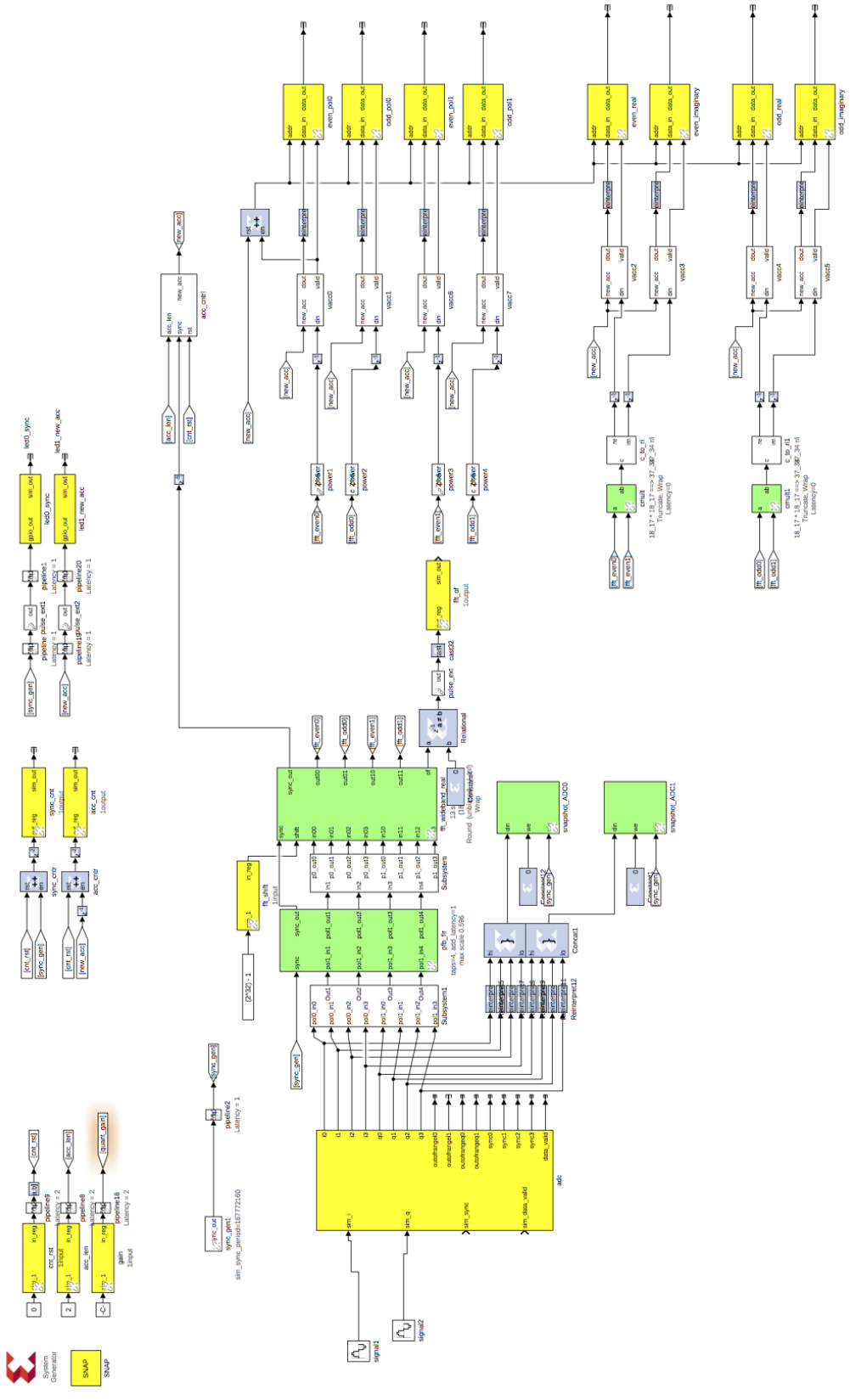

Figure 2.23: The PRI^{Z}M firmware designed using the MATLAB-Simulink package is represented in a graphical environment. The yellow blocks are used for communicating to the outside world.

are CASPER[10] modules that pass inputs/outputs to/from the firmware. The rest are Xilinx and standard Simulink blocks that perform several digital signal processing functions. Since SNAP board is developed by the CASPER group, we use the CASPER toolflow[11] to compile the design and generate the firmware.

In the PRI^{Z}M firmware, the incoming analogue signal after getting sampled by the ADC passes through a polyphase filter bank (PFB). The PFB module helps in suppression of out-of-band signal and also produces a flat response across the channel. The PFB module consists of two main blocks – *pfb_fir* and *fft_wideband_real* blocks (green blocks in Figure 2.24). The *pfb_fir* block is responsible for applying finite impulse response (FIR) filters by dividing the input signal into parallel taps. The output of the *pfb_fir* block is a time-domain signal that gets converted into the frequency domain by fast Fourier transform (FFT) butterfly biplex algorithms in the *fft_wideband_real* block. A FFT butterfly has 2^n inputs and 2^n outputs with n layers of twiddle stages in between, and in biplex, the FFT can process two input data streams simultaneously by time multiplexing hardware. Moreover, in the FFT butterfly algorithm, half of the inputs are combined with the other half at any twiddle stage, and therefore when one stream is buffered, the other input stream is processed. The *fft_wideband_real* block only processes the real data.

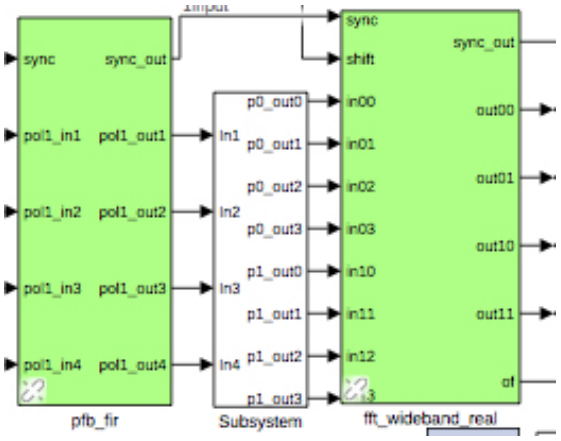

Figure 2.24: The polyphase filter bank comprising of FIR filter and FFT blocks represented using blocks in MATLAB-Simulink block design environment.

[10]Collaboration for Astronomy Signal Processing and Electronics Research

[11]https://casper.berkeley.edu/wiki/Toolflow

2.6 Data acquisition

The resulting spectra span 0–250 MHz with 4096 frequency channels (∼61 kHz resolution) and are recorded roughly once every four seconds. A RPi is used to communicate with the SNAP board, run the data acquisition (DAQ) software, and store data. Chapter 4 discusses the preliminary analysis of raw science data.

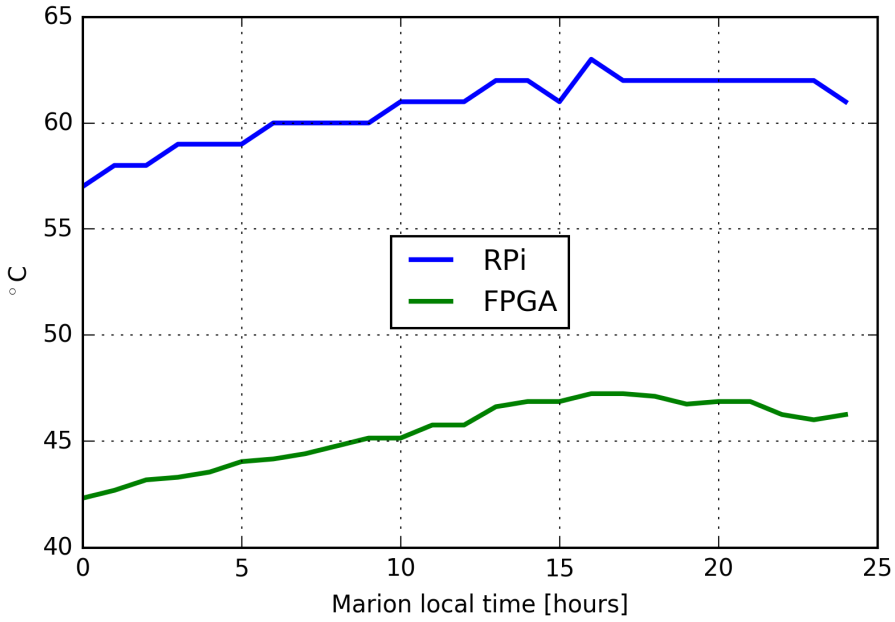

Figure 2.25: Core temperatures of RPi and SNAP FPGA over a 24 hour period. The 0 hour corresponds to midnight on Marion Island.

In addition to the science data, we also record the state of several other parameters for housekeeping purposes. These parameters include the time taken by the SNAP board to accumulate a spectra, the overflow parameter of the 8-bit FFT, and the core temperatures of the FPGA and the RPis etc. Any deviation from normal values of these parameters trigger respective debugging steps. For example, the maximum operating temperatures for the RPi and SNAP FPGA are ∼85° and ∼60° respectively, we therefore monitor their temperatures (Figure 2.25) during our observation to gauge their performance.

In April 2018, we modified the PRI^{Z}M DAQ to include supervisord[12], a process control system that allows monitoring and controlling of multiple processes on UNIX-like operating systems. Supervisord is configured to start DAQ automatically within 2 minutes after the instrument is powered on. All processes and subprocesses are monitored by supervisord, and is programmed to automatically restart them on a crash. It also periodically outputs the log and error files which are helpful during debugging.

Data from both 70 and 100 MHz systems undergo similar compression and are stored in micro-SD cards on the RPis. We employ bzip2 compression to reduce the raw data file sizes by a factor of $\sim$2.7. The data are stored as 15 minute observation files. Each 15 minute dataset is $\sim$19 MB in size, and therefore both systems have a combined data rate of $\sim$3.6 GB per day. Each dataset contains auto- and cross-spectra files from the respective systems (either 70 or 100 MHz), along with the SNAP board housekeeping files. Some of the generated files are:

- East-West auto-spectra data
- North-South auto-spectra data
- cross-spectra data (real and imaginary)
- start time of each spectrum (from the system clock)
- stop time of each spectrum (from the system clock)
- start time of each spectrum (from the GPS real-time clock)
- stop time of each spectrum (from the GPS real-time clock)
- accumulation time of the SNAP FPGA for the East-West auto-spectra
- accumulation time of the SNAP FPGA for the North-South auto-spectra
- FFT overflow indicator
- FFT bit shifting indicator
- temperature of the FPGA
- temperature of the RPI

[12]http://supervisord.org/

2.7 Auxiliary hardware

The Faraday cage that encloses the second stage and readout electronics also houses a set of auxiliary hardware. The auxiliary hardware has dedicated operations such as controlling the calibrator switch state, and power regulation etc.

2.7.1 Calibrator switch control circuit

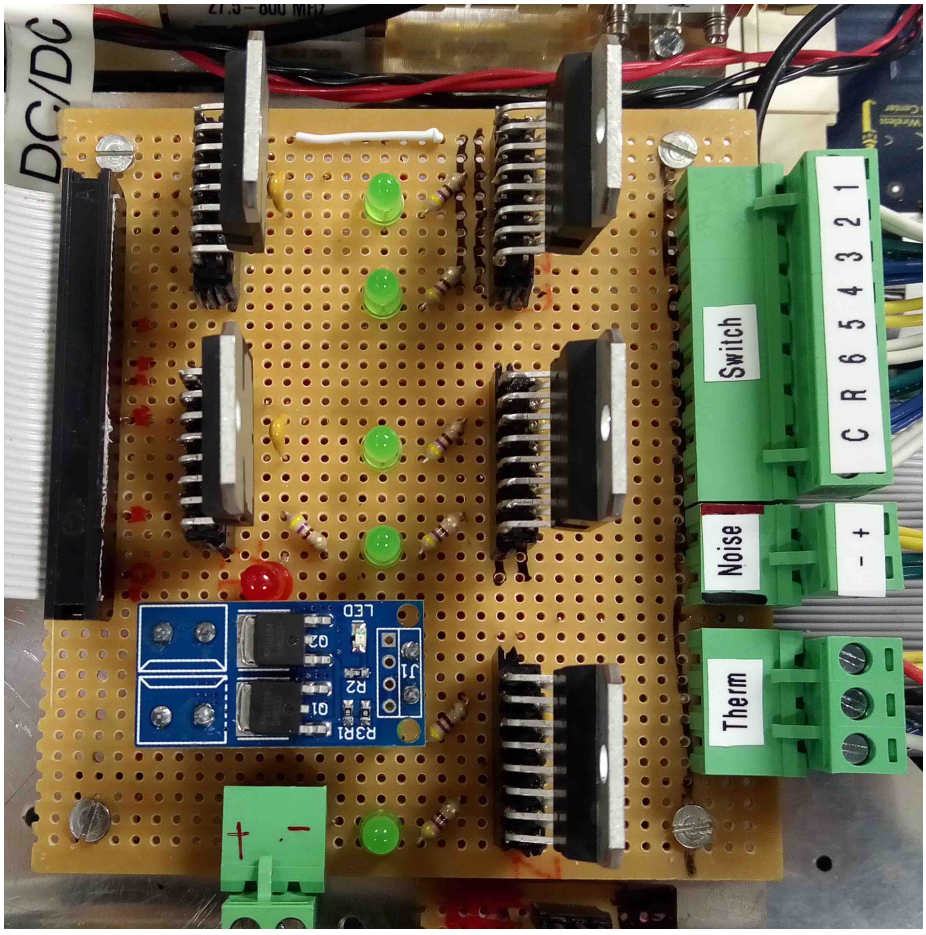

Figure 2.26: The switch control circuit installed in April 2018 to drive the latching calibrator switches in both antennas. The components were assembled on a perfboard and operated using a RPi (not shown in this image) that is connected to the GPIO ribbon cable on the left. Addition of latching switches was one of the major upgrades in 2018.

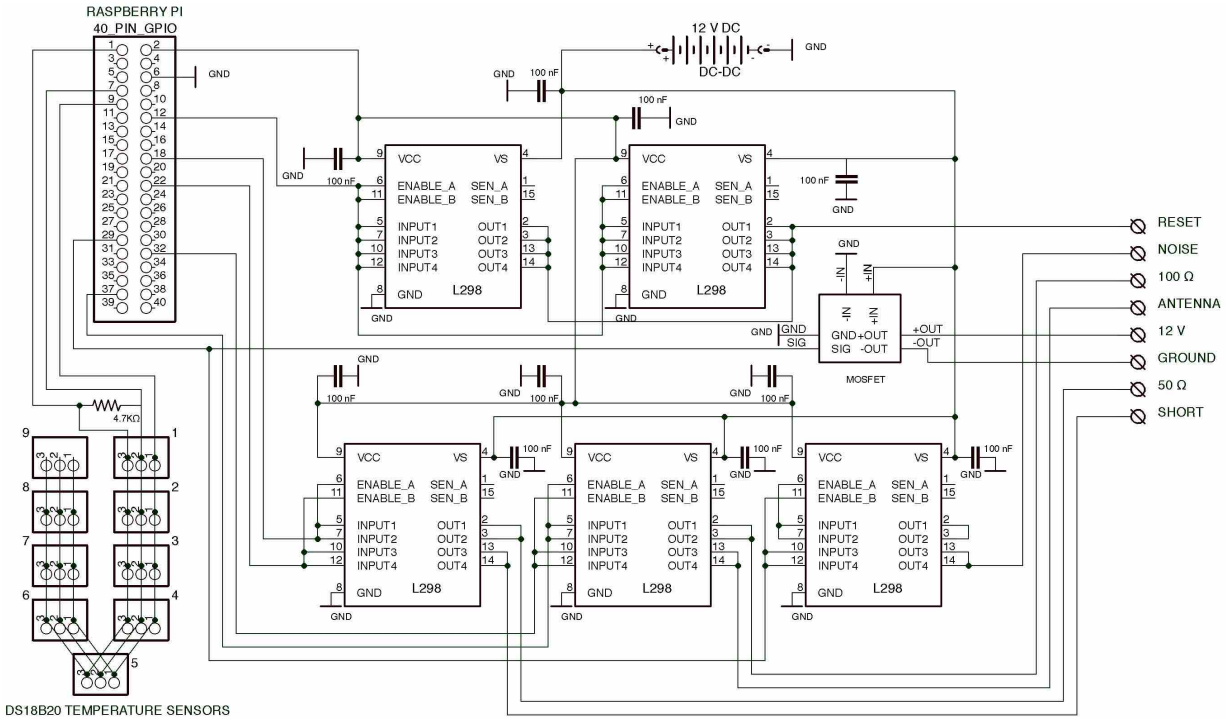

Figure 2.27: 2018 : A circuit to operate four CCR-39S860 electromechanical switches. We use five L298 high-current full-bridge drivers to provide the reset (using the top two L298s) and actuation (using the bottom three L298s) signals. A power mosfet is used to turn ON/OFF a noise source in the FSE box. The TTL signals are provided by a RPi. The circuit also has nine DS18B20 1-wire sensors for temperature feedback.

PRI^{Z}M has of four calibrator switches that cater two polarizations in each of the two antennas. All four switches are operated by one master switch control circuit that is enclosed in the Faraday cage along with the second stage and readout electronics. The control signals are generated using transistor-transistor-logic (TTL) using integrated chips that meets the required output current limit for the combined power draw of all the switches. A RPi model 3 runs Python script that programs its GPIO pins in order to control the logic gates of the integrated chips.

Figure 2.26 shows the switch control circuit assembled on a perfboard to drive the CCR-39S860 latching switches. Adding latching switches was an upgrade done in April 2018. To make the control circuit, I used L298 full bridge drivers that are capable of handling high current and voltage to input the reset and position select pulses to the latching switches (see Figure 2.27).

Previously, in 2017, PRI^{Z}M was installed to Marion with CCR-38S360 non-latching switches. To operate the switches, I designed a control circuit using ULN2003A high voltage high current Darlington transistor arrays. One ULN2003A chip has seven drivers that outputs a maximum of ∼500 mA each. During testing we found that the combined current draw for all four switches was beyond the maximum rating of an individual ULN2003A driver. Therefore, the circuit was parallelized and the total load of four switches was distributed over four ULN2003 chips as shown in Figure 2.28.

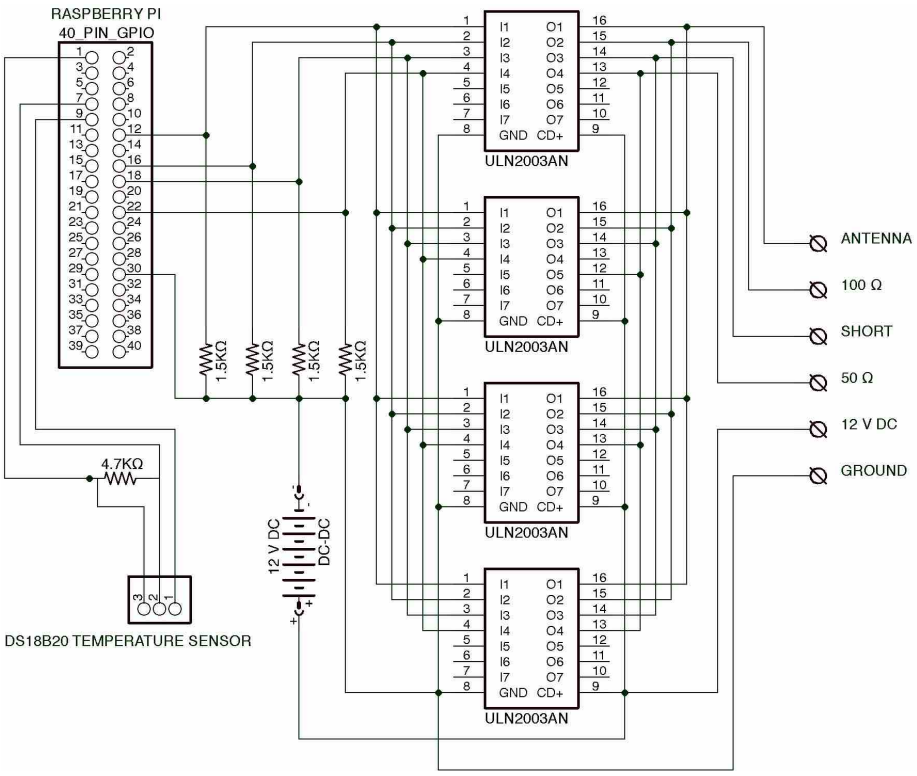

Figure 2.28: 2017 : Four ULN2003AN chips connected in parallel to operate four CCR-38S360 switches. Each of the seven NPN Darlington transistors on a single ULN2003AN is capable of 500 mA, 50 V output. The TTL signals are provided by a RPi, and a DS18B20 1-wire sensor is used to record the temperature inside the PRI^{Z}M receiver.

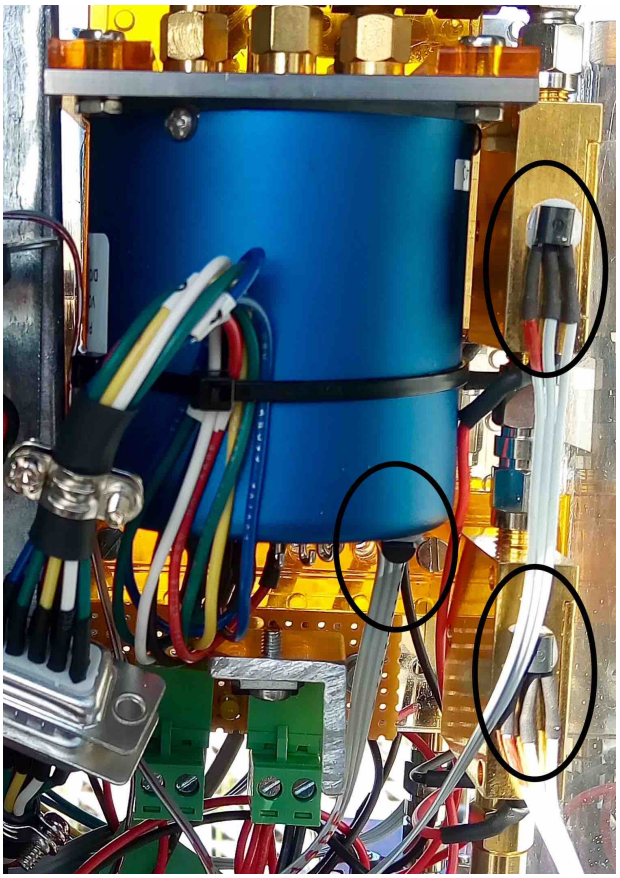

Figure 2.29: Zooming in onto a section of the FSE box shows a subset of 1-wire DS18B20 temperature sensors *(circled)* glued to the calibrator switch and the LNAs in one of the polarizations. There are nine DS18B20 temperature sensors in each FSE box.

2.7.2 Temperature monitoring circuit

The temperature monitoring circuit is for housekeeping purposes and provides additional data to verify component performance. Each FSE box has nine 1-wire DS18B20 (Figure 2.29) temperature sensors to record temperatures across 4×LNAs, 2×calibrator switches, 2×noise source circuit that cater two polarizations and 1×ambient temperature reading. Figure 2.30 shows the temperature profile of the components in the East-West polarization of the 70 MHz FSE box over a period of ∼2 days.

DS18B20 temperature sensors are 1-wire digital thermometers with unique serial codes that makes it easy to connect multiple sensors to a single RPi (see Figure 2.27). The sensors have

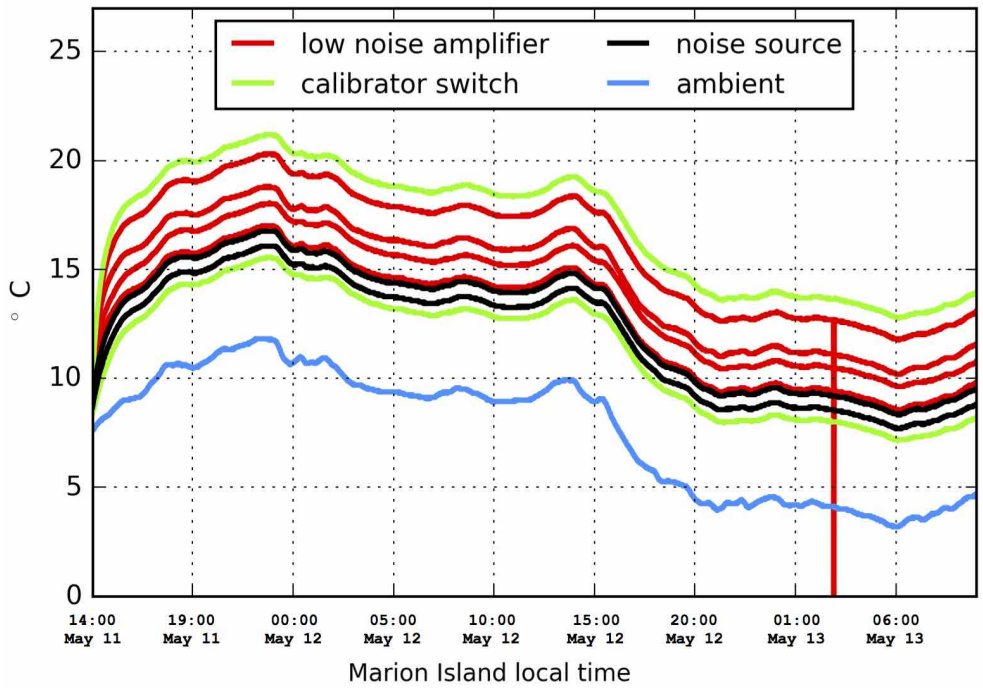

Figure 2.30: Temperature profile of LNAs *(red)*, noise sources *(black)*, calibrator switches *(green)* and ambient *(blue)* inside the 70 MHz East-West polarization FSE box recorded on 11–13 May, 2018. The diurnal temperature variation is visible in the plot. The brief dropout on the right is due to a glitch in the data from a sensor on one of the LNAs.

a TO-92 package with three pins : ground, data and 3.3 V power line. The circuit also requires a 4.7k (or 10k) pullup resistor between the data and power pins. DS18B20 has a precision of $\pm 0.5°$C over an operating temperature range of $-55°$C to $125°$C. The RPi issues a read command each time during a temperature read, and all the nine DS18B20 sensor outputs are serially read via a single data line in our system.

2.7.3 Power distribution circuit

The entire PRI^{Z}M system is powered using eight 12-V, 200-Ah Lead Crystal batteries that are wired in parallel as shown in Figure 2.31. The total system power draw is $\sim$65 W, and PRI^{Z}M can operate without interruption for $\sim$1 week when the batteries are fully charged.

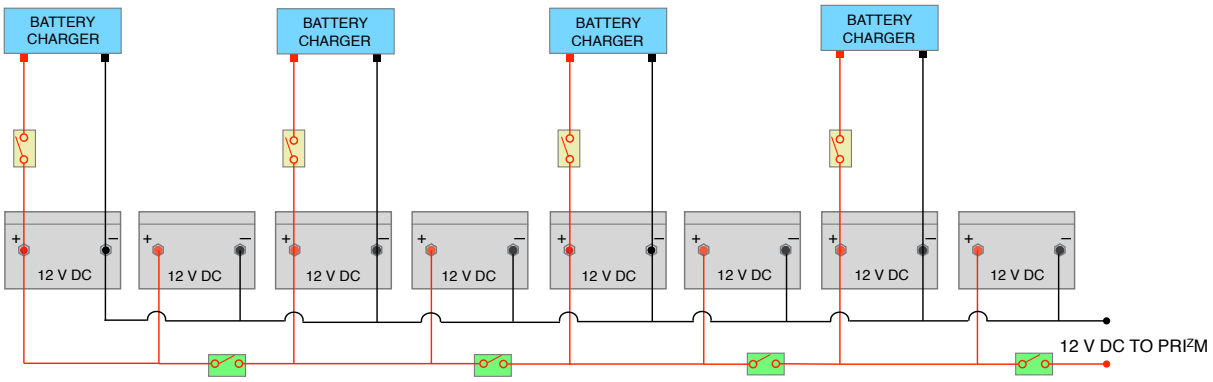

Figure 2.31: Power distribution chain of PRI^{Z}M consists of eight lead crystal batteries *(grey blocks)* of 200-Ah each. The batteries operate in pairs that are cascaded together via the green switches. During charging, the battery pairs are disconnected and a single battery charger *(blue blocks)* can charge two batteries. The yellow switches are used to operate the battery chargers. During observation, all yellow switches are powered OFF and all green switches are powered ON.

Battery charging is performed using a Honda EU30is[13] generator and a fuel cache that is kept at the PRI^{Z}M observing site. During observations, the batteries are connected to two DC/DC converters – one powering the SNAP boards, and the other one powering auxiliary hardware. The DC-DC converters are housed inside the Faraday cage and provides stable 12 V outputs despite the slow decline of the battery voltage. There are additional power regulators that supply lower voltage levels to several components in the system.

[13] http://www.hondaenergy.com/generators/honda-eu30is.html

CHAPTER 3

Observing site and RFI characterization

3.1 Overview

Even though global signal experiments theoretically require only a few hours of data to attain the necessary signal to noise ratio, the observation is mainly dominated by systematics. Besides, observational challenges include bright astrophysical foregrounds described in Section 1.3 and the Earth's ionosphere (Section 3.6.1). Another problem facing low frequency radio astronomy is man-made radio frequency interference (RFI). RFI signals emanate from a diverse range of man-made sources. Among these, the FM radio transmitters are the biggest contributors of RFI in the low-frequency regime ($<$200 MHz). Furthermore, the radio frequency spectrum is getting more crowded due to the technological advancement, thus, spilling RFI signals into observation bands. The enormously sensitive radio telescopes are capable of picking up RFI signals that travel miles from their source of origin, yet are several orders of magnitude stronger than the weak celestial signals of interest.

A solution to this problem is observing from sites that are far away from RFI transmitters. The radio environment at potential sites must be verified prior to significant instrument devel-

opment and/or observations. Often for such observing sites, there exists a trade-off in terms of access to the site. Therefore choosing a good observing location is generally a balance between accessibility and radio-quietness. Taking all these into account, we chose Marion Island as the observing location for PRI^{Z}M. Marion has a pristine radio quiet environment, however, with an annual access. The next section discusses our site in detail.

3.2 Marion Island

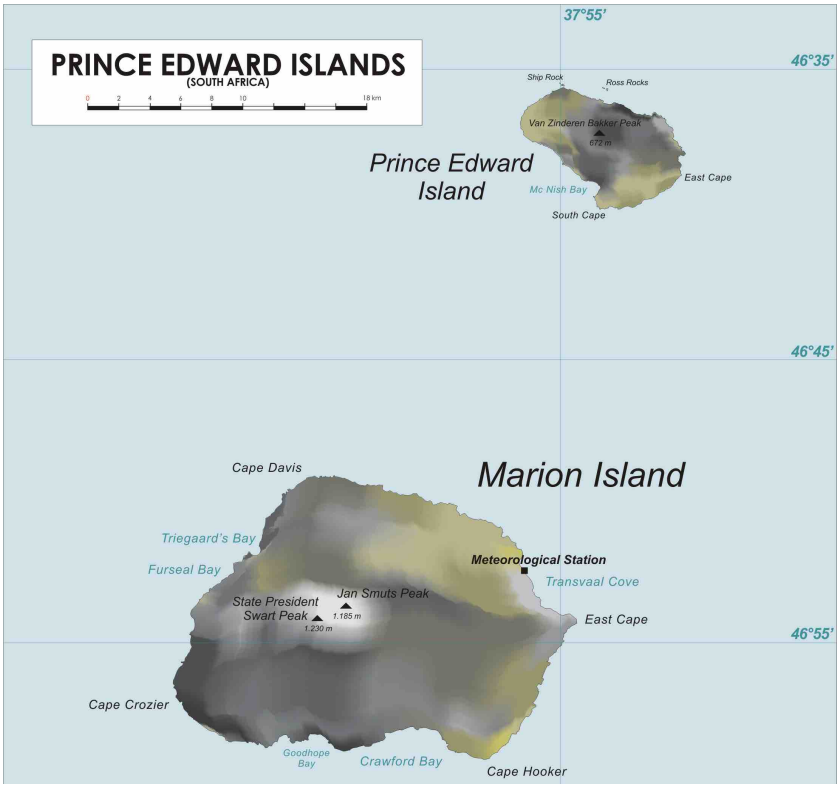

Figure 3.1: The Prince Edward Islands are two small islands : Marion island and Prince Edward Island, in the sub-antarctic Indian ocean.

Marion Island, located at 46°54′45″S, 37°44′37″E, is one of the two sub-antarctic islands that form a part of the Prince Edward Islands (PEI; Figure 3.1) in the Southern Indian ocean. PEI is a part of South Africa, and Marion Island hosts a research station (Figure 3.2) that is operated by the South African National Antarctic Programme (SANAP) and the Department of

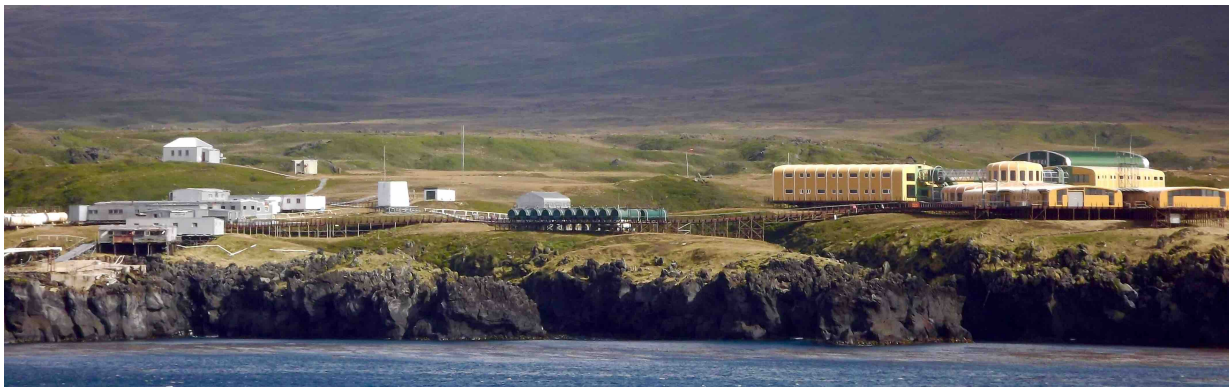

Figure 3.2: The new base (*right,* yellow buildings) and the jettisoned old base (*left,* white buildings) on Marion Island. The emergency base is partially visible in green behind the new base, it serves as a helipad and a hangar for helicopter operations.

Environmental Affairs (DEA), South Africa. Marion Island is about 2000 km away from the nearest continental land masses.

The area of the island is $\sim$290 km^2, and the main research base is situated on the northeast side. Marion Island has a volcanic origin and the terrain is scattered with many secondary craters and small lakes. There is abundant snow and rain, and, the vegetation is mainly mosses and ferns. The lowland regions are marshy due to high precipitation. It is extremely windy and mostly cloudy throughout the year.

Every year in April, Marion Island is serviced by S. A. Agulhas II[1], a South African ice-breaking polar supply and research ship owned by the Department of Environmental Affairs (DEA). The relief voyage in April lasts for a little over one month, however, the travel time shortens it and leaves us with only $\sim$3 weeks on the island. Marion is open to diverse fields of research such as botany, geology, meterology, mammalogy, ornithology, etc. The main base at Marion accommodates all the researchers participating in the relief voyage, and also provides living quarters to the overwintering team members. There are nine huts with attached pantries (see Figure 3.3, and refer Table 3.1) that serve as resting stations for researchers traversing the island.

[1] https://en.wikipedia.org/wiki/S._A._Agulhas_II

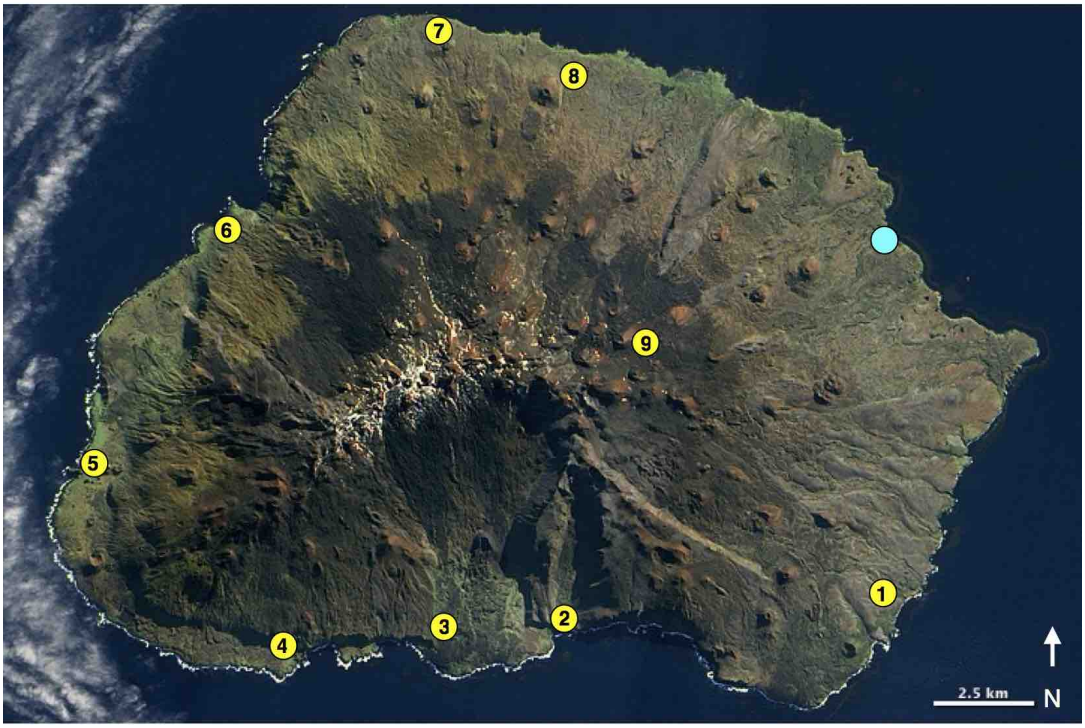

Figure 3.3: Satellite image of Marion Island with field huts (1–9, refer Table 3.1 for hut details) shown using yellow markers , and main base using a cyan marker.

PRI^{Z}M is the first radio astronomy experiment to be installed on Marion Island. All our expeditions to Marion Island are funded by the South African National Antarctic Programme (SANAP). In the subsequent sections, I will provide a walk through of my voyages to Marion Island.

3.3 My voyages to Marion Island

The voyage sets sail from Cape Town, South Africa in the month of April each year. The preparations for the relief voyage begin months in advance. The first step is multiple sessions of brainstorming and deciding upon the goals for the relief voyage. It is followed by an intense development and testing phase during when we improve our designs to increase the robustness

Table 3.1: Huts on Marion (clockwise from the main base, as marked in Figure 3.3)

Name	Longitude	Latitude
Main base (new)	37°51′30.76″	-46°52′31.75″
1. Kildalkey	37°51′11.82″	-46°57′17.1″
2. Watertunnel	37°44′55.39″	-46°57′43.77″
3. Greyheaded	37°42′31.1″	-46°57′42.63″
4. Rooks	37°39′36.41″	-46°58′0.89″
5. Swartkop's	37°35′37″	-46°55′32.4″
6. Mixed pickle	37°38′20.02″	-46°52′19.95″
7. Cape Davis	37°42′30.74″	-46°49′42.04″
8. Repetto's	37°45′12.05″	-46°50′17.55″
9. Katedraal	37°46′28.5″	-46°53′50″

of the system that is to be deployed. As mentioned earlier, the PRI^{Z}M instrument in its entirety is developed in the radio astronomy lab at the UKZN, Durban, South Africa. Since 2016, I have been actively involved in the development of PRI^{Z}M instrumentation. I have provided a brief outline of my role during each of the relief voyages to Marion in the following subsections.

3.3.1 2016 relief voyage

In 2016, I was part of a three-person team that performed the maiden engineering installation for low-frequency astronomy on Marion Island. We installed an experiment called SCI-HI (Voytek et al., 2014), which is the predecessor of PRI^{Z}M. Our team had multiple goals – 1. test Marion Island to confirm that it is suitable for low frequency astronomy 2. RFI characterization of the island 3. field testing of SNAP boards. I was in charge of the data acquisition using SNAP board, and this was the first time a SNAP board was used for science in the field. The installation of SCI-HI was only for the 2016 takeover voyage, and no SCI-HI hardware was left behind on Marion.

Figure 3.4: The SCI-HI experiment installed on Marion during the relief voyage of April 2016. The PVC support structures failed to stabilize the antenna, and therefore it had to be tied down using nylon ropes. The orange shipping container housed backend electronics, batteries, generator, fuel and spares.

Figure 3.5: A Workman T-600 antenna hooked up to a Rhode & Schwartz spectrum analyzer (not visible in the photo) set up at one of the RFI survey locations on Marion.

3.3.1.1 Site selection and installation challenges

The SCI-HI 100 MHz antenna was installed near a field hut called Rooks on the south west side of the island (Figure 3.4), with a primary aim to observe far away from the main base and its locally generated RFI. The system was powered using 12 V car batteries, with recharging done in the field using a small 650 W portable petrol generator. The entire system fit inside a single container, which was air-lifted by helicopter to the deployment site. The short takeover schedule on Marion and weather uncertainties led to us having only twelve days on site at Rooks. SCI-HI was previously deployed to a few locations across North America, and a remote island called Guadalupe, which is off the coast of Mexico. However, for the 2016 voyage to Marion, the original SCI-HI backend underwent a major upgrade to include a SNAP board and two RPis. One of the RPis controlled the SNAP board, while the other one operated the calibrator switch. I designed the calibrator switch circuit as described in Section 2.7.1, and was responsible for the data acquisition using the SNAP board.

Due to our inexperience with the Marion terrain, there were a lot of challenges to overcome. Our primary challenge was anchoring the antenna support structure to withstand the roaring forties on the island. The extremely soft nature of the terrain at our deployment site did not play well with the largest of our anchors, and therefore we had to devise clever ways to anchor the antenna setup. On four occasions we had to move out to nearby field huts (Greyheaded and Watertunnel) in order to accommodate teams of birders and sealers at Rooks. These efforts resulted in shortening our already compressed schedule on site.

3.3.1.2 RFI characterization

During this voyage, one of our team members used a Workman T-600 antenna and a Rhode & Schwartz spectrum analyzer (Figure 3.5) to map the RFI profile of Marion. Spectra were recorded at different locations on Marion (markers in Figure 3.6). RFI profiling of Marion was crucial in identifying potential observing sites for future deployments. Preliminary analysis of the RFI survey data indicates that although the main base generates local RFI, there is no visible contamination at any of the field huts.

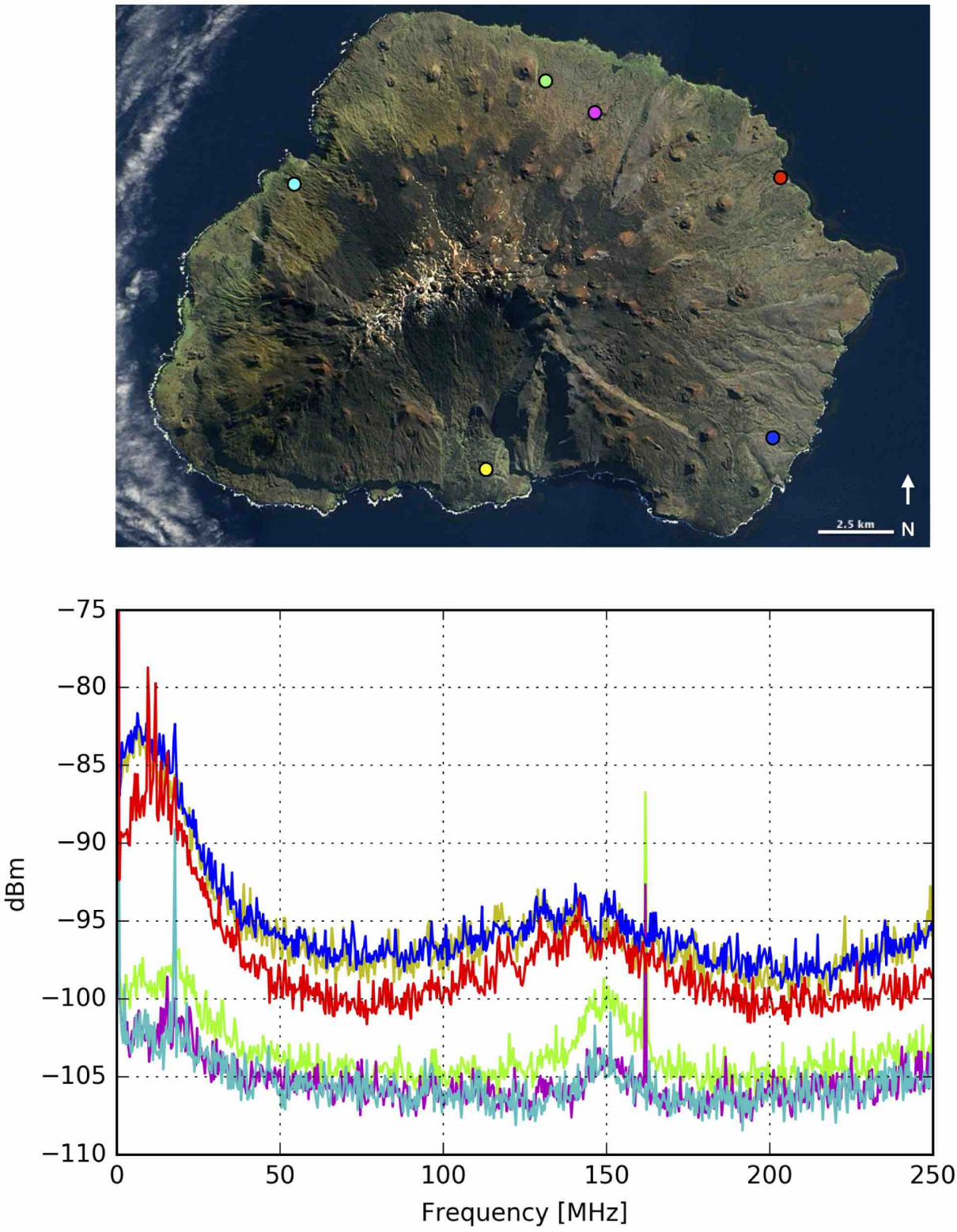

Figure 3.6: The markers on Marion map *(top)* indicate some of the RFI survey locations during the 2016 voyage. The bottom panel shows the spectra recorded at each location. The spike at ∼162 MHz is from the ship's transponder. The colours in the plot correspond to the marker colours in the map. The *yellow* and *blue* sites have an increased power level possibly due to incorrect settings on the spectrum analyzer..

In Figure 3.6, the *blue* and *yellow* sites show increased power levels due to reasons unknown, which possibly could be a measurement artifact. Preliminary analysis of the data collected on Marion Island during the 2016 takeover indicate that the remote sub-Antarctic location is indeed sufficient for avoiding RFI in the frequency band of interest for low frequency experiments. In particular, data collected at the Rooks site show no visible signs of RFI in the FM radio band as hoped. After preliminary analysis of the modest amount of data collected during the 2016 voyage, we outlined our goals for the 2017 voyage.

3.3.2 2017 relief voyage

Following the 2016 engineering run and RFI characterization of Marion, we were confident about installing PRI^{Z}M on the island and operating it for a complete year. With a view to ease the instrument assembly process, I designed new support structures for the antennas which largely comprised of modular units which integrated with each other (as described in Section 2.2.1). The new design was a very effective move towards battling winds up to ∼80–100 knots on Marion. Besides designing the support structures, I also built the first and second stage electronic modules (Sections 2.3 and 2.4) for PRI^{Z}M. After successfully integrating the system, we performed an end-to-end test in the lab. In the month of April 2017, a team of four participated in the relief voyage to Marion.

The primary goals for the 2017 Marion takeover period were to identify a suitable observing location for PRI^{Z}M, install the equipment, verify end-to-end functionality, test survival in the harsh environmental conditions, and ensure sufficient robustness of the system for winter-long operation. The winter operation is supported by the South African Space Agency (SANSA). The over wintering SANSA engineer maintains the experiment on a best effort basis, and is responsible for charging the batteries and backing up observation data. In addition to this, the SANSA engineer is trained by the PRI^{Z}M team to handle low-level system troubleshooting whenever needed.

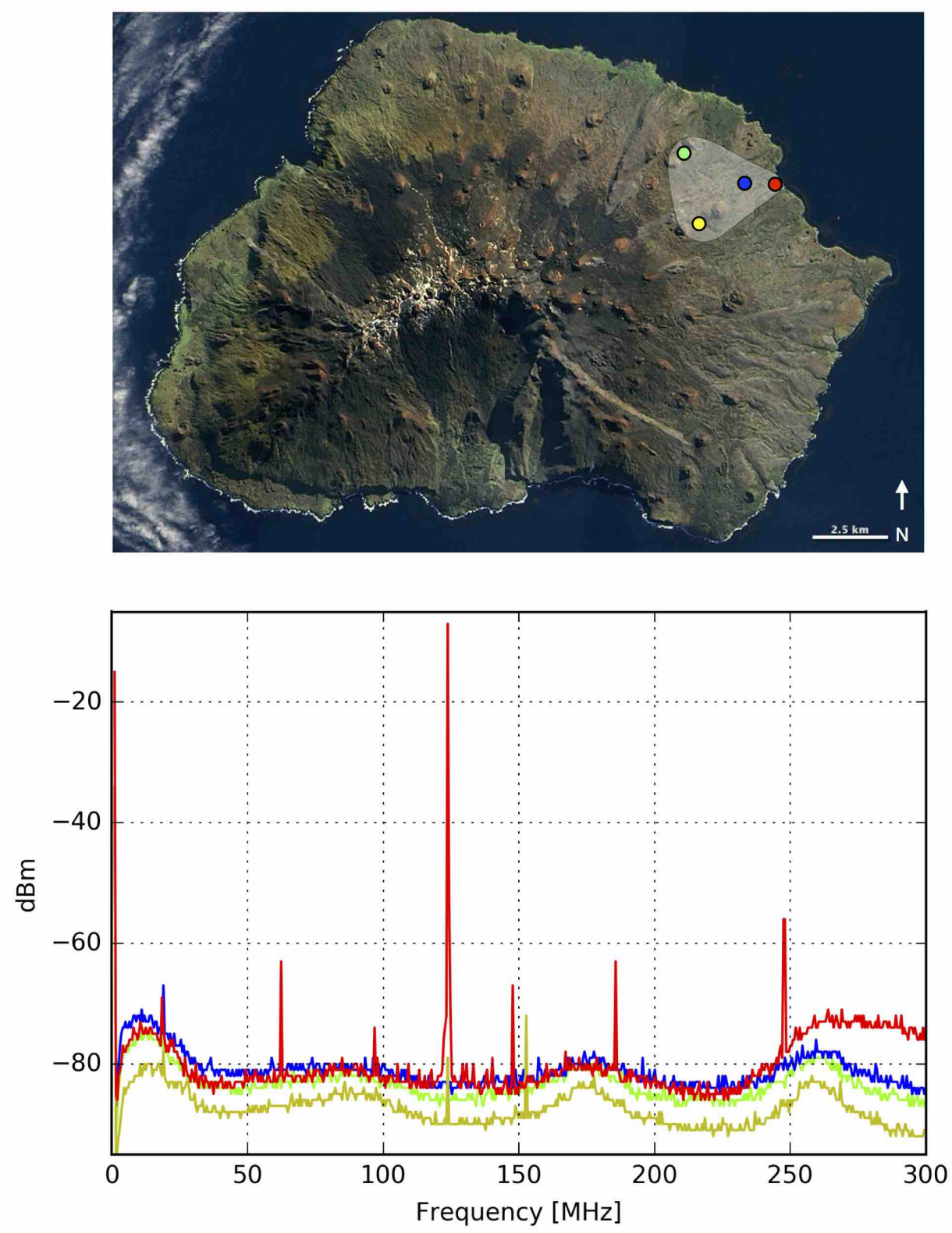

Figure 3.7: The markers on Marion map *(top)* indicate the RFI survey locations during the 2017 voyage. We were searching for a potential observing site within the region highlighted in white that is at a reasonable hiking distance (<5 km) from the base (red marker). The bottom panel shows the spectra recorded (<300 MHz) at each location. The colours in the plot correspond to the marker colours in the map.

3.3.2.1 Site selection

In April 2017 upon arrival at Marion, our immediate aim was to decide upon a suitable observing site for the experiment. The 2016 site, Rooks, was too far from the base to be feasible for regular winter maintenance and operations. Therefore, the observing site for PRI^{Z}M was selected by balancing several requirements: 1. ease of regular access from the main base; 2. sufficient distance from the base to minimize the impact of locally generated RFI; and 3. suitable terrain. During the first several days of the takeover period, we hiked to three different locations within $\sim$5 km from the base (see Figures 3.7 and 3.8), surveyed RFI levels and examined terrain quality. The three locations were :

- Elevated area near the old hydro shack (46°52′11.7”S, 37°50′29.8”E, blue marker in Figure 3.7)
- Between second and third sisters in the Three Sisters mountain range (46°51′57.6”S, 37°48′36.0”E, green marker in Figure 3.7)
- Between Junior’s and Fister’s Kop (46°53′13.0”S, 37°49′10.7”, yellow marker in Figure 3.7)

The elevated area near the old hydro shack was convenient in terms of ease of access, however, we found that the level of RFI shielding from the base was insufficient (refer Figure 3.9). In particular, the 400 MHz DORIS[2] beacon was clearly visible from the hydro shack location, and the level of attenuation was only $\sim$20 dB. The candidate location between the Second and Third Sister provided better shielding than the hydro shack but not as good as the third candidate site; also, the long hiking distance made this site unfeasible. The DORIS beacon too was faintly visible between the sisters. We ultimately selected the third site, between Junior’s and Fister’s kop – it neither had visible contaminations from the base nor was the DORIS beacon visible. Junior’s kop (see Figure 3.10) is the largest hill within a reasonable hiking distance from the main base that can provide enhanced RFI shielding, and we found that the terrain between Junior’s and

[2]https://en.wikipedia.org/wiki/DORIS_(geodesy)

Figure 3.8: The PRI^{Z}M team *(foreground)* and the SANSA team *(background)* RFI surveying a candidate site near 46°52′11.70”S, 37°50′29.80”E (blue marker in Figure 3.7) during the April 2017 takeover.

Hendrik Fister's kop was suitably flat and dry for antenna installation. We chose an installation site roughly 4 km southwest from the main base. The GPS coordinates of our equipment are as follows:

- Three containers, central point: 46°53′13.0”S, 37°49′10.7”E
- 70 MHz antenna: 46°53′13.7”S, 37°49′09.1”E
- 100 MHz antenna: 46°53′14.0”S, 37°49′12.1”

We benchmarked the level of RFI shielding by surveying with a Workman T-601 discone antenna and a Rohde & Schwarz spectrum analyzer. Figure 3.11 shows a comparative plot of RFI at the base and the PRI^{Z}M observing site; these measurements were taken on a day when a helicopter was operating near the base and transmitting at 123.45 MHz. The observed power at 123.45 MHz is suppressed by $\sim$60 dB at the PRI^{Z}M observing site relative to the base, indicating that any station emissions well be similarly attenuated. The power reduction arises from a combination of physical separation from the base and diffraction over Junior's kop.

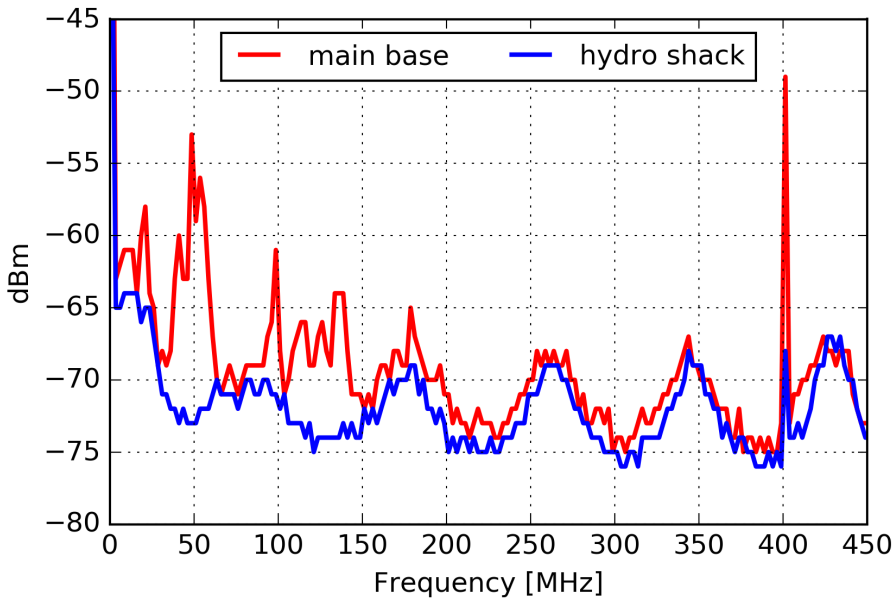

Figure 3.9: RFI spectrum comparison between the main base and one of the candidate sites called the hydro shack. In spite of the hydro shack being easily accessible from the main base, the RFI sheilding was poor especially at lower frequencies. We can clearly see the DORIS beacon (401 MHz) at the main base from the hydro shack. Due to all these factors, the hydro shack was not selected as our deployment site.

3.3.2.2 Instrument installation

Following the selection of the PRI^{Z}M observing location between Junior's and Fister's kop, the next major task was to commence instrument installation. Most activities on Marion is completely weather driven, also the helicopters could sling our shipping containers to the observing site on no/less windy days. After a few days of bad weather, our three containers were finally slung to the site on April 19 (Figure 3.12). The containers were placed end-to-end along the north-south direction, with the open sides facing approximately east so that the container interiors are sheltered from the prevailing winds. We began by surveying and marking our antenna locations relative to the southernmost of the three containers (which we call the command module). We completed the 100 MHz antenna assembly within one day, and installed the backend system and achieved first light on the 100 MHz system on April 21. On April 22,

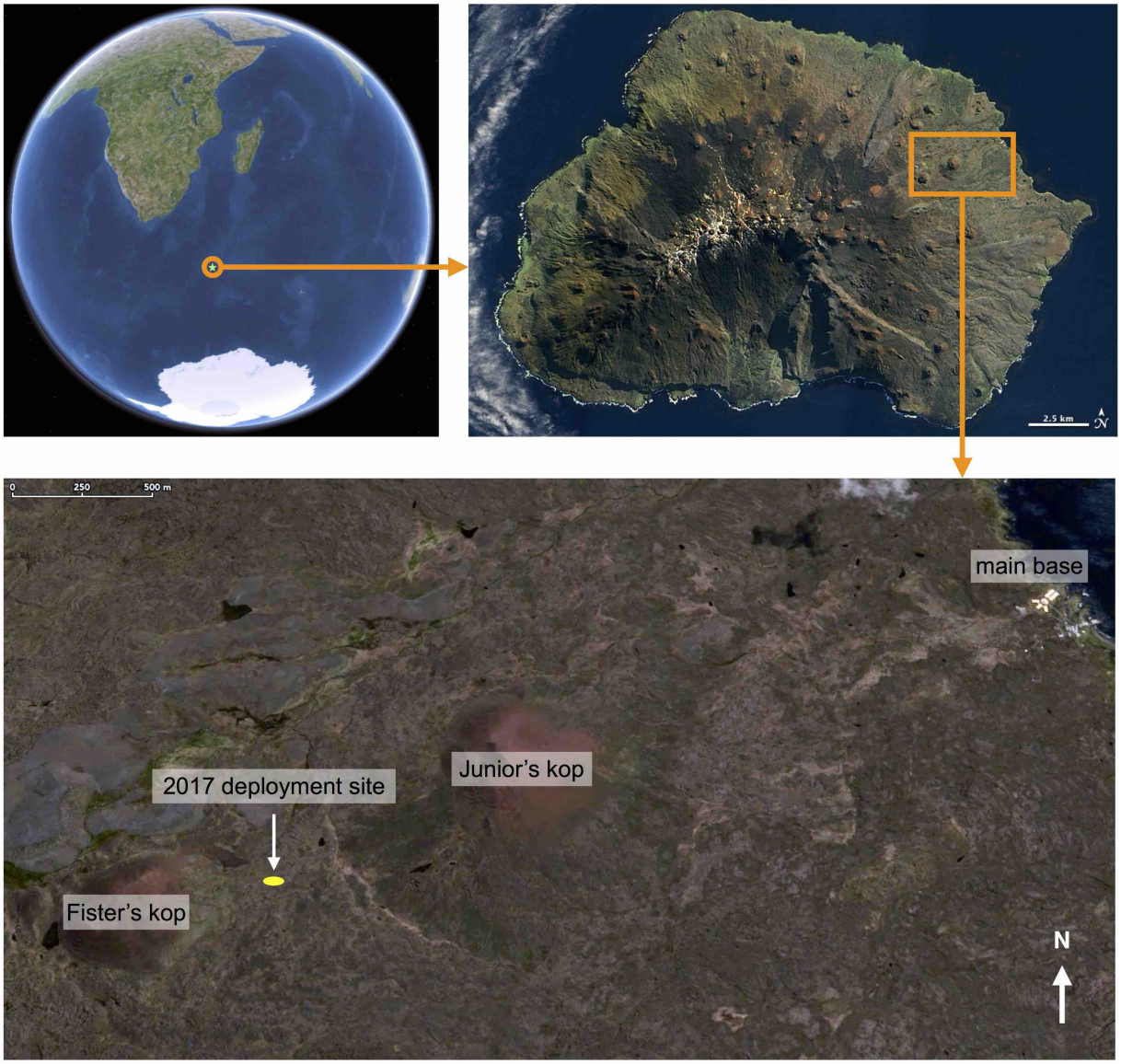

Figure 3.10: Marion Island is located in the sub-Antarctic, roughly halfway between South Africa and Antarctica. The main research base is situated on the northeast side of the island, and the PRI^{Z}M observing site is about 4 km inland, between Junior's and Fister's kop.

we completed the assembly of the 70 MHz antenna and successfully demonstrated end-to-end functionality of the full PRI^{Z}M experiment (Figure 3.13).

Meanwhile, we also employed measures to increase the robustness of the experiment for winter operations. A major concern was weather proofing the instrument; we sealed the central

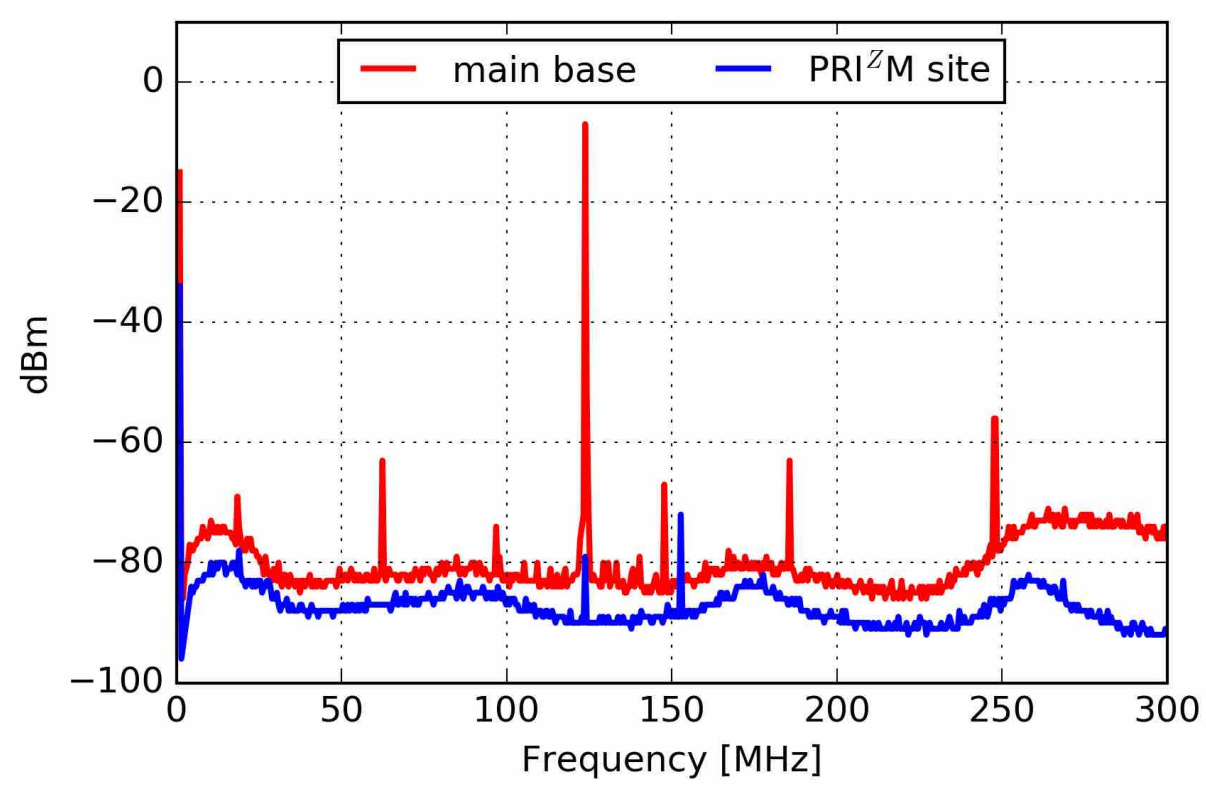

Figure 3.11: RFI spectrum comparison between the main Marion base and the PRI^{Z}M observing location. These spectra are max hold measurements and were taken while a helicopter was operating near the base and transmitting at 123.45 MHz. A comparison of the received power at both locations provides a rough benchmark of ∼60 dB signal suppression, arising from a combination of attenuation from Junior's kop and the distance between the PRI^{Z}M site and the base. The peak at 156 MHz is transmission from a hand held radio.

hub underneath the antennas for water proofing sensitive electronics. Despite the initial success of the PRI^{Z}M setup, we encountered a few days of setback after the equipment was operational. The signal and power cables were attacked by mice, and therefore were covered them with steel mesh sheets to protect them (see Section 3.5 for details). We spent a few days repairing superficial mouse damage and applying several mouseproofing measures. These mouseproofing measures proved effective, and we were back online and observing again by April 27 (refer Section 3.5).

Figure 3.12: *Clockwise from top-left:* On-site cargo drop by the helicopter team; assembling the mechanical support structure; and installing the first stage module.

Our time on the island was limited to ∼3 weeks, and some of the days we were caught in at the base due to gale force winds. Therefore, we only had a limited number of days to access the instrument post its installation (Figure 3.14). All of the days towards the end of the takeover period were devoted to continued observations, calibration measurements, and preparing the hardware and software for winter operations. We collected and backed up the data during all of our visits to the site, and at the end of the relief voyage we returned to the mainland with ∼2 weeks of data from both instruments.

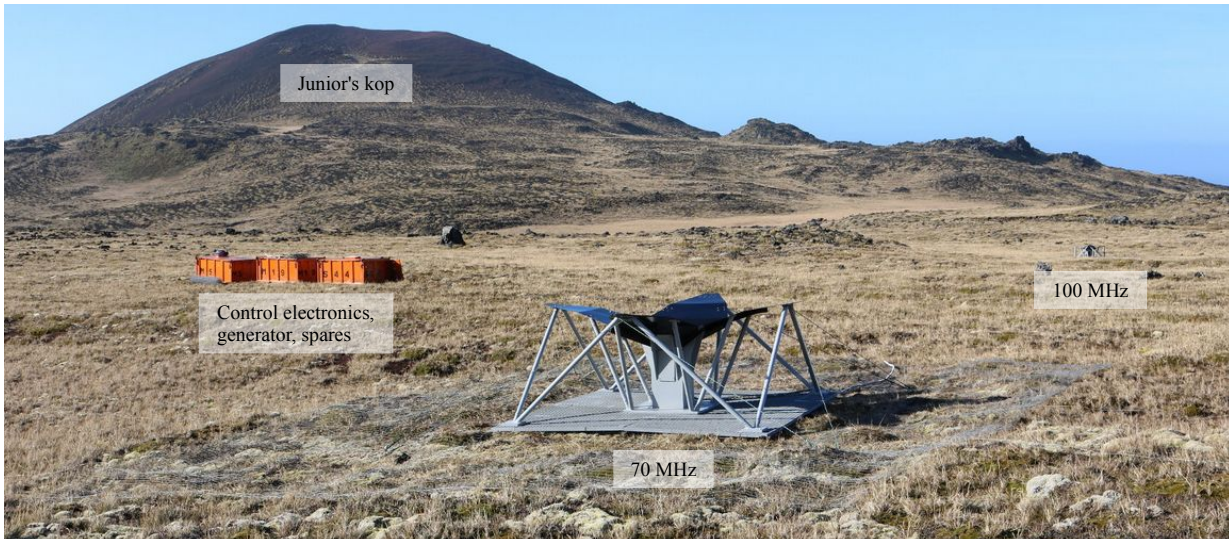

Figure 3.13: The PRI^{Z}M experiment installed on Marion Island. The 70 MHz and 100 MHz antennas are visible in the foreground and background, respectively, and the three orange shipping containers house the control electronics, generator and batteries, fuel cache, and spares. The main base lies 4 km behind Junior's kop.

Figure 3.14: *Left:* Me inspecting the electrical connections of the 70 MHz antenna petals during a snow storm at PRI^{Z}M site. *Right:* Small amount of ice accumulation near the electrical connections at the central hub of the antenna. All electrical contacts and cable feedthrough points are completely sealed from wind, water, ice and mice.

3.3.3 2018 relief voyage

Following our takeover voyage in May 2017, we did not have any access to the PRI^{Z}M hardware until April 2018. The 2017-18 winter operations of PRI^{Z}M were successfully monitored by the SANSA engineer from the M73 team. For the 2018 voyage, we identified the need for improving the existing calibration scheme of PRI^{Z}M, along with refurbishing the electronics and installing two brand new low-frequency antennas to probe the radio sky below 10 MHz. The low-frequency antennas are the first exploratory step toward building a larger array spanning the island, with the aim of imaging the sky at low frequencies that have been unexplored since the 1970s. These observations may allow us to probe even earlier epochs of the Universe's history and will lay the groundwork for eventually exploring the cosmic dark ages. The low frequency experiment we deployed on Marion in April 2018 is discussed in Section 4.4.

In early 2018, we directed our effort towards bringing down the power consumption of the experiment in order to operate the instrument for a longer duration between battery charging times. The four non-latching Teledyne CCR38S360 EM switches that were a part of thePRI^{Z}M FSE during the 2017 deployment, had a relatively higher power draw compared to other components. The reason being that the non-latching switches require a constant supply of power and they draw $\sim$20 W at all times when the system is powered on. Therefore, in 2018 in order to reduce the power draw, we installed four latching Teledyne CCR39S860 EM switches. The latching switches require separate reset and actuation pulses for a maximum of 20 ms, and draws $\sim$21 W each for total of $\sim$2.5 seconds per day. As we notice, even though the latching switches draw more power when switching, they do not require constant supply of power to operate. The change to latching switches reduced the power draw of PRI^{Z}M to $\sim$65 W. The control circuits for both these switch types are discussed in detail in Section 2.7.1.

Another major addition was a broadband noise source for calibration purposes on all signal chains. The noise source was connected on one of the inputs of the calibrator switch. A dedicated GPIO pin on the auxiliary RPi controls the power to the noise source via a mosfet. The schematic of the noise source is illustrated in Figure 3.15, and it outputs a noise temperature of $\sim$3000 K (30–200 MHz) at 12 V (Figure 3.16) as measured in the lab.

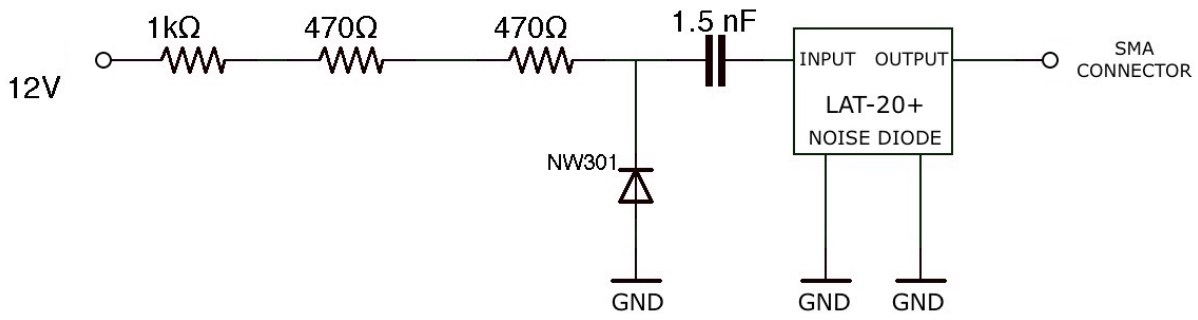

Figure 3.15: Schematic of a broadband noise source added to the input of all calibrator switches in April 2018. The noise source outputs a noise temperature of ∼3300 K (30–200 MHz) at 12 V.

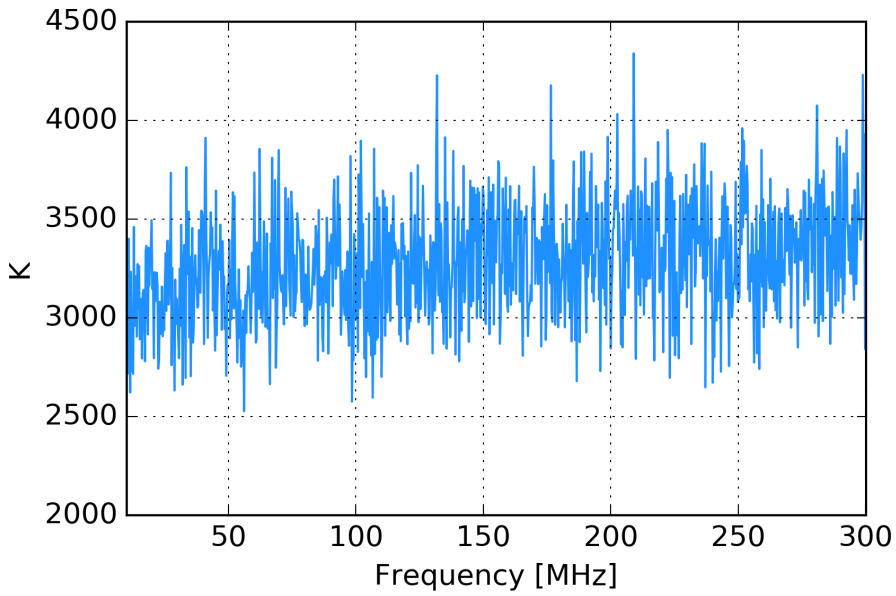

Figure 3.16: The output spectrum of the noise source shown in Figure 3.15. The spectral structure is independent of system contribution.

Because the new switches, noise diodes, and temperature sensors required new control electronics, we also rebuilt the back-end readout system to accommodate an upgraded housekeeping board. Therefore, the FSE and SSE boxes underwent major upgrade in terms of volume expansion and component addition. Newer and better auxiliary circuits were added for improved monitoring of various components in the system. We also added a network switch to facilitate a centralized communication point for all the three RPis inside the second stage Faraday cage. We

additionally reconfigured the internal layout of the back-end system to increase accessibility to critical components. A complete end-to-end testing (as shown in Figure 3.17) was performed at the main base prior to field installation.

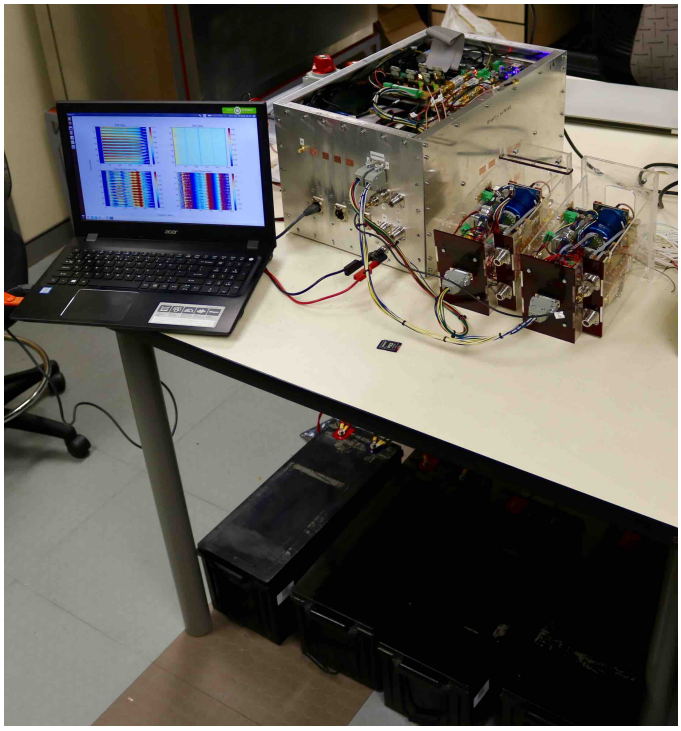

Figure 3.17: The newly upgraded PRI^{Z}M system undergoing an end-to-end test at Marion base in April 2018. The SSE box is connected to two FSE boxes, and test data is being displayed on the laptop. The system is powered using 4 lead cyrstal batteries of 200 mAh each placed under the table.

3.4 Operations and onsite infrastructure

During the takeover voyage, we only get ∼3 weeks at Marion Island (see Section 3.2). Weather delays and logistical challenges further cut short our time on the island. The observing site is ∼4 km from the main base on Marion Island. The onsite operations are completely driven by two factors – weather and daylight. The site is completely inaccessible on days with gale force winds, blizzard etc. Limited daylight plays another major role in restricting our access

to the instrument. A normal day at the Marion base begins with a 6 am breakfast, followed by gearing up for onsite activities, and finally commencing the trek at 8 am. It takes about a hour to walk to the PRI^{Z}M site. The route to the site is littered with lava rocks and hidden mires, thus, making the trek significantly challenging.

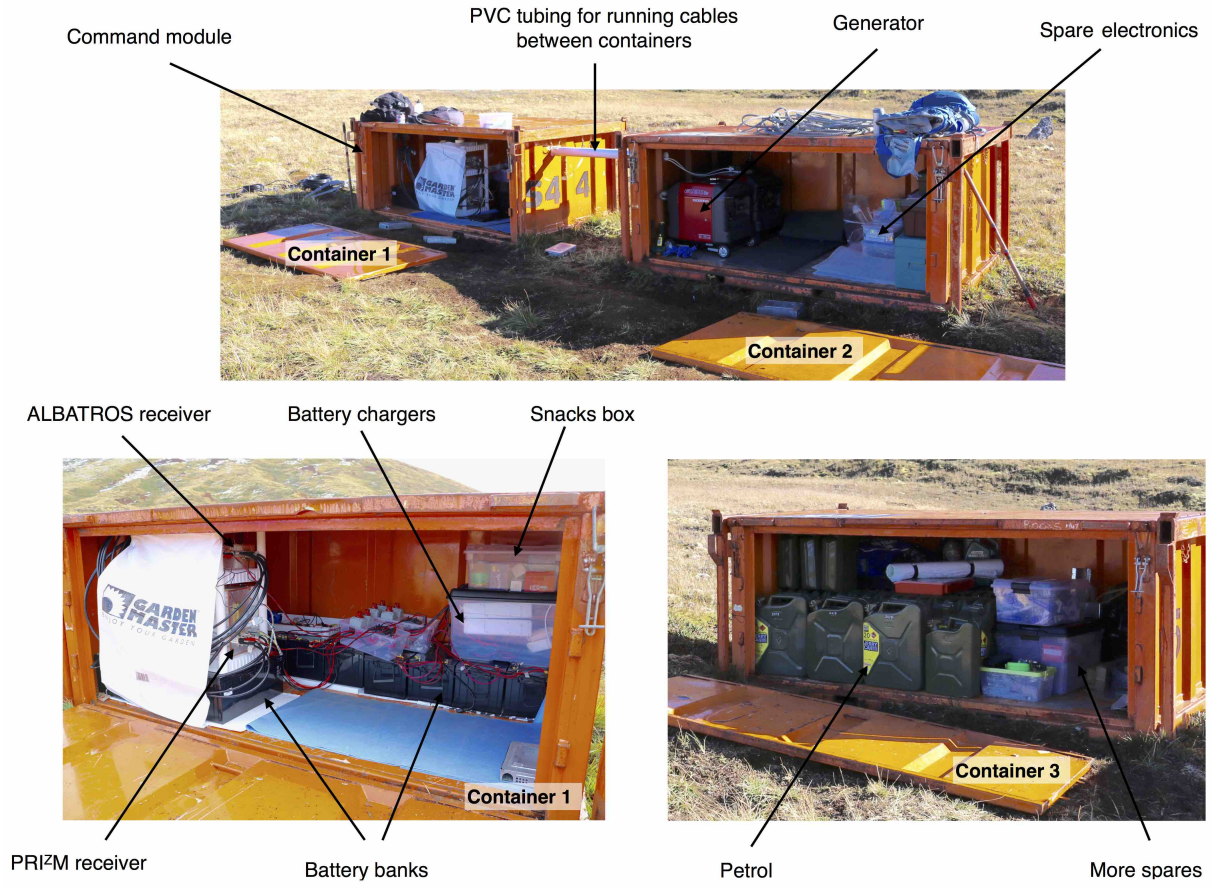

Figure 3.18: There are three shipping containers at the PRI^{Z}M site. The command module contains newly rebuilt readout electronics for both the PRI^{Z}M and ALBATROS (described in Section 4.4) experiments, with battery banks, and chargers etc. The generator and fuel containers are the two other containers at site.

The PRI^{Z}M instrument is installed behind the Junior's hill (details in Section 3.3.2.1), and we have three shipping containers at site for storage and backend support (see Figure 3.18). The containers are placed end-to-end along the north-south direction, with the open sides facing approximately east so that the container interiors are sheltered from the prevailing winds. Two

out of three containers are connected together by a section of PVC tubing to run cables from the generator to the batteries, this makes the charging process easier. 50-m cable bundles (two LMR-400 coaxial cables for the antenna signals, plus a 15-conductor Jaycor cable for power distribution) run from the antennas to the southernmost "command module" container, which lies near the midpoint of the two antennas and houses the backend electronics. The command module also houses eight lead crystal batteries that power the system, as well as the battery chargers. The central container houses the generators and spare electronics. We use petrol to operate the generator, and the fuel cache is stored in the northernmost container.

The onsite operations include data copying and backup, battery charging, generator refueling etc. We also perform regular hardware inspection to keep a check on the robustness of the instrument. We dedicate a significant amount of time for preparing the hardware and software for winter operations.

3.5 Mice extermination program

Figure 3.19: Mice eating away our cable insulation *(left)* and self amalgamating tape *(right)*.

House mice have been present on Marion Island for over 200 years. After an attempt to eradicate the mice by introducing cats failed, the mouse population exploded. Currently, mice pose a significant threat to the birds on Marion, thereby classifying Marion as a priority island

for mouse eradication. The havoc caused by mice extended into the electronics domain in April 2017 as they attempted to chew on our coaxial cable sealant, self-amalgamating tape, electrical tape, wire insulation, etc. On numerous occasions our cable insulations were under attack by the vermins (see Figure 3.19). We soon understood the affinity of mice towards plastic insulation and adhesives. We spent a few days repairing superficial mouse damage and applying several mouseproofing measures, which included wrapping cables in wire mesh cloth (see Figure 3.20), stuffing cable penetrations with metal scouring pad material, and selective use of silicone sealant.

Figure 3.20: The PRI^{Z}M cables are protected by wrapping them with finely woven steel mesh *(left)*. A combination of steel mesh and scourer pads are used to prevent mice from entering the cable feeding pointing at the base of the antenna *(right)*.

During the 2018 relief voyage, a team of mouse eradication experts collected data by baiting specific areas on Marion. A complete eradication of mice from Marion is, however, a major focus area for the DEA during upcoming deployments.

3.6 Advantages of observing from Marion Island

As mentioned briefly in Section 3.1, for experiments such as PRI^{Z}M, there lies a major threat from time-invariant broadband RFI that dominate regions in the observed spectrum. For example, interference from FM radio lies in a frequency range of ∼88–105 MHz and extends

hundreds of kilometers from the source stations, presenting a serious challenge for low-frequency observations. Therefore, experiments are deployed to some of the most remote locations on Earth, and some instruments are proposed to be space-based.

The remoteness of Marion Island makes it a truly unique location to carry out ground based very low-frequency radio astronomy. The radio-quietness of our observing site is evident in our data (see Chapter 4), with no detectable interference in the FM band, which otherwise is a major concern for most remote observing sites around the world. Moreover, PRI^{Z}M deployment has opened the door to one of the most excellent low frequency radio astronomy sites on Earth.

3.6.1 Ionosphere

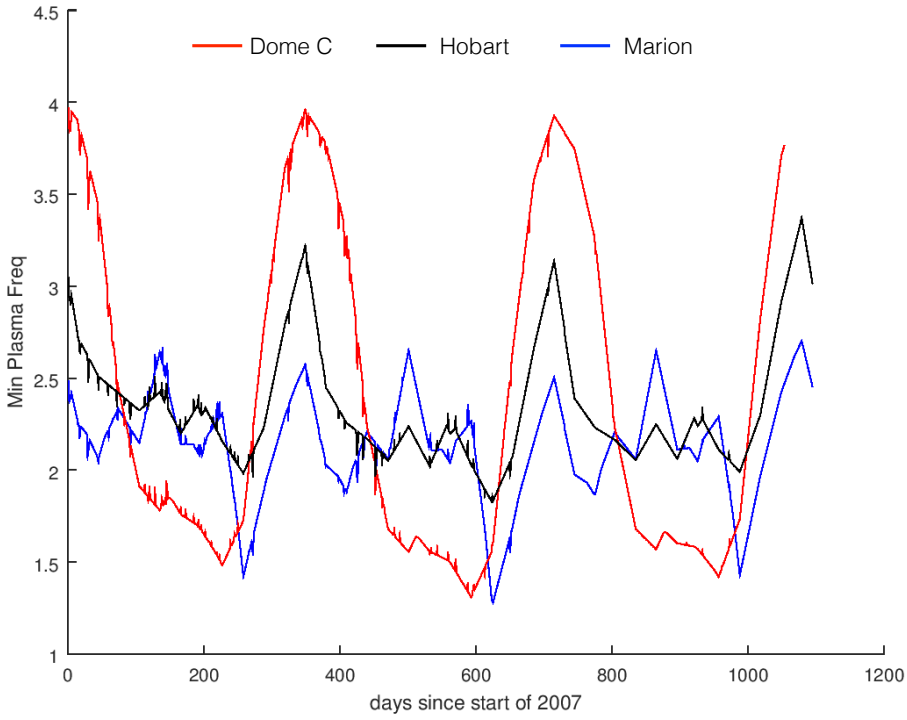

Figure 3.21: The daily mean of the plasma frequency at different locations in the Southern hemisphere during the last solar minimum as predicted by the International Reference Ionosphere model (IRI-2007).

Adding to the contamination by terrestrial RFI, the ionosphere also attenuates the cosmo-

logical signal. The ionosphere is a layer in the Earth's upper atmosphere that extends to a height of about 50 to 1000 km. In this layer, the incoming solar radiation and high energy particles ionize the air molecules, thereby creating plasma. At low frequencies, the ionosphere reflects radio waves, with the cutoff frequency set by the plasma density of the ionosphere. This phenomenon is well known in radio communications and is why low-frequency transmissions (like AM radio) can sometimes be picked up from thousands of kilometers away. The cutoff frequency drops at low ionization levels, such as at night and during periods of low solar activity. The minimum frequency transmitted to Earth, and therefore the lowest frequency at which we can observe, is set by the plasma frequency in the ionosphere. The International Reference Ionosphere model (IRI-2007) predicted plasma frequency as low as $\sim$1.5 MHz at Marion Island (Figure 3.21) during the last solar minimum. The minimum plasma frequency from Marion is comparable to polar sites, such as Dome C, and most locations elsewhere on Earth have minimum plasma frequencies higher than that from Marion. In low frequency measurements, it is important to characterize the state of the ionosphere during observation. This is done by measuring the variability in the total electron content (TEC).

Marion Island, therefore, benefits from its high latitude, with long winter nights giving ions more time to recombine, and not being near the magnetic poles leading to less auroral ionization. This opens a unique window into $<$10 MHz observations. Low frequency experiments that were once thought possible only from space, might be able to make quality measurements from Marion during the austral winter. Such observations could provide high resolution improved measurements over previous results at $<$10 MHz frequencies. The groundwork of exploring lower frequencies has been laid with the installation of newer antennas at the PRI^{Z}M site (see Figure 4.15). By observing at lower frequencies, we may be able to use the 21 cm hydrogen line to understand the synchrotron self-absorption of the Milky Way, and even push to higher redshifts such as of the dark ages in the Universe.

3.6.2 Meteor scatter

Meteoroids enter the Earth's atmosphere at a speed of ∼10–75 km/s, and collision with the atmosphere results in ionization of the air molecules. The ionized trail acts as a mirror that reflects radio waves, and can last anywhere from a few hundredth of a second to a few seconds. During this time, brief communication paths can be established between radio stations several thousand miles away from each other by bouncing radio waves off the ionized trail. Similarly, terrestrial RFI too gets scattered off the trail over long distances. The magnitude of RFI due to meteor scatter varies depending upon the location of the meteor trail and the rate of meteor activity. Therefore, suggesting increased scattering during meteor showers. The ∼2000 km separation between the island and the mainland is close to the distance limit at which meteor trails effectively scatter RFI (Wislez, 1996). We have not seen qualitative evidence of enhanced RFI from meteor scattering, an effect that is commonly visible at many other remote sites.

CHAPTER 4

Preliminary data and future outlook

4.1 PRI^{Z}M raw spectrum

The spectrometer samples the input analogue signal, channelizes and integrates for ∼4 seconds to generate a spectrum. The raw spectrum from the SNAP represents linear power, and we plot the spectrum in dB. Figure 4.1 shows a single raw spectrum from the 100 MHz system without any cuts or processing. The spectrum covers the frequency range 0–250 MHz, with 4096 channels, corresponding to a frequency resolution of 61 KHz. High and low pass filters in the second stage cut off the signal below 30 MHz and above 200 MHz. The lone spike at ∼136–139 MHz is from an Orbcomm satellite. Very rarely, during the relief voyage, we see temporal spikes between 150–160 MHz from the hand-held radios used by fellow researchers on Marion, and from the ship's transponder at ∼162 MHz. However, these radio communications happen only during the takeover period, the band is otherwise quieter for the rest of the year. The spike at 125 MHz comes from the FPGA clock, which also produces harmonics across the band spaced by 31.25 MHz.

The noise power spectra of the 50 Ω and 100 Ω resistors have similar amplitudes N_p be-

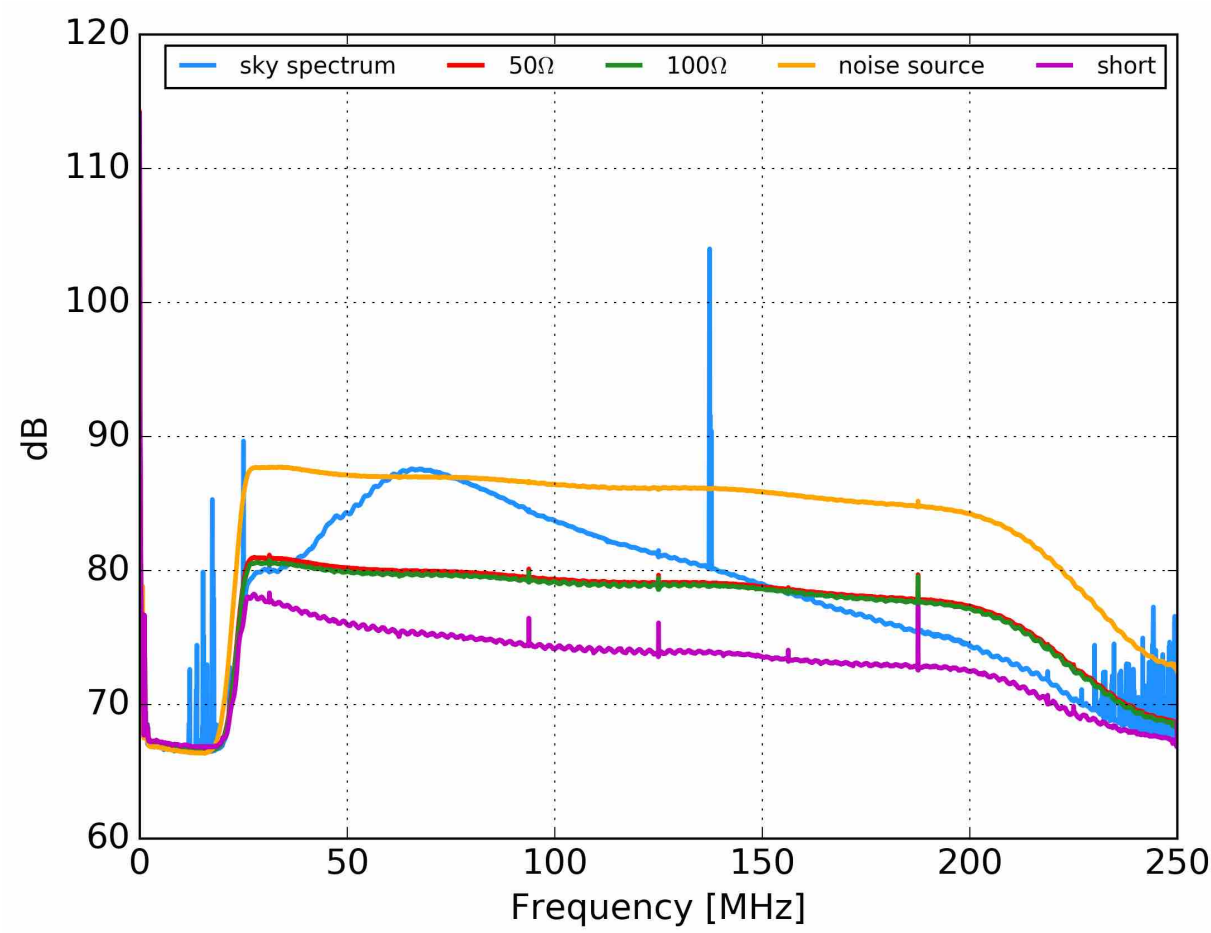

Figure 4.1: Spectra of raw data from a single dataset (∼4 second integration) from the PRI^{Z}M 100 MHz East-West polarization. The different spectra denote antenna and calibrator observations.

cause they are at the same physical temperature T. The nominal relationship $N_p = kTB$ is independent of resistance and depends only on the bandwidth B and Boltzmann's constant k. This equation assumes a perfect match between the emitting resistor and the LNA; we use the two different resistors to quantify any mismatch and to separate voltage and current noise in the LNA model.

The antenna and calibrator sources spectra show ∼2.5 MHz ripples across the observed frequency band. Figure 4.2 shows a truncated version of the short spectrum in which the ripple frequency (∼2.5 MHz) can be easily measured. Given the RF propagation velocity in LMR400

is 0.84c, we get a signal propagation length of $(0.84 \times 3 \times 10^8)/(2.5 \times 10^6) \approx 100$ m, caused by an end to end reflection in the 50 m coaxial transmission line, possibly due to impedance mismatch at the end connectors.

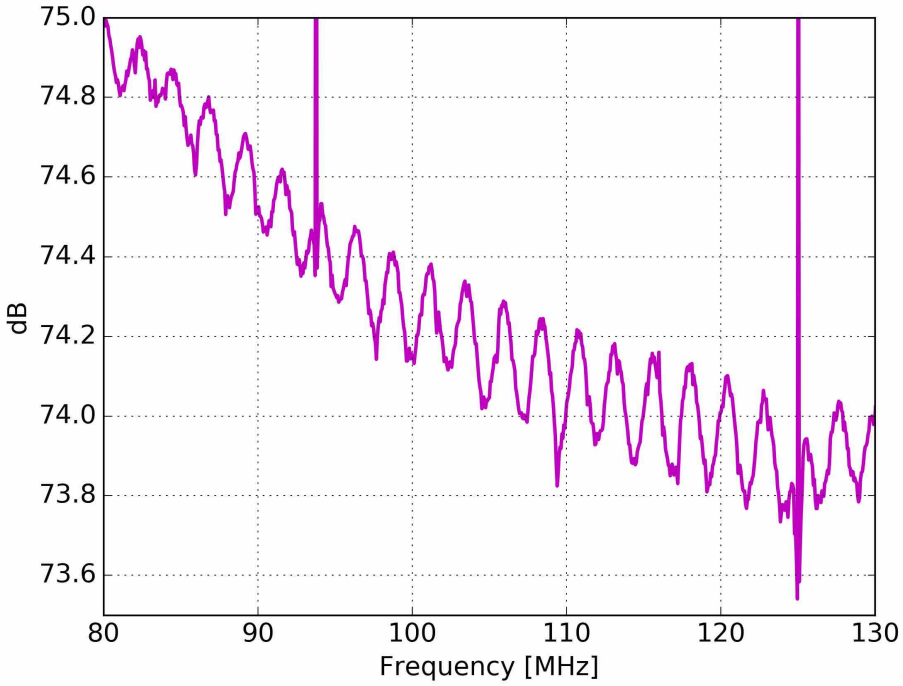

Figure 4.2: A representative truncated short spectrum showing ∼2.5 MHz ripple across the band. This ripple, present in antenna and calibrator spectra, is caused by standing waves in the 50 m LMR400 coaxial cable. The spike at 125 MHz is believed to be due to leakage from the FPGA clock, and its harmonic at 93.75 MHz.

Figures 4.3 and 4.4 show representative 24 hour raw spectra recorded by the 100 and 70 MHz systems on April 24–25, 2018. In this image, the switch cadence was set to 1 hour on the sky and 1 minute on each of the calibrator sources, resulting in a comb of narrow horizontal streaks in time. However, the switching cadence was changed to 15 minutes on the sky and 1 minute on each of the calibrators, halfway through the takeover voyage. During the 2018 takeover voyage, the 70 MHz North-South polarization chain showed qualitatively different frequency structure (therefore not shown in Figure 4.3) than the rest, and the malfunction was traced to the FSE box. As mentioned previously, the biggest challenge on Marion is working with the

continuously shrinking time frame, and therefore we could not debug the 70 MHz North-South polarization during the 2018 takeover. This task has been assigned the highest priority for the upcoming takeover voyage.

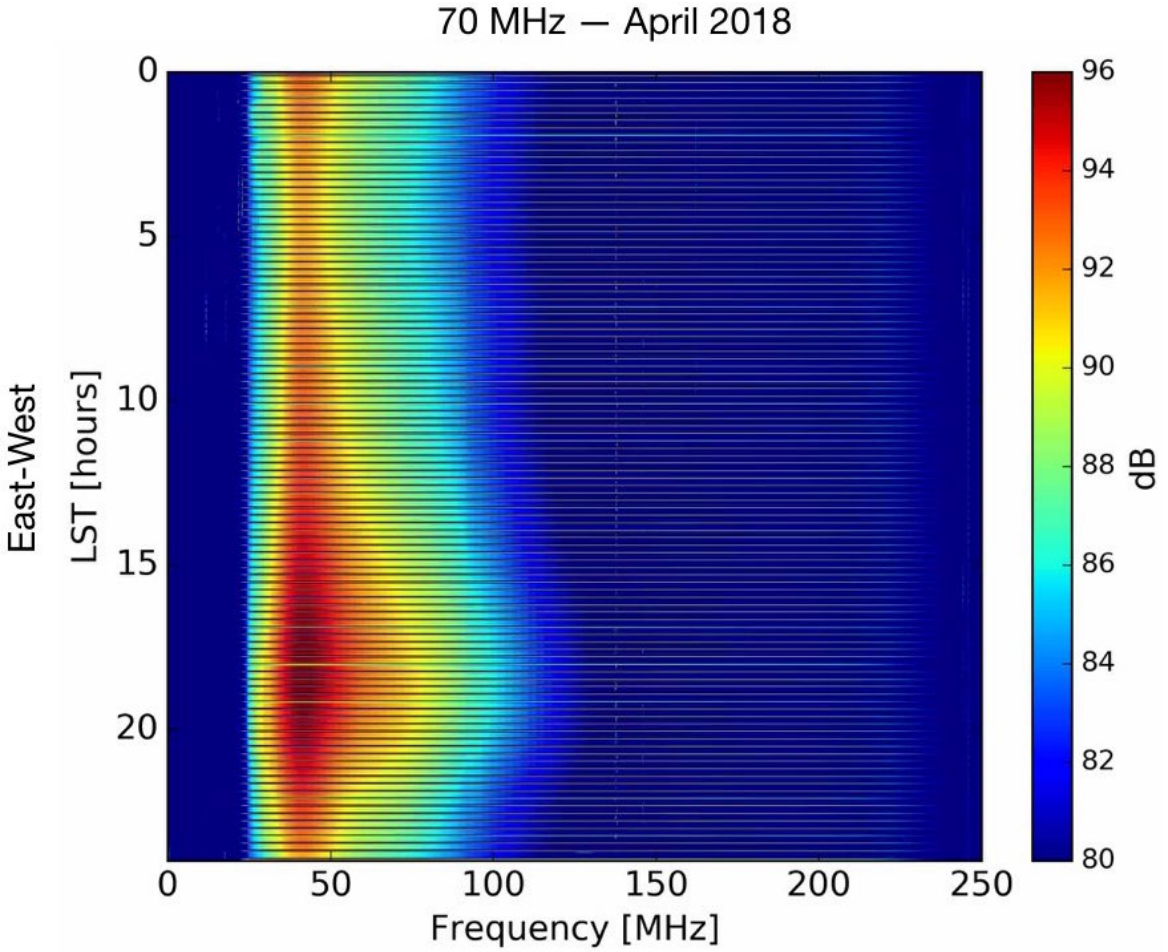

Figure 4.3: 24 hour waterfall plot of raw data from East-West polarization of the 70 MHz system recorded in April 2018. The fine horizontal streaks are due to switching between on-sky and calibrator observations. The switching cadence is one hour on the sky and one minute on each of the calibrator sources. During the April 2018 takeover voyage, the North-South polarization signal chain had a malfunction, and therefore not shown in this plot.

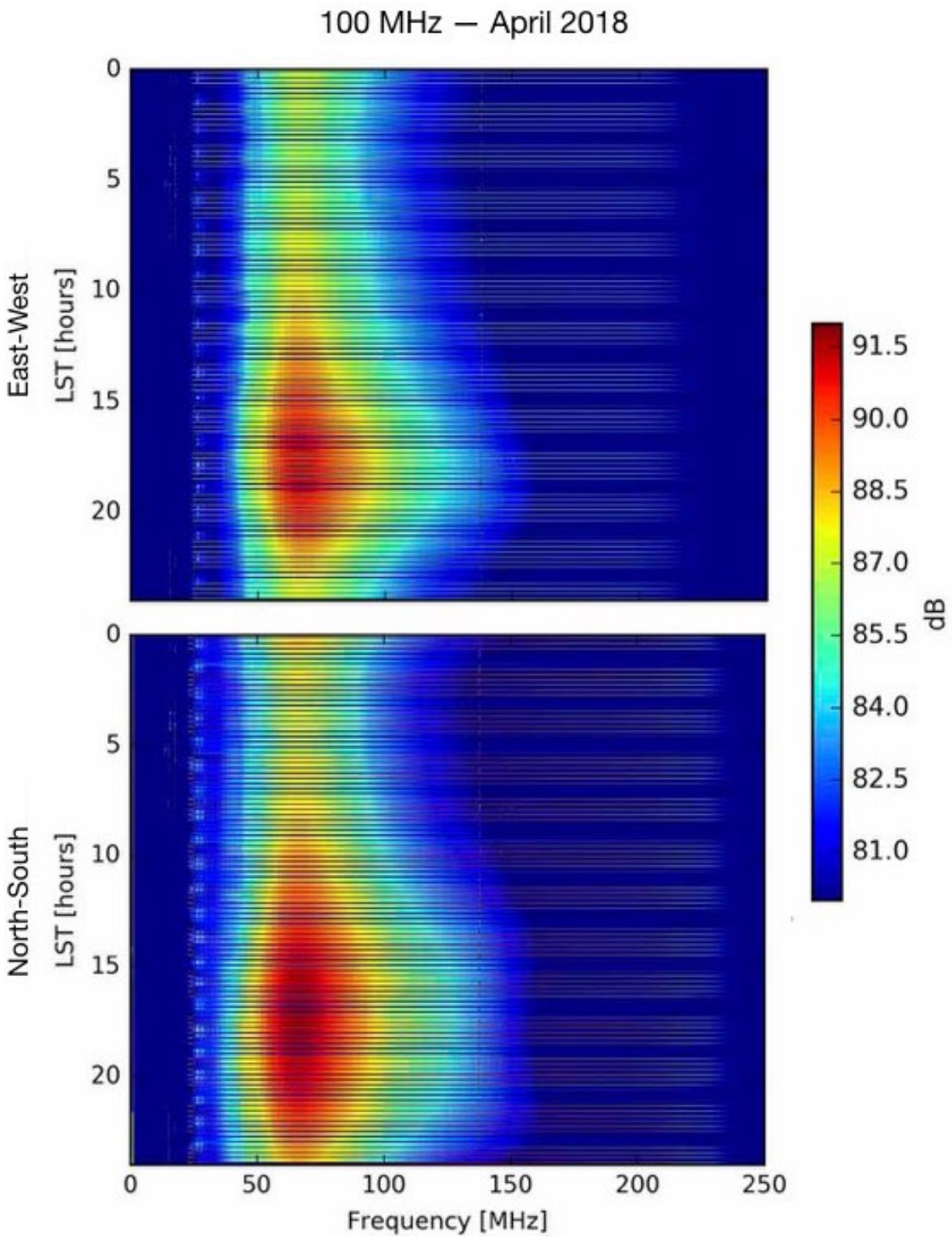

Figure 4.4: 24 hour waterfall plot of raw data from East-West polarization *(top)* and North-South polarization *(bottom)* of the 100 MHz system recorded in April 2018. The fine horizontal streaks are due to switching between on-sky and calibrator observations. The switching cadence is one hour on the sky and one minute on each of the calibrator sources.

The raw data are separated into antenna and calibrator sources dataset for qualitative analysis and calibration. A 24 hour waterfall plot of antenna raw datasets from both systems is shown in Figure 4.5. We further band limit the data by selecting an appropriate range of frequency channels based on the effective working range of both antennas, which is 40–85 MHz for the 70 MHz antenna, and 65–130 MHz for the 100 MHz antenna. These frequency ranges exclude RFI such as Orbcomm transmission and the filter roll-off structures at the edge of the band.

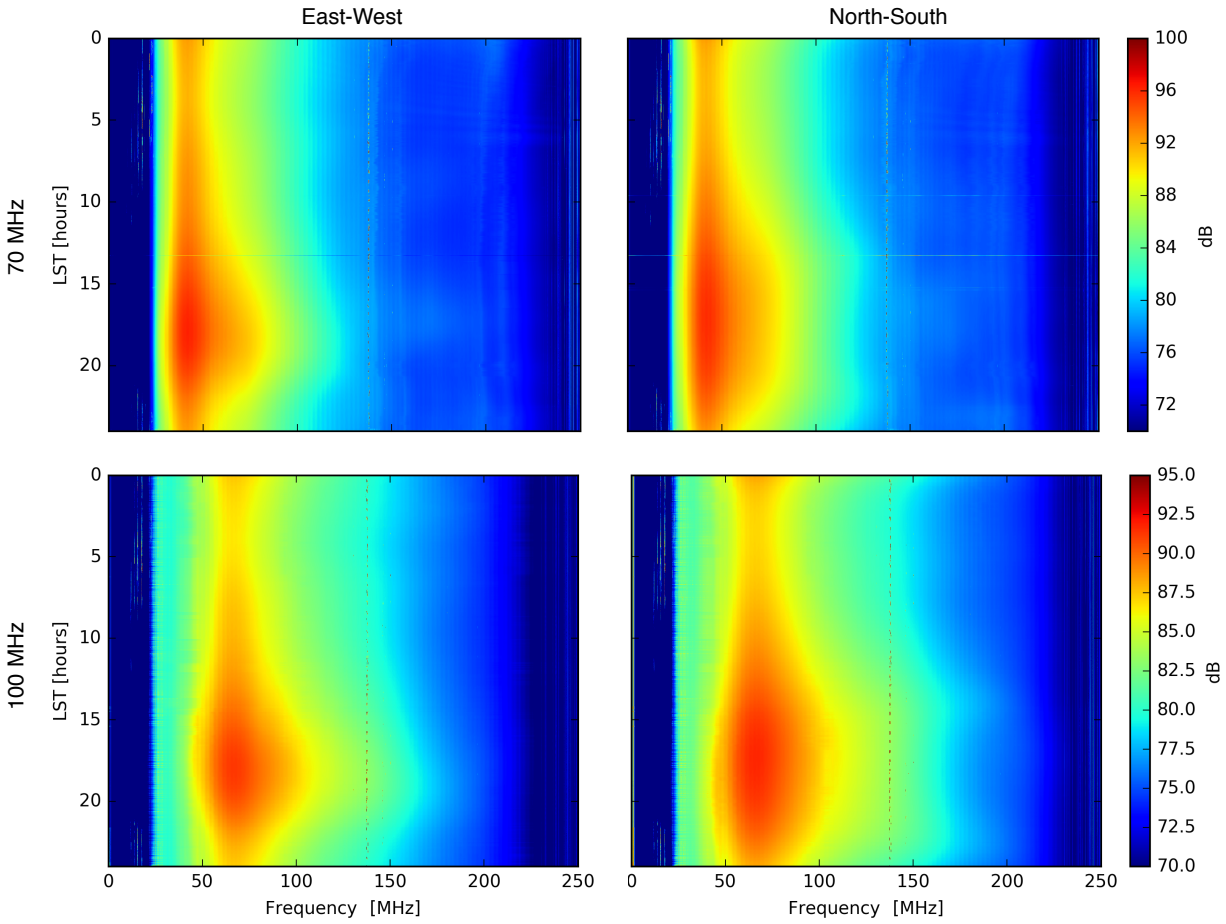

Figure 4.5: 24 hours of waterfall plots from the 70 MHz antenna recorded in April 2017, and the 100 MHz antenna recorded in April 2018, on Marion Island. This plot shows the raw data without any calibration or RFI mitigation.

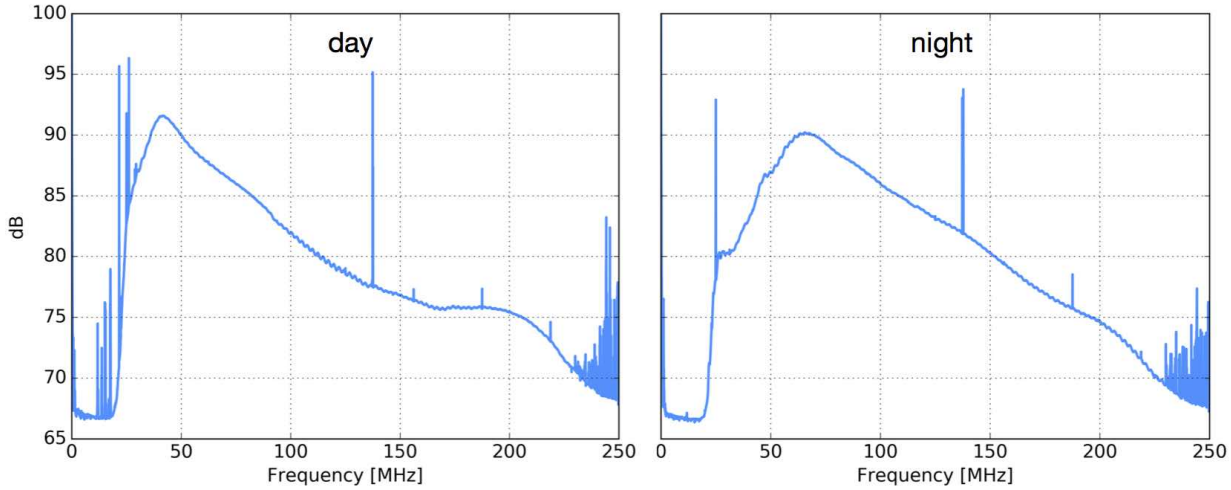

Figure 4.6: Representative spectra from the 70 MHz system showing day and night variation in the reflection of long wavelength transmission (<30 MHz, eg. AM radio). During daytime, when the solar activity is high, the ionosphere reflects radio waves (spikes <30 MHz in the left panel). However, during night, the reflection is significantly reduced because ions recombine and are not replenished due to photoionization.

In terms of RFI, the FM band (88–110 MHz) looks visually clean, also we do not notice any temporally varying RFI emission. The shortwave radio signals reflecting off the ionosphere during the daytime can be seen at <30 MHz, and the reflections reduce significantly during the night when the ionosphere becomes calmer. This phenomenon is seen in Figure 4.6, which shows two spectra – the day spectrum was recorded at noon on April 24, 2018, and the night spectrum at midnight on April 25, 2018. During the winter nights, the ionosphere has a lower plasma frequency.

In this chapter, I will describe the preliminary analysis of data from the 2018 takeover period. The data analysis is still in progress, and therefore the analysis included in this dissertation is not complete and should not be taken as the final outcome.

4.2 Preliminary bandpass calibration

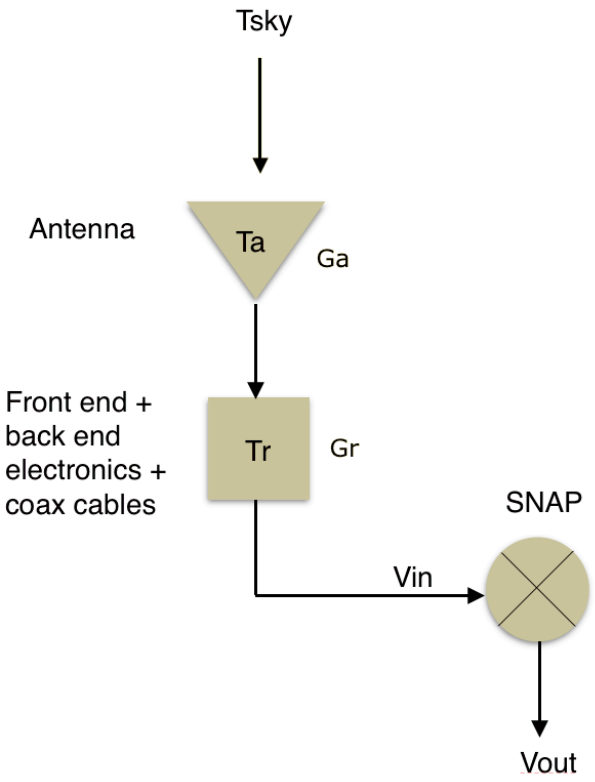

Figure 4.7: PRI^{Z}M signal chain for a single polarization with antenna as the input. T_a and T_r are antenna and receiver temperatures respectively. The gains of the antenna and receiver are denoted by G_a and G_r respectively. V_{in} and V_{out} are the input and output voltages of the spectrometer.

During the 2017 and 2018 takeover voyages, due to on site challenges, we could not dedicate time to perform calibration specific measurements on the system. However, we attempt a preliminary formalization of calibration equations for PRI^{Z}M to understand the quality of our measurement. Due to lack of adequate measurements needed for efficiently calibrating the system, we are currently unable to provide fully calibrated analysis. The parameters used in this section are conservative and more stringent analysis techniques will be implemented in the future.

Figure 4.7 is a simplified block diagram of a single polarization signal chain of PRI^{Z}M.

The antenna and receiver has their individual gains G_a and G_r respectively. These gains induce corresponding noise temperatures in them. In theory, the antenna could be replaced with a resistor and the temperature of the resistor can be varied until the noise power it produces matches the noise power from the sky. When the noise power levels match, the temperature of the resistor can be called the antenna temperature (T_a).

During an observation, a voltage V_{sky} is induced across a PRI^{Z}M dipole measuring the sky temperature T_{sky}. Therefore, the voltage V_a measured across a single antenna dipole (for a single polarization) can be written as,

$$V_a = V_{sky}(1 + \Gamma_a)G_a \tag{4.1}$$

where Γ_a is the return loss of the antenna.

In the case of a hypothetical noiseless receiver, we can describe the input voltage to the spectrometer (V_{in}) as,

$$V_{in} = G_r V_a \tag{4.2}$$

Ideally, the frequency dependent output power of the spectrometer for on-sky observation can be calculated as,

$$\begin{aligned} P_{out}^{sky} &= V_{in}(\nu)V_{in}^{*}(\nu) \\ &= |V_{in}|^2 \end{aligned} \tag{4.3}$$

Using Eqn. 4.2 and the relation $T_{sky} = |V_{sky}|^2$, we can define the above equation as,

$$\begin{aligned} P_{out}^{sky} &= |G_r\ V_a|^2 \\ &= |G_r\ (V_{sky}\ (1 + \Gamma_a))\ G_a|^2 \\ &= |V_{sky}|^2\ |G_r\ (1 + \Gamma_a)\ G_a|^2 \\ &= T_{sky}\ |G_r|^2\ |G_a|^2\ |(1 + \Gamma_a)|^2 \end{aligned} \tag{4.4}$$

Taking into account the receiver noise T_r, Eqn. 4.4 becomes,

$$P_{out}^{sky} = T_{sky}\,|G_r|^2\,|G_a|^2\,|(1+\Gamma_a)|^2 + T_r\,|G_r|^2 \tag{4.5}$$

Now, for a reference load of 50 Ω with V_{50} as the corresponding voltage, we can write the input voltage to the spectrometer (V_{in}) as,

$$V_{in} = G_r\,V_{50} \tag{4.6}$$

The corresponding output power therefore becomes,

$$\begin{aligned} P_{out}^{50\Omega} &= V_{in}(\nu)V_{in}^*(\nu) \\ &= |G_r\,V_{50}|^2 \\ &= |V_{50}|^2\,|G_r|^2 \\ &= T_{50}\,|G_r|^2 \end{aligned} \tag{4.7}$$

In all our assumptions, we have considered a hypothetical case of all reflections in the system to be zero. Therefore, we can express the output power of a short load as,

$$P_{out}^{short} = T_r\,|G_x|^2 \tag{4.8}$$

Using Eqns. 4.5, 4.7 and 4.8,

$$P_{out}^{sky} - P_{out}^{short} = T_{sky}\,\cancel{|G_x|^2}\,|G_a|^2\,|(1+\Gamma_a)|^2 + \cancel{T_r}\,\cancel{|G_x|^2} - \cancel{T_r}\,\cancel{|G_x|^2} \tag{4.9}$$

$$\frac{P_{out}^{sky} - P_{out}^{short}}{P_{out}^{50\Omega}} = \frac{T_{sky}}{T_{50}}\,|G_a|^2\,|(1+\Gamma_a)|^2 \tag{4.10}$$

Eqn. 4.10, however, computed with conservative parameters shows that our semi-calibrated result is independent of the temperature of the receiver. We implemented Eqn. 4.10 on a ∼20 min dataset from the East-West polarization of 100 MHz system, and obtained a semi-calibrated spectrum. The ripples in this spectrum were fitted using a 5^{th} order polynomial as follows,

$$P'_{dB} = \sum_{i=0}^{5} a_i\nu^i + \sum_{i=0}^{5} b_i\nu^i\Big(c\sin(k\nu) + d\cos(k\nu)\Big) \tag{4.11}$$

where a, b, c, d and k are constants, and the resultant spectrum is shown in Figure 4.8.

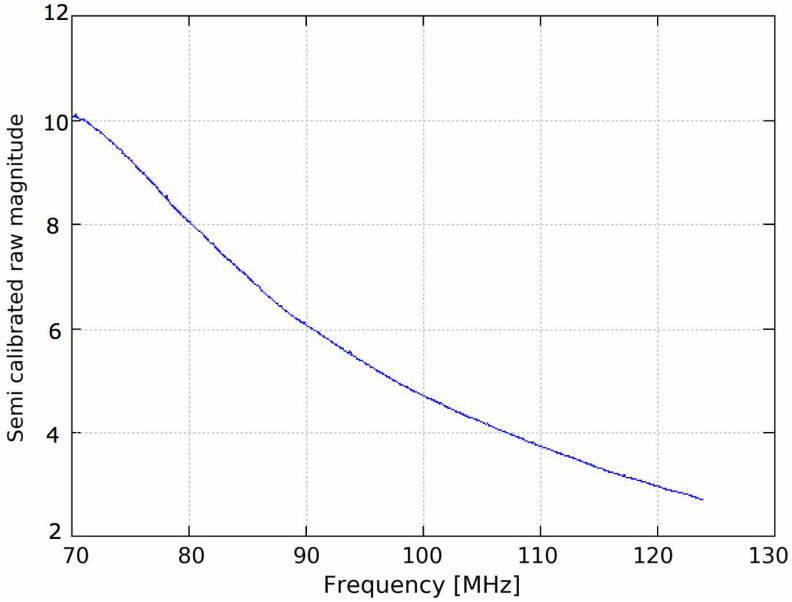

Figure 4.8: A representative plot showing ∼20 min dataset from the East-West polarization of 100 MHz system that is partially calibrated using Eqn. 4.10.

We calculated the residuals from Figure 4.8 using,

$$\text{residual} = \left(P_{dB} - \sum_{i=0}^{5} b_i \nu^i \Big(c \sin(k\nu) + d \cos(k\nu) \Big) \right) \Big/ \sum_{i=0}^{5} a_i \nu^i \tag{4.12}$$

The residual RMS is roughly at the ∼0.5% level (see Figure 4.9). With an order-of-magnitude sky temperature of 1000 K, a ∼0.5% signal residual corresponds to ∼5 K. In order to reach a residual level required to confirm the EDGES detection (Bowman et al., 2018), we need to improve our measurements by a factor of ∼10. Analyzing more data and adopting a better calibration approach will help us achieve improved results. The preliminary results provide necessary checkpoints for ongoing analysis. Our team is currently working on the 2017-18 season data that we retrieved during the April 2018 voyage, and results will be published in the future.

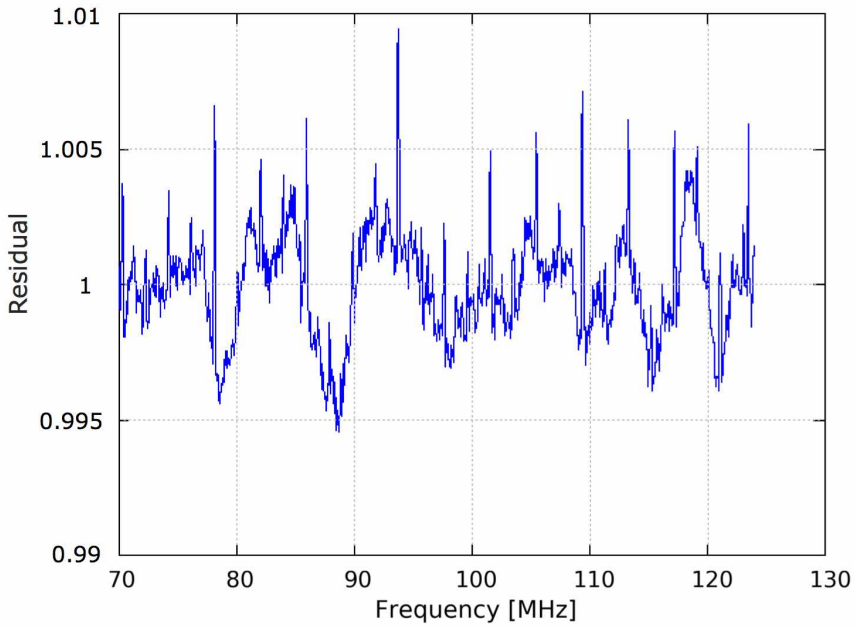

Figure 4.9: The residuals after removing the ripples and diving by a background smooth polynomial. The plot suggests a $\sim$0.5% residual, thus placing PRI^{Z}M within a factor of $\sim$10 from the EDGES detection. The plot is generated using a semi-calibrated 20 minute dataset, hence, with more data and improved calibration, we should be able to provide better results.

4.3 Foreground modeling

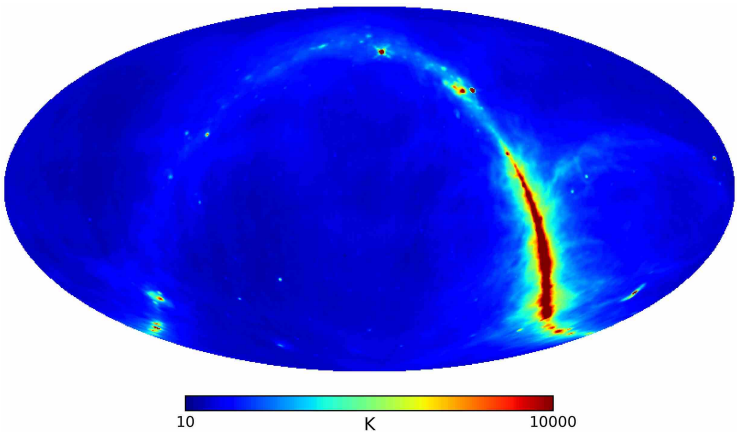

Figure 4.10: A global sky model by de Oliveira-Costa et al. (2008) at 100 MHz plotted in the celestial coordinate system.

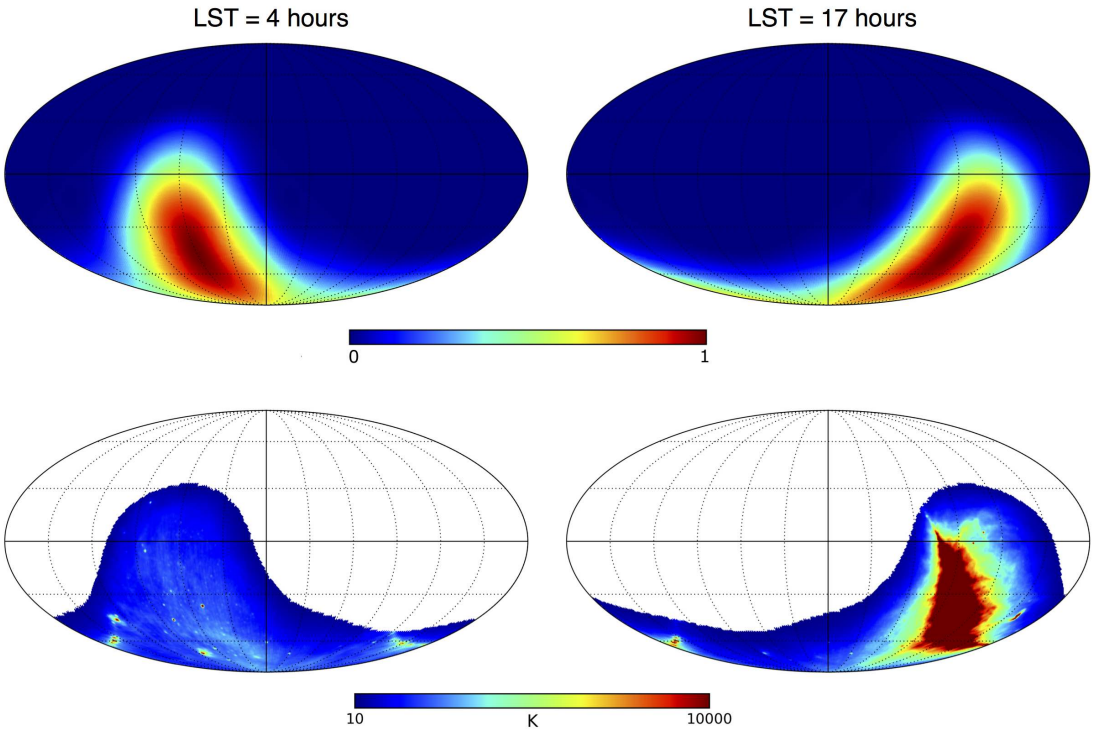

Figure 4.11: As the Earth rotates, the PRI^{Z}M 100 MHz East-West beam *(top panels)* map different patches of the sky *(bottom panels)*. Here we see the antenna observing a hotter patch when the Galactic centre is up *(right panels)*, and a comparatively colder patch when the Galactic centre is below the horizon *(left panels)*. Similarly, the North-South beam maps the orthogonal polarization.

As we understand, in the operating frequencies of global signal experiments, the astrophysical foregrounds are dominated by Galactic emission that is 10^3–10^4 times brighter than the expected cosmological signal. At these frequencies, the global sky model (GSM) by de Oliveira-Costa et al. (2008) generates the expected sky brightness temperature, $T_\nu(\theta, \phi)$, by interpolating data from many different publicly available radio surveys with a frequency range of 10 MHz–100 GHz (Figure 4.10). Using FEKO, we generated an expected antenna pattern, $A_\nu(\theta, \phi)$, with the coordinates (θ, ϕ) representing the azimuth and elevation in the plane of the antenna. A model of the expected sky spectrum (T_{sky}) was obtained by convolving the antenna pattern with the brightness temperature (obtained from GSM) across the entire sky for a given frequency ν

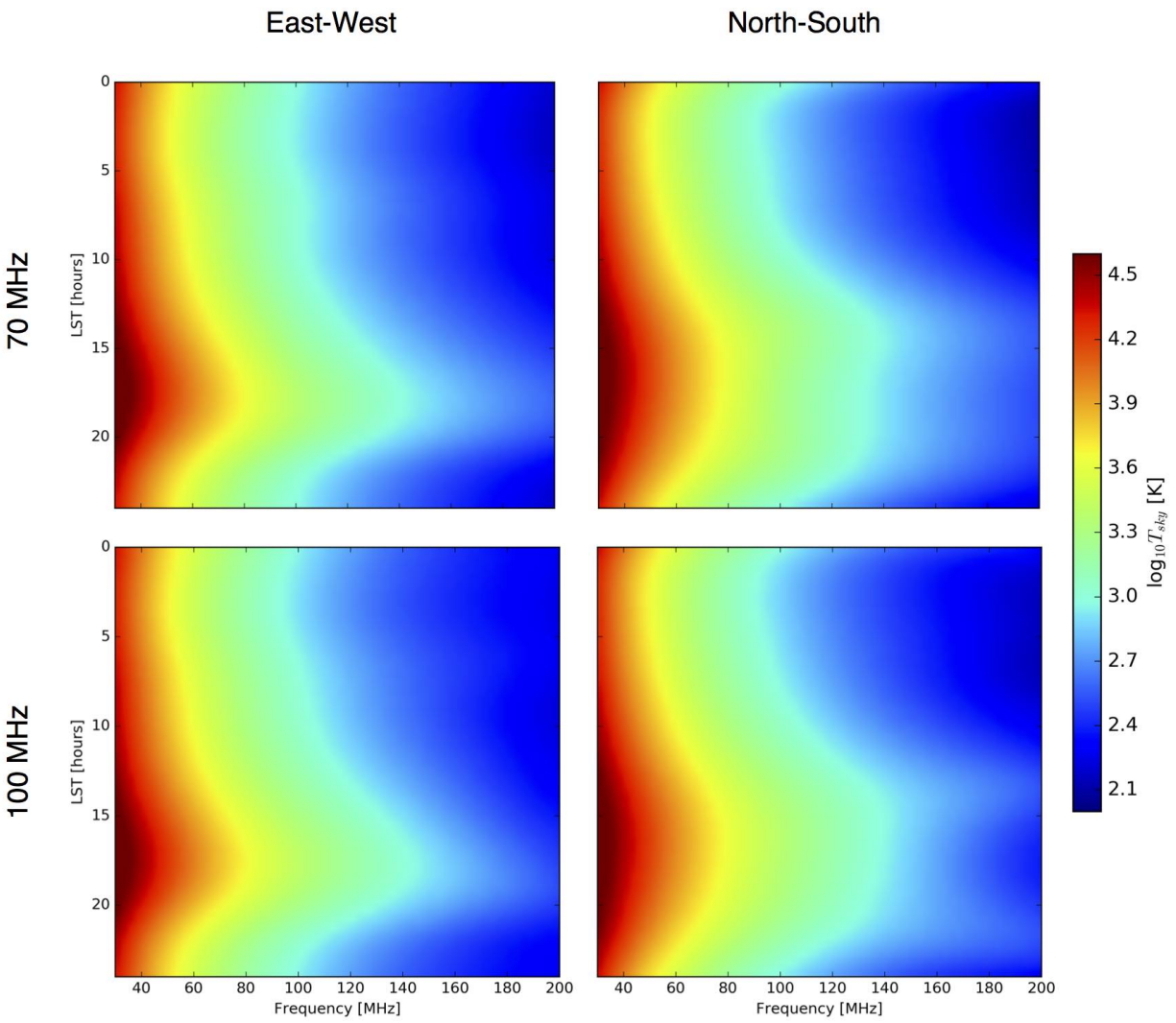

Figure 4.12: Expected sky spectrum T_{sky} generated by convolving the GSM with the FEKO beam of PRI^{Z}M.

and time, according to the formula:

$$T_{sky} = \frac{\int_{4\pi} A_\nu(\theta,\phi) T_\nu(\theta,\phi) d\Omega}{\int_{4\pi} A_\nu(\theta,\phi) d\Omega} \tag{4.13}$$

Figure 4.11 illustrates representative low- and high-brightness regions of the Galaxy that are observed as the sky drifts through the beam, and Figure 4.12 shows the resulting simulated spectra. The daily variance of a single frequency is plotted in Figure 4.13. A noticeable feature that is evident both in the observed data (Figure 4.4) and the simulation (Figure 4.12) is the

overall broadness of the North-South spectrum compared to the East-West spectrum. This feature can be related to the structural difference we observe in the E and H cuts of the PRI^{Z}M beam in Figure 2.6. A detailed comparison between the data and GSM predictions is still work in progress.

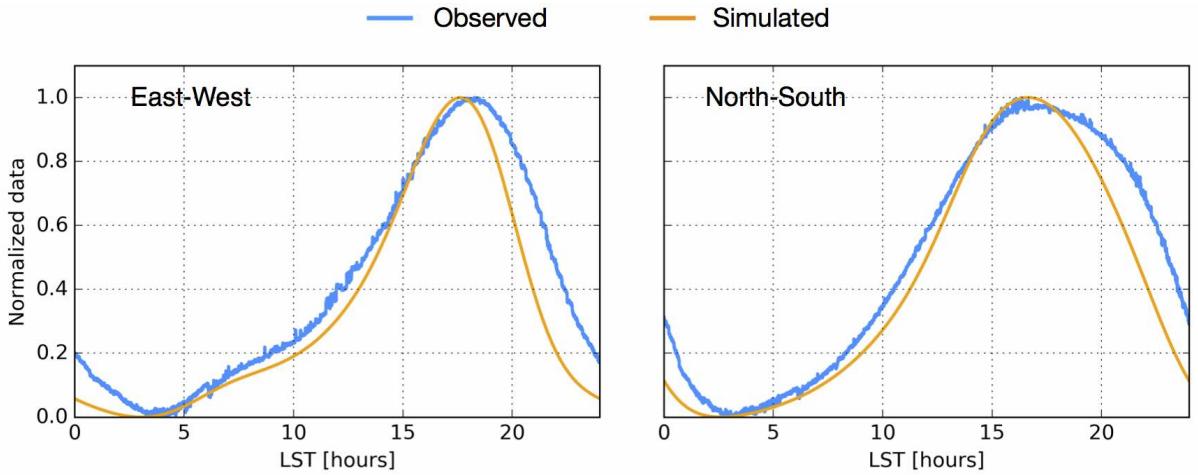

Figure 4.13: Daily variance of a frequency point at 100 MHz. The simulated data is in Kelvin, however, the observed data is not calibrated. Therefore, the values are feature scaled (using min-max normalization) for comparison.

4.4 Exploring lower frequencies

Installation of PRI^{Z}M on Marion Island opened doors to an excellent radio-quiet observing location on Earth. The overall radio quietness of Marion Island surpasses even the South African SKA site in the Karoo desert (see Figure 4.14). Given the excellent conditions for low-frequency experiments from Marion, we have laid the ground work to push the observation envelope to much lower frequencies. We introduced a brand new experiment called Array of Long Baseline Antennas for Taking Radio Observations from the Sub-Antarctic (ALBATROS) to Marion Island in April 2018, and installed a prototype called ALBATROS-Exploratory Gizmo on the Ground (ALBATROS-EGG, see Figure 4.15).

ALBATROS-EGGs are the first exploratory step toward building a larger array spanning

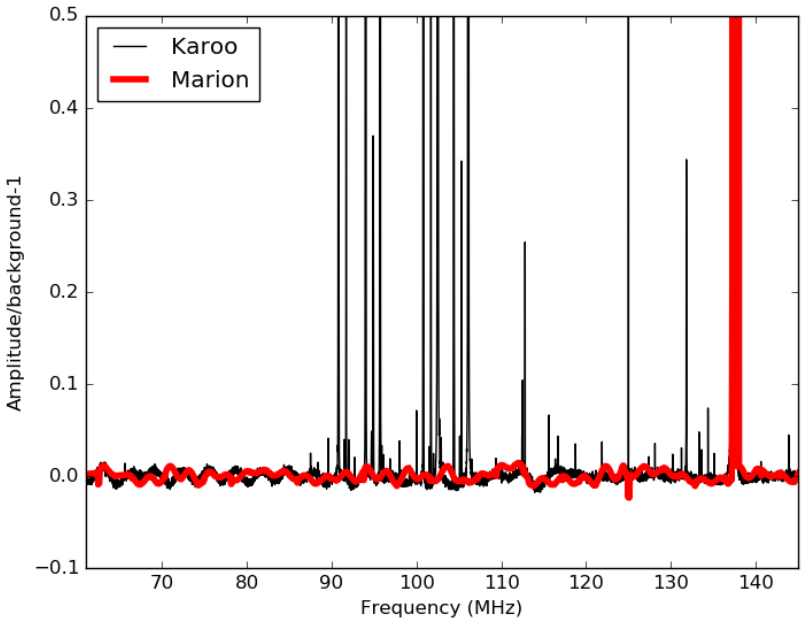

Figure 4.14: Comparison of radio spectrum on Marion *(thick red)* and in the Karoo desert *(thin black)* in the cosmic dawn frequency range band from the 100 MHz antennas. Both data have been identically filtered by applying a light high pass and notch filters to remove ripples. This plot shows the fractional amplitude above a background fit to the raw and uncalibrated data without RFI excision. Apart from Orbcomm satellite transmission at 137–138 MHz, there is no visible RFI in the Marion data. The feature at 125 MHz is an artifact of the FPGA clock and not due to RFI.

the island, with the aim of imaging the sky at low frequencies ($<$10 MHz) that have been unexplored since the 1970s. The measurements in the sub-10 MHz frequency regime has been very limited, mainly done in the '60s and '70s from Tasmania (Ellis et al., 1963; Reber, 1968), and with a resolution of 5–10 degrees. The ALBATROS experiment will place small (significantly sub-wavelength) antennas at each of the Marion field huts and record raw electric field samples (technically, channelize then record 1-bit baseband). The dynamic range issues at 1-bit in the large-signal limit can be worked around by implementing effective techniques. The baselines on Marion will provide a resolution $\sim$8 arcminutes full width half maximum (FWHM) at 5 MHz as

Figure 4.15: ALBATROS-EGG with a baseline of ∼120 m *(yellow dashed line)* installed at the PRI^{Z}M site in April 2018. The PRI^{Z}M antennas and shipping containers are visible to the right of the ALBATROS-EGG baseline.

shown in Figure 4.16.

4.4.1 ALBATROS-EGG instrument

An ALBATROS-EGG is a single element dual polarization radiometer that uses the antenna and the front-end electronics from the LWA experiment, and a receiver similar to that of PRI^{Z}M. The operating frequency range of the experiment is 0–125 MHz, with a resolution of ∼61 kHz. Both antennas have a 10 m × 10 m ground screen, and a ∼120 m baseline. The PRI^{Z}M site offers an excellent testbed for the ALBATROS experiment, and therefore the ALBATROS-EGG instrument is hosted at the PRI^{Z}M deployment site as shown in Figure 4.15.

The front-end and the backend are separated by 100 m to minimize self generated RFI. Signal is transmitted from the antenna to the receiver over 100 m long LMR400 coaxial cable. Currently, there are four signal chains, and each has a ∼20 dB amplification at the backend, and a high pass filter at 0.5 MHz. Figure 4.17 shows the ALBATROS-EGG receiver which uses a single SNAP board. Currently, we are using the on-board 8-bit ADCs on the SNAP board to digitize the

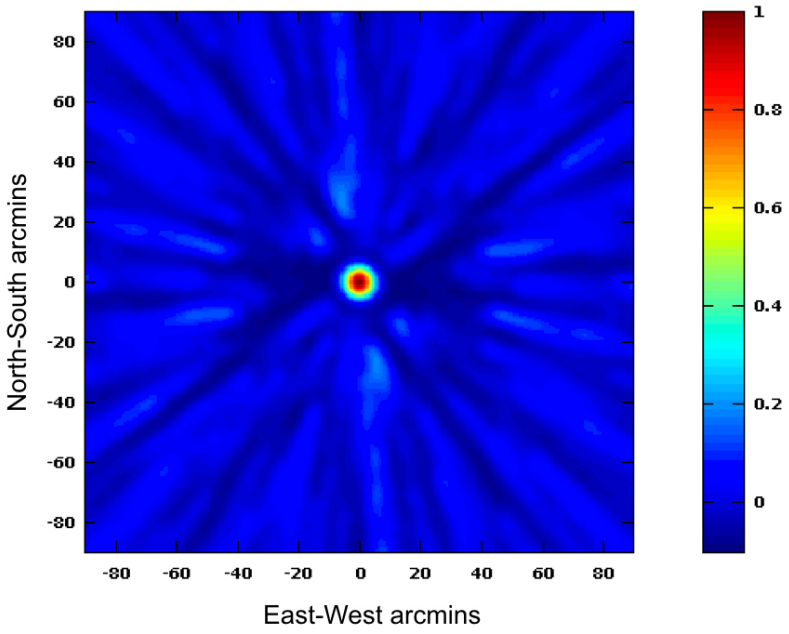

Figure 4.16: A synthesized beam of the ALBATROS experiment, with antennas at all the field huts on Marion, and a longest baseline of ∼20 km. The beam has a resolution of 8 arcminutes FWHM at 5 MHz.

signal, followed by auto- and cross- correlation performed by the FPGA. The backend Faraday cage is custom designed to fit inside a backpack, and the receiver can be transported by a single person during remote deployments. The experiment is powered by four 12 V 200 Ah lead crystal batteries, and the total power draw is ∼45 W. The charging schedule of the batteries is similar to PRI^{Z}M.

Current efforts are directed towards developing single-antenna stations that operate autonomously and that store baseband data for offline correlation. These autonomously operating stations will be deployed initially to the field huts near to the main base, and eventually to the rest of the huts. Major efforts for the upcoming deployment include: 1. adding a solar charging station, 2. developing the firmware for writing baseband, and 3. data storage.

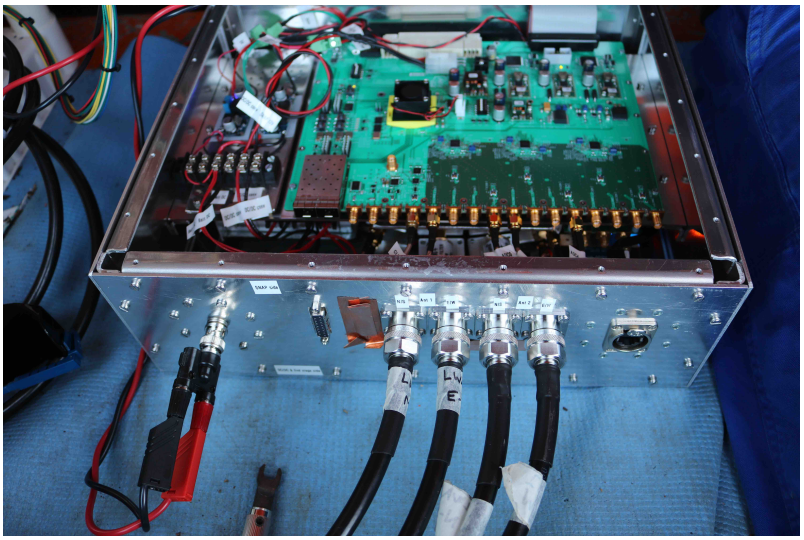

Figure 4.17: Current version of the ALBATROS-EGG receiver with inputs from two antennas, and encloses a single SNAP board. The future revisions will cater to only a single antenna and accommodate additional hardware such as a calibrator switch circuit. An important aspect of the receiver box design is the ease of transportation for remote deployments.

4.4.2 ALBATROS-EGG data : first look

We recorded a modest amount of data during the 2018 takeover, and the analysis is in progress. The first light from the antennas is shown in Figure 4.18, it shows the auto-spectra of East-West polarization of one antenna, and its cross-correlation with the second antenna in the same polarization. A major area of attention is the performance of the antennas at frequencies below 20 MHz. In Figure 4.18, we notice fringes down to $\sim$10 MHz, and we expect to observe at lower frequencies during the upcoming solar minimum in 2019-20. The reduction in shortwave reflections $<$30 MHz during night is evident in the ALBATROS-EGG data, like it was observed in PRI^{Z}M data.

Expanding the experiment by adding antennas at the field huts will provide us longer baselines using which we can make high-resolution measurements at lowest possible frequencies during the solar minimum.

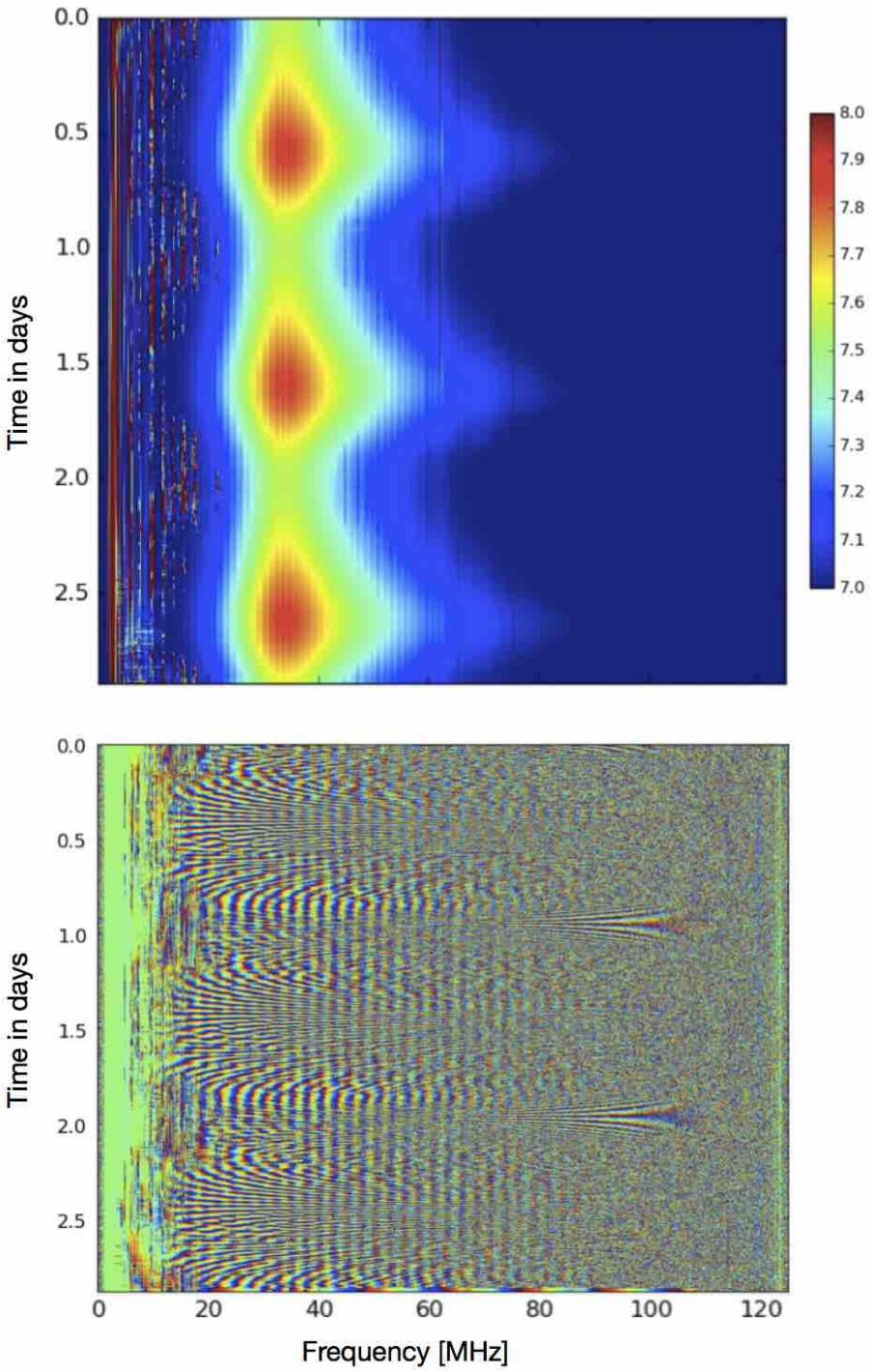

Figure 4.18: A representative plot of auto *(top)* and cross *(bottom)* correlation of $\sim$3 days of East-West polarization data from the recently installed ALBATROS-EGG experiment. The auto-spectra colourbar shows log values of the raw signal amplitude recorded by the SNAP board. The fringes < 20 MHz in the cross-spectra is a visual confirmation of the antenna performance at lower frequencies, and we expect to observe at lower frequencies during the solar minimum.

4.5 Conclusions and future outlook

The 21 cm HI line is a promising probe into the cosmic dawn and other epochs in the early Universe. Observation of the cosmic dawn holds the key to understand the nature of the first luminous sources that turned on in the Universe a few hundred million years after the Big Bang. The radiation from these sources interacted with the IGM and imprinted a characteristic absorption signature in the evolution of the globally averaged 21 cm signal when observed as a function of frequency. Theoretically, the 21 cm spectrum is expected to have a $\sim$200 mK absorption feature at a redshift of $\sim$20 (Cohen et al., 2017). A recent detection by Bowman et al. (2018) of an absorption feature at $\sim$78 MHz in the globally averaged sky spectrum, has excited much interest. The detection, however, is a factor of two greater than the largest predictions (Cohen et al., 2017), and has an unexpected wider absorption trough profile. Therefore, similar experiments, including PRI^{Z}M, have already focused their efforts in providing an independent verification of the detection.

PRI^{Z}M is a brand new experiment built in 2017, and consists of two radiometers covering the frequency range 20–300 MHz (Philip et al., 2018). PRI^{Z}M operates on eight lead crystal batteries (200 Ah each), and the combined power draw of both radiometers is $\sim$65 W. In this dissertation, I have provided a detailed discussion on the design and build of the instrument, and presented a walk through of individual components in the system. PRI^{Z}M is deployed to an excellent radio-quiet location called Marion Island in the sub-Antarctic. Marion island has no visible RFI contaminations, and offers above 2000 km isolation from the surrounding mainlands. In this dissertation, I have summarized all our voyages to Marion, with a detailed description of the island, and preliminary characterization of its RFI profile. Marion Island is one of the most promising observing sites on Earth for low-frequency experiments. In 2017, PRI^{Z}M became the first radio telescope to be deployed to Marion.

In April 2018, we laid the groundwork to push the observational envelope to lower frequencies by installing ALBATROS-EGG at the PRI^{Z}M site. ALBATROS-EGG is an exploratory prototype of ALBATROS, which will consist of autonomous radio receivers operating in the 0–125 MHz range, and will be deployed to all field huts on Marion. ALBATROS aims to image the

sky at low frequencies ($<$10 MHz), and provide an improvement over the existing measurements done in the '60s and '70s.

The data analysis of PRI^{Z}M is currently ongoing. Therefore, this dissertation presents a minimal data analysis effort, with preliminary results from a semi-calibrated $\sim$20 minute dataset placing PRI^{Z}M with a factor of $\sim$10 from the recent EDGES detection (Bowman et al., 2018). Since ours is a global signal experiment, the analysis is dominated entirely by systematic rather than statistical error. Instrumental systematics can be better understood with precise measurements of reflections in the signal chain, with prominent tests in the lab to characterize individual components in the system. In addition to this, the upcoming voyages will focus on precise on-site calibration measurements. Besides, we aim to increase the efficiency of the existing calibration pipeline in order to completely remove the instrumental effects from the data. With a precise calibration scheme, and a thorough understanding of the systematics, we aim to provide improved results in the future.

APPENDIX A

Programming Valon5009

As mentioned in Section 2.4.2, the Valon is programmed using the following lines of Python code are to program the Valon 5009 to generate a 500 MHz sampling signal with 15 dB attenuation at Source 1:

```
import VSerialPort
sp = VSerialPort.VSerialPort()
sp.writeline( "status" )
sp.readAll()
sp.writeline( "Source 1; Frequency 500 M" )
sp.readAll()
sp.writeline( "Source 1; ATT 15" )
sp.readAll()
sp.writeline( "SAV" )
sp.readAll()
```

VSerialPort.py is a python script available on the Valon website[1], and is used to establish serial communication between Valon 5009 and a computer using the FTDI serial to USB chip.

[1] http://valontechnology.com/5009users/5009.htm

Bibliography

Anderson, L., Aubourg, E., Bailey, S., et al. 2014, MNRAS, 439, 83

Barkana, R. 2018, nat, 555, 71

Barkana, R., & Loeb, A. 2001, Physics Report, 349, 125

—. 2004, ApJ, 609, 474

—. 2008, MNRAS, 384, 1069

Barkana, R., Outmezguine, N. J., Redigolo, D., & Volansky, T. 2018, ArXiv e-prints, arXiv:1803.03091

Becker, G. D., Bolton, J. S., & Lidz, A. 2015, ArXiv e-prints, arXiv:1510.03368

Bennett, C., Boggess, N., Cheng, E., et al. 1993, Advances in Space Research, 13, 409

Bennett, C. L., Halpern, M., Hinshaw, G., et al. 2003, apjs, 148, 1

Beringer, J., Arguin, J. F., Barnett, R. M., et al. 2012, Phys. Rev. D, 86, 010001

Bernardi, G., Zwart, J. T. L., Price, D., et al. 2016, mnras, 461, 2847

Beuermann, K., Kanbach, G., & Berkhuijsen, E. M. 1985, AAP, 153, 17

Bowman, J. D., Morales, M. F., & Hewitt, J. N. 2009, apj, 695, 183

Bowman, J. D., Rogers, A. E. E., Monsalve, R. A., Mozdzen, T. J., & Mahesh, N. 2018, Nature, 555, 67

Bromm, V. 2013, Reports on Progress in Physics, 76, 112901

Campbell, D. B. 2002, in Astronomical Society of the Pacific Conference Series, Vol. 278, Single-Dish Radio Astronomy: Techniques and Applications, ed. S. Stanimirovic, D. Altschuler, P. Goldsmith, & C. Salter, 81–90

Chen, X., & Miralda-Escudé, J. 2004, apj, 602, 1

Chuzhoy, L., & Shapiro, P. R. 2007, apj, 655, 843

Ciardi, B., Ferrara, A., & White, S. D. M. 2003, MNRAS, 344, L7

Cohen, A., Fialkov, A., Barkana, R., & Lotem, M. 2017, mnras, 472, 1915

de Oliveira-Costa, A., Tegmark, M., Gaensler, B. M., et al. 2008, mnras, 388, 247

DeBoer, D. R., Parsons, A. R., Aguirre, J. E., et al. 2017, pasp, 129, 045001

Dijkstra, M. 2014, PASA, 31, e040

Dine, M., & Kusenko, A. 2003, Reviews of Modern Physics, 76, 1

Ellingson, S. W., Taylor, G. B., Craig, J., et al. 2013, IEEE Transactions on Antennas and Propagation, 61, 2540

Ellis, G. R. A., Green, R. J., & Hamilton, P. A. 1963, Australian Journal of Physics, 16, 545

Ewen, H. I., & Purcell, E. M. 1951, Nature, 168, 356

Fan, X., Carilli, C. L., & Keating, B. 2006, Annual Review of A&A, 44, 415

Fialkov, A., Barkana, R., & Visbal, E. 2014, Nature, 506, 197

Fialkov, A., & Loeb, A. 2013, jcap, 11, 066

Field, G. B. 1959, apj, 129, 536

Fuller, G. M., Mathews, G. J., & Alcock, C. R. 1988, Physical Review D, 37, 1380

Furlanetto, S. R., & Furlanetto, M. R. 2007a, mnras, 374, 547

—. 2007b, mnras, 379, 130

Furlanetto, S. R., Oh, S. P., & Briggs, F. H. 2006, physrep, 433, 181

Furlanetto, S. R., & Pritchard, J. R. 2006, mnras, 372, 1093

Gleser, L., Nusser, A., & Benson, A. J. 2008, Monthly Notices of the Royal Astronomical Society, 391, 383

Goldenberg, H. M., Kleppner, D., & Ramsey, N. F. 1960, Phys. Rev. Lett., 5, 361

Gunn, J. E., & Peterson, B. A. 1965, apj, 142, 1633

Guth, A. H. 1981, Phys. Rev. D, 23, 347

Haslam, C. G. T., Salter, C. J., Stoffel, H., & Wilson, W. E. 1982, A&A Supplement, 47, 1,2,4

Hickish, J., Abdurashidova, Z., Ali, Z., et al. 2016, Journal of Astronomical Instrumentation, 5, 1641001

Hirata, C. M., & Sigurdson, K. 2007, mnras, 375, 1241

Jáuregui–García, J. M., Peterson, J. B., Castillo–Domínguez, E., & Voytek, T. C. 2017, IEEE, AP-S

Jelić, V., Zaroubi, S., Labropoulos, P., et al. 2008, mnras, 389, 1319

Jeon, M. 2015, in American Astronomical Society Meeting Abstracts, Vol. 225, American Astronomical Society Meeting Abstracts, 318.06

Kajantie, K., & Kurki-Suonio, H. 1986, Physical Review D, 34, 1719

Kellermann, K. I., & Owen, F. N. 1988, published in Galactic and Extragalactic Radio Astronomy, 1988, 2nd edition, eds. G. L. Verschuur and K. I. Kellerman, Springer-Verlag

Lawson, K. D., Mayer, C. J., Osborne, J. L., & Parkinson, M. L. 1987, MNRAS, 225, 307

Linde, A. 1982, Physics Letters B, 108, 389

Liu, A., Tegmark, M., Bowman, J., Hewitt, J., & Zaldarriaga, M. 2009, mnras, 398, 401

Loeb, A., & Zaldarriaga, M. 2004, Physical Review Letters, 92, 211301

Madau, P., Meiksin, A., & Rees, M. J. 1997, ApJ, 475, 429

Meiksin, A. 2006, mnras, 370, 2025

Mellema, G., Iliev, I. T., Pen, U.-L., & Shapiro, P. R. 2006, MNRAS, 372, 679

Mesinger, A., Ferrara, A., Greig, B., et al. 2015, Advancing Astrophysics with the Square Kilometre Array (AASKA14), 11

Monsalve, R. A., Rogers, A. E. E., Bowman, J. D., & Mozdzen, T. J. 2017, apj, 847, 64

Morales, M. F., & Wyithe, J. S. B. 2010, Annual Review of Astronomy and Astrophysics, 48, 127

Morandi, A., & Barkana, R. 2012, mnras, 424, 2551

Mortlock, D. J. 2015, ArXiv e-prints, arXiv:1511.01107

Mozdzen, T. J., Bowman, J. D., Monsalve, R. A., & Rogers, A. E. E. 2017, mnras, 464, 4995

Nhan, B. D., Bradley, R. F., & Burns, J. O. 2017, ApJ, 836, 90

Parsons, A. R., Backer, D. C., Foster, G. S., et al. 2010, A.J., 139, 1468

Peebles, P. J. E. 1968, apj, 153, 1

Pentericci, L., Vanzella, E., Fontana, A., et al. 2014, ApJ, 793, 113

Penzias, A. A., & Wilson, R. W. 1965, apj, 142, 419

Philip, L., Abdurashidova, Z., Chiang, H. C., et al. 2018, Journal of Astronomical instrumentation, doi:10.1142/S2251171719500041

Planck Collaboration. 2015, ArXiv e-prints, arXiv:1506.07135

Planck Collaboration, Ade, P. A. R., Aghanim, N., et al. 2016a, AAP, 594, A13

Planck Collaboration, Adam, R., Aghanim, N., et al. 2016b, AAP, 596, A108

Planelles, S., Schleicher, D. R. G., & Bykov, A. M. 2015, SSR, 188, 93

Platania, P., Bensadoun, M., Bersanelli, M., et al. 1998, ApJ, 505, 473

Price, D. C., Greenhill, L. J., Fialkov, A., et al. 2017, ArXiv e-prints, arXiv:1709.09313

Pritchard, J., & Loeb, A. 2010, Nature, 468, 772–773

Pritchard, J. R., & Furlanetto, S. R. 2007, MNRAS, 376, 1680

Pritchard, J. R., & Loeb, A. 2012, Reports on Progress in Physics, 75, 086901

Reber, G. 1968, Journal of the Franklin Institute, 285, 1

Rottgering, H. J. A., Braun, R., Barthel, P. D., et al. 2006, ArXiv Astrophysics e-prints, astro-ph/0610596

Rybicki, G. B., & Lightman, A. P. 1986, Radiative Processes in Astrophysics, 400

Sadler, E. M., Jackson, C. A., & Cannon, R. D. 2003, in Astronomical Society of the Pacific Conference Series, Vol. 289, The Proceedings of the IAU 8th Asian-Pacific Regional Meeting, Volume 1, ed. S. Ikeuchi, J. Hearnshaw, & T. Hanawa, 105–112

Seo, H.-J., & Eisenstein, D. J. 2005, ApJ, 633, 575

Shaver, P. A., Windhorst, R. A., Madau, P., & de Bruyn, A. G. 1999, A&A, 345, 380

Singh, S., Subrahmanyan, R., Shankar, N. U., et al. 2018a, Experimental Astronomy, 45, 269

Singh, S., Subrahmanyan, R., Udaya Shankar, N., et al. 2018b, apj, 858, 54

Sironi, G. 1976, Astrophysics and Space Science, 44, 159

Sokolowski, M., Tremblay, S. E., Wayth, R. B., et al. 2015, pasa, 32, e004

Stark, D. P., Ellis, R. S., & Ouchi, M. 2011, ApJ, 728, L2

Steigman, G. 2007, Annual Review of Nuclear and Particle Science, 57, 463

Taylor, G. B., Ellingson, S. W., Kassim, N. E., et al. 2012, Journal of Astronomical Instrumentation, 1, 1250004

Tegmark, M., Eisenstein, D. J., Strauss, M. A., et al. 2006, Physical Review D, 74, 123507

Tingay, S. J., Goeke, R., Bowman, J. D., et al. 2013, pasa, 30, e007

Valdes, M., Evoli, C., & Ferrara, A. 2010, MNRAS, 404, 1569

van de Hulst, H. C. 1945, Ned. Tijdschr. Natuurk, 11, 210

Voytek, T. C., Natarajan, A., Jáuregui García, J. M., Peterson, J. B., & López-Cruz, O. 2014, apjl, 782, L9

Wang, X., Tegmark, M., Santos, M. G., & Knox, L. 2006, ApJ, 650, 529

Wislez, J.-M. 1996, in Proceedings of the International Meteor Conference, 14th IMC, Brandenburg, Germany, 1995, ed. P. Roggemans & A. Knofel, 99–117

Wouthuysen, S. A. 1952, Astronomical Journal, 57, 31

Xu, X., White, M., Padmanabhan, N., et al. 2010, ApJ, 718, 1224

Yoshida, N., Hosokawa, T., & Omukai, K. 2012, Progress of Theoretical and Experimental Physics, 2012, 01A305

Zaroubi, S. 2012, in Astrophysics and Space Science Library, Vol. 396, The First Galaxies, ed. T. Wiklind, B. Mobasher, & V. Bromm, 45

Zaroubi, S. 2013, in Astrophysics and Space Science Library, Vol. 396, The First Galaxies, ed. T. Wiklind, B. Mobasher, & V. Bromm, 45

Zaroubi, S., Thomas, R. M., Sugiyama, N., & Silk, J. 2007, MNRAS, 375, 1269

Zuo, S., Chen, X., Ansari, R., & Lu, Y. 2018, ArXiv e-prints, arXiv:1801.04082

Zygelman, B. 2005, The Astrophysical Journal, 622, 1356